Université de Montréal

Direct detection of dark matter with the PICO Experiment and the PICO-0.1 calibration chamber

par

Frédéric Tardif

Département de physique

Faculté des arts et des sciences

Mémoire présenté à la Faculté des études supérieures

en vue de l'obtention du grade de

Maître ès sciences (M.Sc.)

en physique

31 août 2018

© Frédéric Tardif, 2018

SOMMAIRE

La détection de la matière sombre demeure aujourd'hui l'un des principaux problèmes non résolus de la physique. Comptant pour près de 85% de toute la densité de matière de l'Univers, elle a été déduite par de nombreuses observations astronomiques, mais aucune particule de matière sombre n'a été détectée à ce jour. L'expérience PICO a cet objectif comme raison d'être, en utilisant la chambre à bulles pour faire ainsi. PICO peut détecter des interactions de très basses énergies dans ses détecteurs à liquides surchauffés, situés dans le laboratoire souterrain SNOLAB à Sudbury, en Ontario. PICO a, et a eu, plusieurs détecteurs de recherche de la matière sombre, de même que de plus petits détecteurs utilisés pour effectuer différents tests ou calibrations. PICO-0.1 est une chambre de calibration située à l'Université de Montréal et a été utilisée pour les études présentées dans ce mémoire.

Dans ce mémoire, les données et l'analyse de mesures faites avec PICO-0.1 sont présentées. Une étude du seuil de Seitz - seuil d'énergie théorique pour qu'un événement se produise dans une chambre à bulles - est faite, avec la réaction monoénergétique $^{35}\mathrm{Cl}(n_{th},p)^{35}\mathrm{S}$ dans du C_2ClF_5; l'étude du recul monoénergétique ^{35}S, directement à l'intérieur du détecteur, est présentée. De plus, la détection des reculs de protons dans PICO-0.1 est détaillée; d'abord par l'analyse du signal acoustique du proton produit par $^{35}\mathrm{Cl}(n_{th},p)^{35}\mathrm{S}$, et ensuite par diffusion élastique des neutrons et des rayons gammas à haute énergie sur l'hydrogène dans du $C_2H_2F_4$.

Mots-clés: Matière sombre, WIMPs, détection directe, chambre à bulles, PICO, seuil de Seitz, recul de protons.

SUMMARY

Dark matter detection remains one of the main unresolved problems in physics. Accounting for almost 85% of all the matter density in the Universe, it was inferred through many astronomical observations, but no dark matter particle has been detected yet. The PICO experiment has this objective as its purpose, using the bubble chamber in order to do so. PICO can detect extremely low-energy interactions in its superheated liquid detectors, located in the SNOLAB underground laboratory in Sudbury, Ontario. PICO has and has had multiple dark matter search detectors, as well as small detectors used to perform calibrations and tests. PICO-0.1 is a calibration chamber located at the University of Montreal and was used for the studies presented in this thesis.

In this thesis, data and analysis of measurements made with PICO-0.1 are presented. A study of the Seitz threshold - theoretical energy threshold for an event to occur in a bubble chamber - is made, with the monoenergetic reaction $^{35}\mathrm{Cl}(n_{th},p)^{35}\mathrm{S}$ in C_2ClF_5; the study of the monoenergetic ^{35}S recoil, directly inside the detector, is presented. Furthermore, the detection of proton recoils in PICO-0.1 is detailed; first through the analysis of the acoustic signal of the proton produced by $^{35}\mathrm{Cl}(n_{th},p)^{35}\mathrm{S}$, and second through elastic scattering of neutrons and high energy gamma rays on hydrogen in $C_2H_2F_4$.

Keywords: Dark matter, WIMPs, direct detection, bubble chamber, PICO, Seitz threshold, proton recoils.

À Alexia,

CONTENTS

Sommaire iii

Summary v

Dedication vii

List of tables xiii

List of figures xv

Acknowledgements xxiii

Contribution of the author xxv

Introduction 1

Chapter 1. Dark matter in the Universe 3

1.1. Dark matter 3

1.1.1. The Lambda Cold Dark Matter model 4

1.2. Evidences for dark matter 7

1.2.1. Galaxy rotation curves 8

1.2.2. Gravitational lensing 9

1.2.2.1. Bullet Cluster 12

1.2.3. Cosmic microwave background 13

Chapter 2. Dark matter candidates 17

2.1. Axions 17

2.2. Sterile neutrinos 18

2.3. WIMPs 20

Chapter 3. Dark matter detection principles 23

3.1. Direct detection 24

3.1.1. Direct detection experiments ... 27
3.2. Indirect detection ... 33
3.2.1. Indirect detection experiments ... 35
3.3. Production ... 38
Chapter 4. The PICO Experiment ... 41
4.1. Bubble chambers ... 41
4.1.1. Superheated liquids ... 41
4.1.2. Detection principle ... 42
4.2. PICO detectors ... 44
4.2.1. Characteristics ... 44
4.2.2. Detectors ... 47
4.2.2.1. PICO-2L ... 47
4.2.2.2. PICO-60 ... 48
4.2.2.3. PICO-40L ... 49
4.2.2.4. PICO-500 ... 50
4.2.2.5. PICO-0.1 ... 51
4.3. Seitz Model ... 52
4.3.1. The heat spike model ... 53
4.3.2. dE/dx threshold ... 57
4.4. Detector response ... 58
4.5. Current results ... 59
Chapter 5. Seitz threshold characterization with C_2ClF_5 ... 61
5.1. C_2ClF_5 thermodynamics ... 61
5.2. ^{35}S 17 keV monoenergetic recoil data ... 62
5.2.1. Thermal neutrons ... 63
5.2.2. Sulfur and proton recoils ... 63
5.2.3. Data ... 65
5.3. *SRIM* simulations ... 66
5.3.1. Bubble efficiency ... 66
5.3.2. Harper parameter ... 67

5.3.3. Surface tension 69
5.3.4. Heat dissipation 70
5.3.5. Critical radius distribution 72
5.4. Gaussian blurred step Seitz threshold 74
Chapter 6. Detecting proton recoils with PICO-0.1 81
6.1. 600 keV proton recoils in C_2ClF_5 82
6.1.1. Proton and sulfur recoils 82
6.1.2. Acoustics analysis 85
6.1.2.1. z-position dependence 85
6.1.2.2. Acoustic power distibution 86
6.1.2.3. Selection of frequency windows 86
6.1.3. Harper Parameter 88
6.2. Proton recoils in $C_2H_2F_4$ 92
6.2.1. $C_2H_2F_4$ thermodynamics 93
6.2.2. 22.8 keV neutrons 93
6.2.2.1. Nuclear recoils 93
6.2.2.2. Data with water in water bath 95
6.2.2.3. Data without water in water bath 96
6.2.2.4. Simulations 97
6.2.3. Thomson scattering 99
6.2.3.1. Data 100
6.2.3.2. Simulations 101
6.3. Projected limits plot 104
Conclusion 107
Bibliography 109
Appendix A. PICO-60 C_3F_8 Paper ..... A-i
Appendix B. PICO-60 C_3F_8 complete exposure paper ..... B-i

LIST OF TABLES

1.1 Types of universes, their geometries and parameters. 6

1.2 Observed values of cosmological parameters [2] and calculated value of the cosmological constant Λ. 7

3.1 Target nuclei properties [20]. 27

5.1 Thermodynamic properties of C_3F_8 and C_2ClF_5 [61]. 62

5.2 Summary of GBS thresholds parameters obtained from monoenergetic recoils data. We assume that the energy deposited from the 5.49 MeV alphas to form bubbles was about (and perhaps a bit above) $E_0 = 71$ keV. 80

6.1 Thermodynamic properties of C_3F_8, C_2ClF_5 and $C_2H_2F_4$ [61]. 93

LIST OF FIGURES

1.1 2D representations of 3D space sections, for closed (left), flat (center) and open (right) geometries [1]. 5

1.2 Andromeda galaxy rotation (velocity) curve, expected (red) vs. measured (white) [7]. Stars far from the center of the galaxy have much higher velocities than expected from Newtonian mechanics, indicating that there is more mass than observed from the luminous disk. 9

1.3 Illustration of gravitational lensing [1]. A light source S emits light rays towards an observer O, bent by an intermediate mass. For the observer O, S appears at different points I_1, I_2 and I_3. 10

1.4 Three different kinds of light rays orbits, depending on $1/b^2$ compared to the maximum of W_{eff}, i.e. $W_{\mathit{eff}}(3GM/c^2) = c^4/27G^2M^2$ [1]. At the top, $1/b^2 = W_{\mathit{eff}}(3GM/c^2)$; in the middle, $1/b^2 < W_{\mathit{eff}}(3GM/c^2)$; at the bottom, $1/b^2 > W_{\mathit{eff}}(3GM/c^2)$. $1/b^2$ is shown with dashed lines (or a dot) on the left, compared to W_{eff} as a function of c^2r/GM (r/M in $c = 1$ units). The shape of the corresponding light ray orbit is shown on the right. 11

1.5 Colorized data the bullet cluster collision [9]. In red is the X-ray light coming from hot interstellar gases; in blue is the reconstructed mass from gravitational lensing. Most of the mass comes from the two regions ahead of the interstellar gases, coincident with the visible galaxies. 13

1.6 Cosmic Microwave Background anisotropy map, as measured by the Planck space observatory in 2013 [11]. 14

1.7 Planck 2015 temperature power spectrum, D_ℓ^{TT} ($= \Delta T^2$) in function of the angular momentum ℓ [2]. Thick line is the theoretical fit from the ΛCDM model. 15

2.1 Exclusion limits on neutralinos and chargino masses, obtained by LHC experiments at CERN [19]. On the left, limits for pair production of charginos, pair production of heavier neutralinos, or pair production of chargino

and neutralino, assuming light sleptons (lepton supersymmetric partner) mediating the decays. On the right, limits for pair production of chargino and neutralino, assuming decoupled sleptons, and chargino/neutralino decay through W^*, Z^* or H. 21

3.1 Feynman diagram of dark matter (χ) interactions with ordinary matter (f). 24

3.2 WIMP wind in comparison with the earth orbital plane. The angle between the two gives a potential variation of the WIMP signal between summer and winter. 26

3.3 Diagram of the dark matter direct detection experiments and their corresponding techniques. 28

3.4 One SuperCDMS detector, 76mm of diameter (left) and the experimental setup to take place in SNOLAB (right) [24]. 29

3.5 Superconductor transition above T_C through heat absorption in SuperCDMS detectors. [26]. 30

3.6 One 60-cm NEWS-G copper vessel (left) and the electric field inside a chamber (right). Field lines are shown on the right part of the picture, and intensities on the left part (corresponding to the log scale on the right) [27]. 31

3.7 Multi-wire proportional chamber. 31

3.8 The XENON100 detector, filled with 105 kg of LXe [28]. 32

3.9 The DEAP-3600 detector, filled with 3600 kg of LAr [33]. 33

3.10 Spectra from dark matter particles annihilation, for final state photons (top left), sum of all neutrino flavors (top right), electrons (bottom left) and protons (bottom right), for $m_\chi = 500$ GeV [35]. 35

3.11 Picture of the VERITAS telescope array [38]. 36

3.12 Ice Cube neutrino detector [39]. 37

3.13 CERN's LHC and experiments. 38

3.14 The ATLAS detector at LHC [45]. 40

4.1 Typical phase diagram, with the liquid-vapour saturation curve highlighted (left) and the Gibbs potential on the saturation curve (right). 42

4.2 Superheat phase diagram (left) and Gibbs potential of a superheated state (right). 43

4.3 Schematic representation of a bubble chamber [52]. 44
4.4 Ionization tracks in CERN's first liquid hydrogen bubble chamber in 1960 [53]. 45
4.5 Photo of a multi-bubble event from neutron scattering in the PICO-2L bubble chamber [21]. 45
4.6 PICO-2L inner vessel and bellows [21]. 48
4.7 A schematic view of the PICO-2L detector [54]. 49
4.8 A schematic view of the PICO-60 detector. 50
4.9 Design of the PICO-40L detector [58]. 51
4.10 PICO-500 in its pressure vessel, inside a water tank. 52
4.11 PICO-0.1. On the left, the chamber alone with its "top hat" containing the bellows. On the right, the chamber and its hydraulic cart. 53
4.12 PICO-0.1 complete setup. 54
4.13 Seitz critical energy curves for different temperatures, for C_2ClF_5 (left) and $C_2H_2F_4$ (right). 57
4.14 Recoil energy spectra for carbon and fluorine, for elastic scattering with neutrons of energy E_n (top). Detector response (count rate $R = dN/dt$) in function of its threshold energy E_{th}, for the same type of event (bottom). . . . 59
4.15 Spin-dependent WIMP-proton cross-section limits set by different dark matter detection experiments. Thick lines are direct detection experiments, while dashed lines are indirect detection experiments. 60
4.16 Spin-independent WIMP-nucleon cross-section limits set by different dark matter detection experiments. 60
5.1 C_2ClF_5 vapor pressure as a function of temperature [61]. 62
5.2 Thermalizing 22.8 keV neutrons with 2.25 cm of paraffin : on the left, the original 22.8 keV spectrum; on the right, the spectrum after passing through the paraffin. 64
5.3 Expected PICO-0.1 response to 17 keV monoergetic sulfur nucleus recoils from ^{35}Cl (n_{th},p) ^{35}S. At the top, the (monoenergetic) recoil energy spectrum. At the bottom, the expected count rate response by varying the threshold below E_{th}. 65

5.4 PICO-0.1 response to thermal neutrons with the reaction ^{35}Cl (n_{th},p) ^{35}S, producing 17 keV monoenergetic ^{35}S recoils. 65

5.5 Example of searching for a bubble event in *SRIM*. On the left, sufficient energy was deposited inside the critical length, and nucleation occurs. On the right, The end of the track is reached without ever having enough energy deposited inside the critical length to create a bubble; no nucleation occured. 67

5.6 Relation between the critical radius R_C and the critical energy E_C calculated from the Seitz model for C_2ClF_5, here at a constant temperature of 15°C. . . . 68

5.7 Efficiency curves produced with *SRIM* for 17 keV ^{35}S nucleus recoils in C_2ClF_5, for different b parameters. From top-left to bottom-right : $b = 0.1$, $b = 0.5$, $b = 1$ and $b = 2$. Each efficiency point is calculated with 1000 *SRIM* recoil simulations. 69

5.8 "Fine-tuning" the Harper parameter to reproduce the 17 keV data. We use $b = \frac{100}{(E_C/keV)^{2.2}}$. Efficiency is in arbitrary units. Each efficiency point is calculated with 100 *SRIM* recoil simulations. 70

5.9 Seitz threshold recalculated with smaller and larger surface tensions (0.8 to 1.2 times the original), for C_2ClF_5 at 15°C. 71

5.10 Efficiency curve produced with *SRIM* for 17 keV ^{35}S nucleus recoils in C_2ClF_5, with a 7% larger surface tension from the Seitz model. $b = 2$ is used. Efficiency is in arbitrary units. Each efficiency point is calculated with 100 *SRIM* recoil simulations. 71

5.11 Efficiency curve produced with *SRIM* for 17 keV ^{35}S nucleus recoils in C_2ClF_5, with a 20% energy loss from the original recoil and the energy deposition. $b = 2$ is used. Each efficiency point is calculated with 100 *SRIM* recoil simulations. 72

5.12 Efficiency curve produced with *SRIM* for 17 keV ^{35}S nucleus recoils in C_2ClF_5, with a gaussian-distributed R_C, of mean $\sigma = 0.5R_C$. $b = 1$ is used. Each efficiency point is calculated with 500 *SRIM* recoil simulations. 74

5.13 Efficiency curve produced with *SRIM* for 17 keV ^{35}S nucleus recoils in C_2ClF_5, with a gaussian-distributed R_C, of mean $\sigma = 0.25R_C$ (left) and $\sigma = 0.5R_C$ (right). $b = 2$ is used. Each efficiency point is calculated with 500 *SRIM* recoil simulations. 74

5.14 Efficiency curve produced with *SRIM* with a gaussian-distributed R_C, of mean $\sigma = 0.5R_C$, and with a 20% energy loss from the original recoil and the energy deposition. $b = 1$ is used. Each efficiency point is calculated with 500 *SRIM* recoil simulations. 75

5.15 The Gaussian blurred step function in grey (with mean μ and width σ), compared to the Heaviside function in red. 76

5.16 Gaussian blurred step event probability P in function of the recoil energy E_R, for $E_{GBS} = 10$ keV (blue) and $E_{GBS} = 15$ keV (green), and for a given original Seitz threshold of $E_{th} = 10$ keV. Both probability curves have $\sigma = 2$ keV, the width of the GBS. 77

5.17 Gaussian blurred step detector efficiency ϵ as a function of the threshold energy E_{th}, for $E_0 = 17$ keV (blue) and $E_0 = 11$ keV (green), and for a given monoenergetic recoil energy of $E_R = 17$ keV. Both efficiency curves have $\sigma = 2$ keV, the width of the GBS. 77

5.18 Fit of the 17 keV data with a GBS threshold of $E_0 = 11$ keV and width $\sigma = 2$ keV. We notice a $\Delta E = 6$ keV. 78

5.19 Fit of the 151 keV monoenergetic ^{210}Pb recoil data, with a GBS threshold of $E_0 = 141$ keV and width $\sigma = 16.8$ keV. We notice a $\Delta E = 10$ keV. 79

5.20 Fit of the 5.49 MeV monoenergetic alpha recoil data with a GBS threshold of $E_0 = 71$ keV and width $\sigma = 6.4$ keV. ΔE is irrelevant here for reasons stated in the text. 80

6.1 Representation of an alpha particle recoil event, along with an heavy element nucleus recoil. 82

6.2 Efficiency curves produced with *SRIM* for 600 keV proton recoils in C_2ClF_5, for $b = 1$ (left) and $b = 2$ (right). Each efficiency point is calculated with 100 *SRIM* recoil simulations. 83

6.3 Representation of a complete event from the reaction ^{35}Cl (n_{th}, p) ^{35}S, with both ^{35}S and proton recoils creating bubbles. 84

6.4 Range distribution for 10^4 600-keV protons in C_2ClF_5. 84

6.5 Acoustic power of ^{35}Cl (n_{th}, p) ^{35}S events in function of their height (z) in the detector, at 35 PSI, 15°C (left) and 25°C (right). 86

6.6 Normalized acoustic power distributions for ^{35}Cl (n_{th}, p) ^{35}S events (blue) and fast neutrons recoil events (red), all at 35 PSI, respectively (from top-left to bottom-right) for 1.66 keV (23°C), 2.15 keV (21°C), 2.72 keV (19°C), 3.53 keV (17°C), 4.44 keV (15.5°C) and 5.4 keV (14°C). The distributions for each threshold point are shown for both piezos. 87

6.7 Mean Fast Fourier Transform of ^{35}Cl (n_{th}, p) ^{35}S events (blue) and fast neutron recoil events (red), all at 35 PSI, respectively (from top-left to bottom-right) for 1.66 keV (23°C), 2.15 keV (21°C), 2.72 keV (19°C), 3.53 keV (17°C), 4.44 keV (15.5°C) and 5.4 keV (14°C). The FFTs for each threshold point are shown for both piezos. 89

6.8 Frequency selections for the mean Fast Fourier Transform of ^{35}Cl (n_{th}, p) ^{35}S events (blue) and fast neutron recoil events (red) of figure 6.7. Dark sections are now not taken into account. 90

6.9 Normalized acoustic power distributions with specific frequency selection (as described in equations 6.1.2, and shown on figure 6.8) for ^{35}Cl (n_{th}, p) ^{35}S events (blue) and fast neutron recoil events (red), all at 35 PSI, respectively (from top-left to bottom-right) for 1.66 keV (23°C), 2.15 keV (21°C), 2.72 keV (19°C), 3.53 keV (17°C), 4.44 keV (15.5°C) and 5.4 keV (14°C). The distributions for each threshold point are shown for both piezos. 91

6.10 Expected proton bubble efficiency, deduced from acoustics analysis. 92

6.11 Efficiency curves produced with *SRIM* for 600 keV proton recoils in C_2ClF_5, for $b = 3/2$ (left) and $b = 5/3$ (right). Each efficiency point is calculated with 100 *SRIM* recoil simulations. 92

6.12 $C_2H_2F_4$ vapor pressure as a function of temperature [**61**]. 94

6.13 PICO-0.1 response to 22.8 keV neutrons in $C_2H_2F_4$. All data (background and with source) are shown. Data are normalized to source activity. 95

6.14 Background-subtracted PICO-0.1 response to 22.8 keV neutrons in $C_2H_2F_4$, with visual markers for the different threshold energies of fluorine, carbon and hydrogen nuclei. Region of interest is $E_{th} \in$ [6.38,22.8] for proton recoil events. Data are normalized to source activity. 96

6.15 Background-subtracted PICO-0.1 response to 22.8 keV neutrons in $C_2H_2F_4$, with (blue) and without (red) water in the water bath. Data are normalized to source activity. 97

6.16 Background-subtracted PICO-0.1 response to 22.8 keV neutrons in $C_2H_2F_4$, with (blue) and without (red) water in the water bath. Data with water are manually shifted by 6.75 kev to match data without water. Data are normalized to source activity. 98
6.17 PICO-0.1 response to ^{124}SbBe neutrons in $C_2H_2F_4$, compared to simulations. 98
6.18 Expected detector response from Thomson scattering, for 1.368 MeV γ (left) and 2.754 MeV γ (right). 100
6.19 PICO-0.1 response to ^{24}Na gamma rays in $C_2H_2F_4$. Data are not normalized to source activity; threshold points were selected randomly for each event, compensating for the relative effect of the source decaying. Data for four ^{24}Na half-lives are used. 101
6.20 Simulation of PICO-0.1 response to ^{24}Na gamma rays in $C_2H_2F_4$. Complete response (left) and zoom on the region of interest where data were taken (right). 102
6.21 PICO-0.1 response to ^{24}Na gamma rays in $C_2H_2F_4$, data compared to simulations. 103
6.22 Simulation of PICO-0.1 response to ^{24}Na gamma rays in $C_2H_2F_4$, including the fraction from Thomson scattering 103
6.23 Potential new exclusion limits of the PICO experiment for the search dark matter (blue), using $C_2H_2F_4$ in PICO-40L, with an exposure of 120 live-days (5400 kg-days) at a threshold about 1 keV. Current exclusion limits of PICO are shown in black. The two blue curves are calculated assuming two different hydrogen nucleation efficiencies at 1 keV, as shown on figure 6.24 105
6.24 Hydrogen nucleation efficiencies at a 1 keV threshold, as a function of the recoil energy. The blue efficiency generates the lowest limit of the two on figure 6.23, the red efficiency generates the highest limit of the two. 106

ACKNOWLEDGEMENTS

First of all, I would like to thank my supervisor Viktor Zacek, for believing in me since the beginning, and for giving me the chance to work on the PICO project. Thank you for being available at all times to help me during the whole length of my degree. Your enthusiasm was contagious, and your innovative ideas were the backbone of my research; I owe a lot to you. I would also like to thank prof. Alan E. Robinson, for the tremendous support on the scientific side, and for improving my scientific knowledge each and every day.

Thanks to all the PICO collaboration, for promoting and sharing great knowledge, and for perpetuating harmonious and efficient team work.

Merci à mes collègues, qui auront égayé mes journées dans le bunker, loin de la lumière du jour, et auront rendu les voyages de conférence bien plus amusants, que ce soit à Chicago, Sudbury, Mont-Tremblant, Halifax ou Providence. Arthur, Frédéric, Mathieu, François, Simon, merci.

Un immense merci à mes parents, qui m'ont toujours inconditionnellement supporté dans tous mes projets. Sans vous, je ne me serai pas rendu où je suis rendu aujourd'hui.

Merci à Gabrielle pour les corrections à ce mémoire, de même que pour toute la connaissance dont tu fais part quotidiennement. Tu as fait de moi quelqu'un de bien moins ignorant.

Finalement, le plus grand des mercis à mes plus fidèles compagnes et compagnons, sans qui ces deux années auraient été bien plus difficiles à traverser, et qui auront toujours su être là pour moi ces 730 derniers jours. Marie-Maude, Félix, Vincent, Maxime, François, Amélie, merci infiniment. Vous êtes les meilleur.e.s.

CONTRIBUTION OF THE AUTHOR

My personal contribution to the PICO experiment consists mainly of the operation of the PICO-0.1 calibration chamber, and the analysis of the measurements made during the two years of my master's degree. For those two years I was in charge of the data taking and analysis for this detector, filled with C_2ClF_5 and then $C_2H_2F_4$ during this time. I took part of the commissioning for both fills, and decommissioning for C_2ClF_5 (PICO-0.1 is still filled with $C_2H_2F_4$).
My studies on the Seitz threshold provided a new understanding of it, and the detection of proton recoils and operation of PICO-0.1 with $C_2H_2F_4$ paved the way for potential new dark matter searches at low WIMP mass with PICO-40L or maybe even PICO-500.

To a lesser extent, I participated in the commissioning of PICO-60 (run 2) and PICO-40L: I spent one week underground to help for the commissioning of PICO-60 during the summer of 2016, and I spent one week in the clean room at SNOLAB during the fall 2017, cleaning parts of PICO-40L for the assembly.

Finally as a side project, in collaboration with Fabrice Debris, I also built a PICASSO C_3F_8 detector, to make calibrations at very low threshold and acoustics studies at low frequencies.

INTRODUCTION

Since more than 80 years and still as of today, dark matter has been one of the most intriguing mysteries of physics. It constitutes almost 85% of all the matter density in the Universe, but still hasn't been directly detected yet - only cosmological effects were observed. Lots of efforts are ongoing around the world to try to detect a dark matter particle interaction with ordinary matter, through many different kinds of experiments and international collaborations.

PICO is one of those experiments, located 2 km under the surface of the Earth in the SNOLAB underground laboratory in Sudbury, Ontario. The PICO experiment uses the bubble chamber technology to try to find dark matter, by detecting extremely low-energy interactions with the nuclei of its active fluid in a superheated state. Being able to reduce considerably and understand perfectly its background, PICO is currently one of the world-leading experiments for the direct detection of dark matter. Lately, PICO has had two dark matter search detectors, PICO-2L (a 2-litre bubble chamber) and PICO-60 (a 40-litre bubble chamber); two detectors are currently under construction (PICO-40, a new-design 40-litre bubble chamber planned to run in early 2019) or design (PICO-500, a 500-litre bubble chamber planned to run in 2020); and a number of small chambers are running in different institutions to make different calibrations, design testing, or any kind of small-scale tests to eventually put to use at larger scale. PICO-0.1 is one of these calibration chambers; it is a 75mL bubble chamber located at the University of Montreal since its commissioning in 2012. PICO-0.1 is the main subject of this thesis; chapters 5 and

6 present data and analysis of measurements made with this detector.

Before arriving to measurements and analysis, chapters 1 and 2 will introduce the concept of dark matter; its definition and implications, evidences of its existence, and potential candidate particles that could make up for it. Chapter 3 will detail the three different families of dark matter detection techniques: direct detection, indirect detection and production. The main experiments in each of them, and their particular physics and detection technique, will also be presented. Finally, chapter 4 will describe precisely the PICO experiment, its theory and functioning, as well as its main detectors; the transition to PICO-0.1 and its measurements will be made.

Chapter 5 will present a study of the Seitz threshold - theoretical energy threshold for an event to occur in a bubble chamber - with a monoenergetic reaction in C_2ClF_5, $^{35}Cl(n_{th},p)^{35}S$ producing a 17 keV ^{35}S recoil inside the detector. Chapter 6 will detail the successful detection of proton recoils in PICO-0.1 - which was never done in any PICO detector - and the calibration of PICO-0.1 with $C_2H_2F_4$ as its active fluid.

Chapter 1

DARK MATTER IN THE UNIVERSE

As of today's knowledge, dark matter accounts for about 84.5% of all the gravitational mass density in the Universe, and about 26.8% of all the Universe itself (mass and energy densities). While it still has to be directly detected, it was inferred through numerous astronomical observations, whether from gravitational effects or studies of the cosmological microwave background.

This chapter discusses dark matter in the frame of the Lambda Cold Dark Matter model: what is dark matter and what does it do (or does not), and how do we know it exists.

1.1. Dark matter

The name dark matter originates from the fact that it is a type of matter that does not interact electromagnetically; it does not absorb, emit, or reflect any light from the whole electromagnetic spectrum, making it nearly impossible to be detected directly through classical astronomical observation techniques. We were able to observe only its effects on gravity in the cosmos (section 1.2), implying that it inevitably has a mass. However, we don't know much more about dark matter: we know that it has a mass (it has gravitational effects), it is electrically neutral (or it would interact with photons), it is stable, and it is cold (non-relativistic). These characteristics for dark matter all fit in the cosmological

standard model, the Lambda Cold Dark Matter (ΛCDM) model.

1.1.1. The Lambda Cold Dark Matter model

The ΛCDM model is a cosmological model that describes the Universe, from its earliest moments (the Big Bang) up until today. It considers a cosmological constant $\Lambda \neq 0$ attributing an energy density to the vacuum, causing the Universe to expand. The Λ constant can in fact be given in terms of the vacuum energy density, as

$$\Lambda = \frac{8\pi G}{c^2}\rho_v \ , \tag{1.1.1}$$

where ρ_v is the vacuum energy density. It enters into the description of spacetime by adding a term into Einstein's field equations of general relativity [1]:

$$R_{\mu\nu} - \frac{1}{2}g_{\mu\nu}R + \Lambda g_{\mu\nu} = \frac{8\pi G}{c^4}T_{\mu\nu} \tag{1.1.2}$$

where $R_{\mu\nu}$ and R are the Ricci curvature tensor and scalar, $g_{\mu\nu}$ is the spacetime metric and $T_{\mu\nu}$ is the stress-energy tensor. Assuming homogeneity and isotropy of the Universe, one can find the metric that solves 1.1.2, and its spacetime element. The latter is given by:

$$ds^2 = -c^2dt^2 + a(t)^2\left(\frac{dr^2}{1-kr^2} + r^2d\Omega^2\right) \tag{1.1.3}$$

where $a(t)$ is called the scale factor and describes space expansion or shrinkage as it increases or decreases with time t, while k describes the spatial curvature and can take values $k = +1, 0, -1$; $k = +1$ is a closed universe, $k = 0$ is a flat universe and $k = -1$ is an open universe, as shown on figure 1.1. This metric is called the Friedman-Roberston-Walker (FRW) metric.

Solving Einstein's field equations 1.1.2 with this metric leads to Friedman's equation:

$$\left(\frac{\dot{a}}{a}\right)^2 + \frac{k}{a^2} = \frac{8\pi G}{3}\rho + \frac{\Lambda c^2}{3} \tag{1.1.4}$$

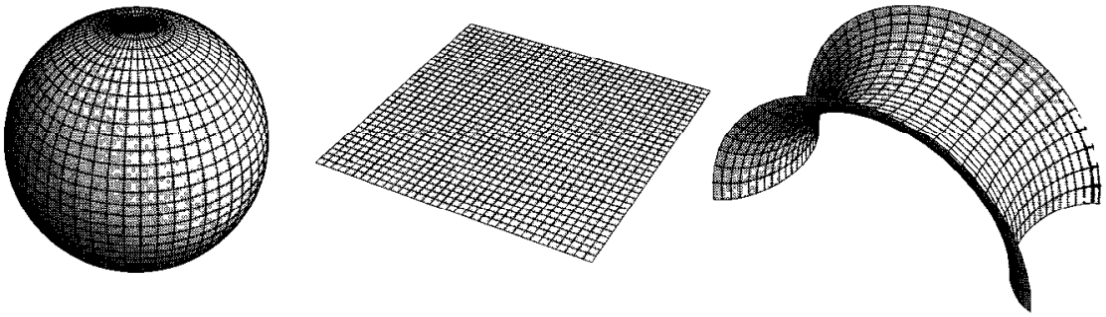

FIG. 1.1. 2D representations of 3D space sections, for closed (left), flat (center) and open (right) geometries [1].

where $\dot{a}$ is the time derivative of the scale factor a and ρ is the total (average) matter energy density of the Universe. This allows to conveniently introduce the Hubble constant

$$H_0 \equiv \frac{\dot{a}(t_0)}{a(t_0)} \tag{1.1.5}$$

where t_0 is the present time. The Hubble constant gives the expansion rate of the Universe, and its current most precise observed value is [2]

$$H_0 = 67.74 \pm 0.46 \text{ (km/s)/Mpc} = (2.195 \pm 0.015)\text{x}10^{-18} \text{ s}^{-1} \ . \tag{1.1.6}$$

Considering a flat ($k = 0$) universe, the present density of a flat FRW model is called the critical density and is given by

$$\rho_{crit} \equiv \frac{3H_0^2}{8\pi G} = (3.926 \pm 0.027)\text{x}10^{-9} \text{ kg/m}^3 \ . \tag{1.1.7}$$

This total density can then be separated in three parts: matter, radiation and vacuum energy. Their respective fraction can be defined as

$$\begin{aligned} \Omega_m &\equiv \frac{\rho_m(t_0)}{\rho_{crit}} \\ \Omega_r &\equiv \frac{\rho_r(t_0)}{\rho_{crit}} \\ \Omega_v \equiv \Omega_\Lambda &\equiv \frac{\rho_v(t_0)}{\rho_{crit}} \ . \end{aligned} \tag{1.1.8}$$

Geometry	Curvature	Density	Relative density
Open	$k = -1$	$\rho < \rho_c$	$\Omega < 1$
Flat	$k = 0$	$\rho = \rho_c$	$\Omega = 1$
Closed	$k = +1$	$\rho > \rho_c$	$\Omega > 1$

TAB. 1.1. Types of universes, their geometries and parameters.

where $\Omega \equiv \Omega_m + \Omega_r + \Omega_v = 1$, still for a flat FRW model. From this and by normalizing $a(t_0) = 1$, we can find the expression for $a(t)$ for different cases of type-dominated universes:

- Matter dominated, $\Omega_m = 1$, $\Omega_r = 0$, $\Omega_v = 0$:

$$a(t) = \left(\frac{t}{t_0}\right)^{2/3} \tag{1.1.9}$$

- Radiation dominated, $\Omega_m = 0$, $\Omega_r = 1$, $\Omega_v = 0$:

$$a(t) = \left(\frac{t}{t_0}\right)^{1/2} \tag{1.1.10}$$

- Vacuum dominated, $\Omega_m = 0$, $\Omega_r = 0$, $\Omega_v = 1$:

$$a(t) = e^{H(t-t_0)} \tag{1.1.11}$$

  where

$$H^2 \equiv \frac{8\pi G}{3}\rho_v = \frac{\Lambda c^2}{3} \tag{1.1.12}$$

More generally, for any flat, open or closed universe, we get the expression for Ω:

$$\Omega - 1 = \frac{k}{H_0^2 a^2} \tag{1.1.13}$$

meaning that that k, and therefore the geometry of space, is determined by whether Ω is greater, equal to, or smaller than 1. Relating this to the density of the Universe ρ and the critical density ρ_{crit}, table 1.1 summarizes each type of Universe and its parameters.

The matter energy density Ω_m can be separated into two parts, $\Omega_m = \Omega_b + \Omega_c$, where Ω_b is the fraction of baryonic matter and Ω_c the fraction of dark matter. From equations 1.1.1, 1.1.7 and 1.1.8, one can rewrite the expression for Λ in terms of observable parameters:

Parameter	Value
H_0	$(2.195 \pm 0.015)\text{x}10^{-18}$ s^{-1}
Ω_Λ	0.6911 ± 0.0062
Ω_m	0.3089 ± 0.0062
Ω_b	0.04860 ± 0.00073
Ω_c	0.2590 ± 0.0041
Λ	$(1.110 \pm 0.018)\text{x}10^{-52}$ m^{-2}

TAB. 1.2. Observed values of cosmological parameters [2] and calculated value of the cosmological constant Λ.

$$\Lambda = \frac{8\pi G}{c^2}\rho_{crit}\Omega_\Lambda = \frac{3H_0^2\Omega_\Lambda}{c^2} \ . \tag{1.1.14}$$

All observed cosmological parameter values are summarized in table 1.2, along with the calculated value of Λ from 1.1.14. According to these observed values, some important observations can be done in the frame of the ΛCMD model, especially from the energy density fractions: first, assuming $\Omega = 1$, $\Omega_\Lambda = 0.6911 \pm 0.0062$ and $\Omega_m = 0.3089 \pm 0.0062$ means that only 30.89% of the Universe is matter (baryonic and dark matter), while 69.11% is what is called dark energy - vacuum energy density; second, $\Omega_b = 0.04861 \pm 0.00031$ and $\Omega_c = 0.2590 \pm 0.0022$ means that baryonic matter constitutes only about 4.86% of the Universe, while dark matter makes up for about 25.90% - this also means that about 84% of all matter is dark matter, while only about 16% is baryonic (ordinary) matter.

The ΛCDM describes really well a dark matter-containing universe and its evolution, and is furthermore supported by multiple astrophysical observations. Observational evidences of the existence of dark mtter are presented in the next section.

1.2. Evidences for dark matter

Since the beginning of the 20$^{\text{th}}$ century, dark matter has been at the center of attention for astrophysicists and astroparticle physicists. It was first hypothesized in the 1920-30's,

and then observed and studied in more and more precise ways throughout the years, from the 1960's to today. This section presents different evidences of the presence of dark matter in outer space.

1.2.1. Galaxy rotation curves

First to suggest the existence of dark matter were Dutch physicists Jacobus Kapteyn in 1922 and Jan Oort in 1932, by observing the rotation velocities of stars in the Milky Way [3, 4]. However, it was Swiss astronomer Fritz Zwicky in 1933 who hypothesized it in a more precise and quantitative way, when he studied the motion of galaxies in the Coma Cluster and found out, by applying the virial theorem

$$\langle E_k \rangle = -\frac{1}{2}\langle E_p \rangle \ , \tag{1.2.1}$$

- with $\langle E_k \rangle$ and $\langle E_p \rangle$ the time averaged kinetic and potential energy - that there was a lot of unseen mass having large gravitational effects [5]. By comparing the mass needed for galaxies near the edges of the cluster to have their observed velocities (from classical mechanics) with the one obtained from the estimated brightness and number of galaxies, he concluded that there was 400 times more mass than what could be visually observed (from the light of stars and galaxies). His estimation later proved to be inaccurate in its value, but his statement was right: there was a lot more matter than what could be seen.

It was only about 40 years later that Zwicky's statement was confirmed and more precisely measured. During the 1960's and 1970's, American astronomer Vera Rubin measured the velocity curves of spiral galaxies and found out, like Zwicky, that there had to be more mass than observed for the stars on the edges to obtain their velocities [6]. According to Newtonian mechanics, the velocity curve for orbiting stars should follow

$$v = \sqrt{\frac{GM(r)}{r}} \tag{1.2.2}$$

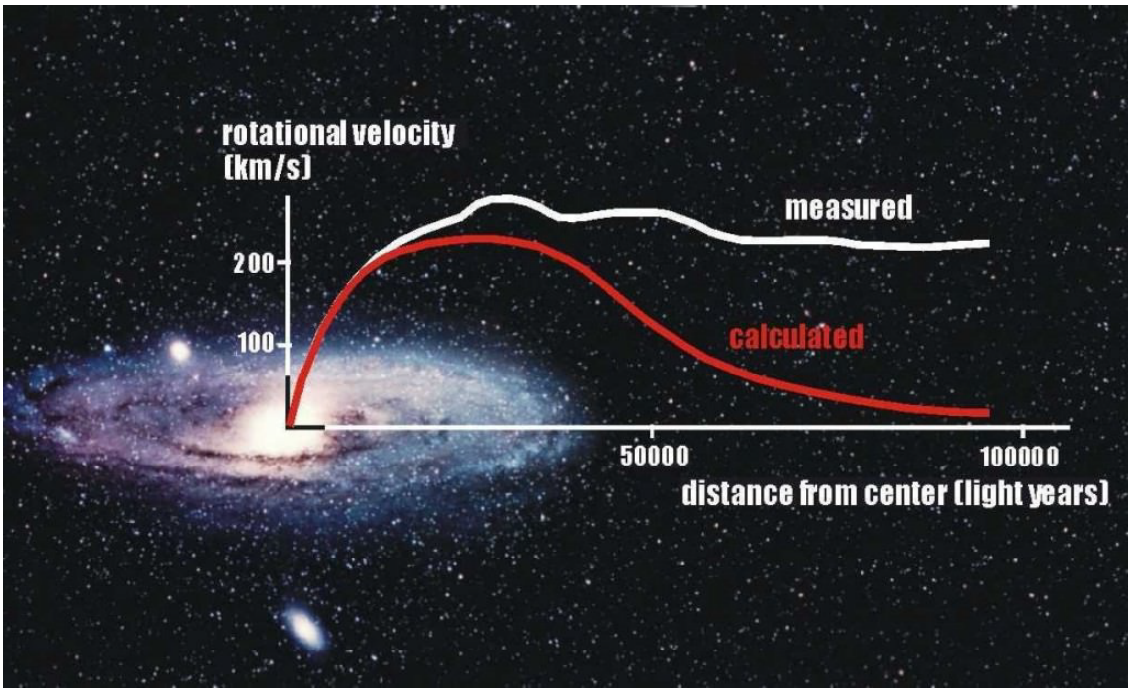

FIG. 1.2. Andromeda galaxy rotation (velocity) curve, expected (red) vs. measured (white) [7]. Stars far from the center of the galaxy have much higher velocities than expected from Newtonian mechanics, indicating that there is more mass than observed from the luminous disk.

where $M(r)$ is the mass of the galaxy contained inside radius r. Near the edge of a galaxy, one can consider $M(r) \approx M_{galaxy}$, and therefore a velocity curve going as $v \sim \sqrt{1/r}$ would be expected. However, this is not what was observed, as shown on figure 1.2. By studying more than 80 galaxy rotation curves, Rubin concluded that for most of them, there had to be about six times more dark matter than luminous matter.

1.2.2. Gravitational lensing

As a consequence of general relativity, a light path can be bent around a massive object due to its deformation of spacetime. A bright object can therefore appear multiple times around an intermediate object, by the phenomenon of gravitational lensing; figure 1.3 illustrates this concept.

Using the Schwarzchild geometry and its spacetime element

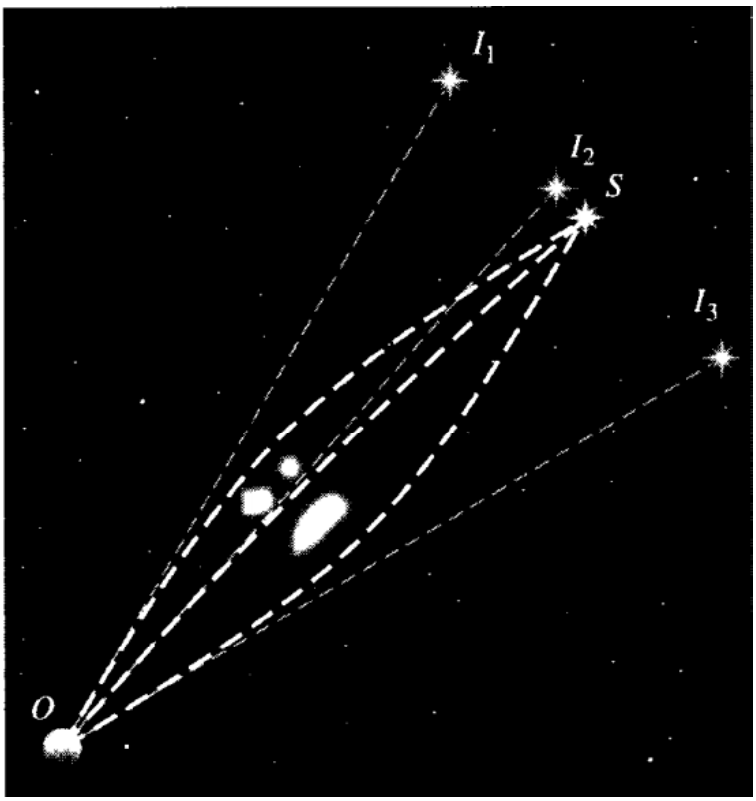

FIG. 1.3. Illustration of gravitational lensing [1]. A light source S emits light rays towards an observer O, bent by an intermediate mass. For the observer O, S appears at different points I_1, I_2 and I_3.

$$ds^2 = -\left(1 - \frac{2GM}{c^2 r}\right)(c\,dt)^2 + \left(1 - \frac{2GM}{c^2 r}\right)^{-1} dr^2 + r^2 d\Omega^2 \tag{1.2.3}$$

to calculate orbits or deflections of light rays around massive objects, one can derive the effective potential which photons are subject to [1]:

$$W_{\mathit{eff}}(r) = \frac{1}{r^2}\left(1 - \frac{2GM}{c^2 r}\right) . \tag{1.2.4}$$

Defining the impact parameter b:

$$b \equiv \left|\frac{lc}{e}\right| \tag{1.2.5}$$

with l and e the angular momentum and energy of the light ray at infinity (where the spacetime curvature due to the massive object vanishes and spacetime is flat), we can find three different kinds of light ray orbits, depending on $1/b^2$ compared to the maximum of

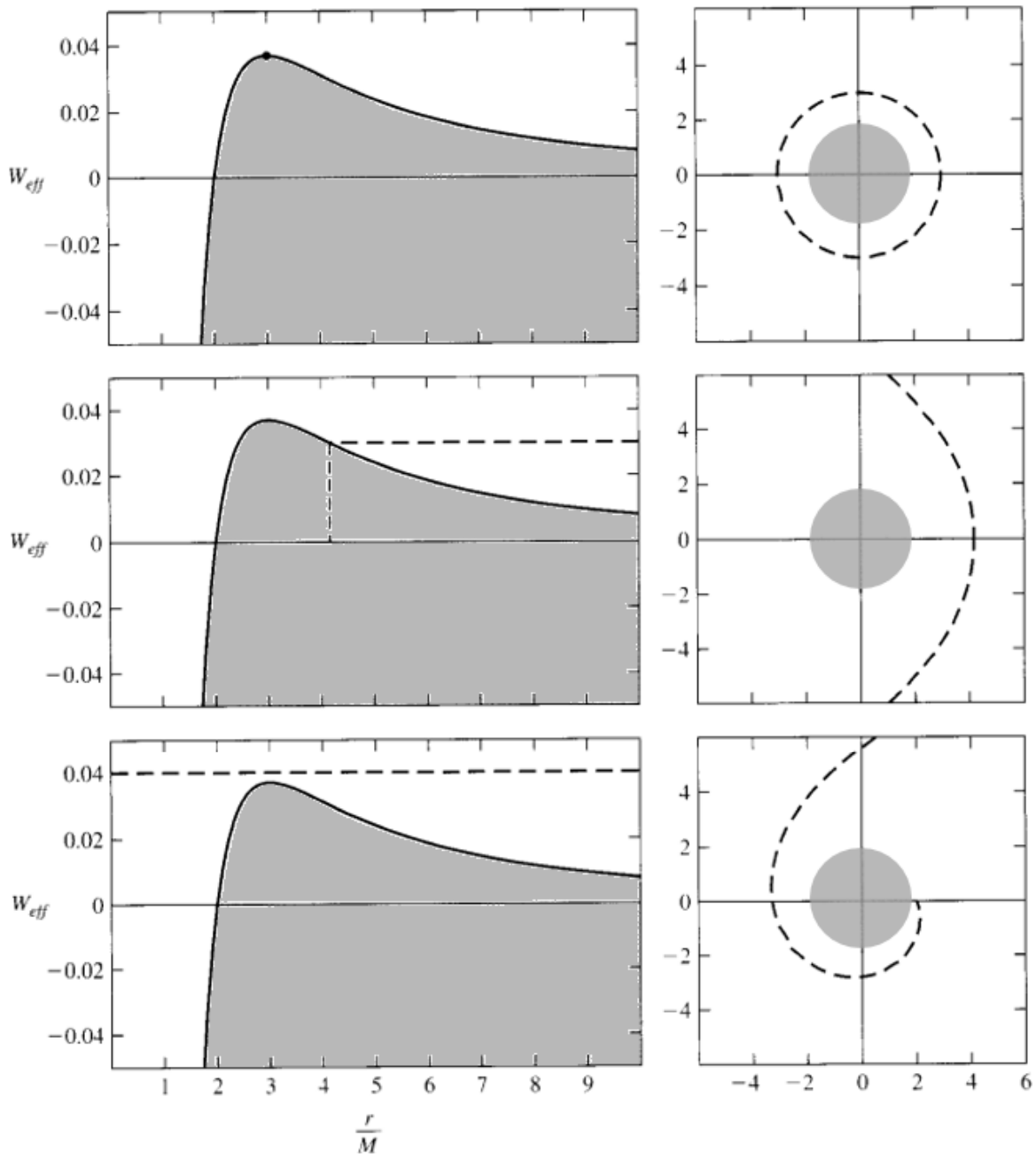

FIG. 1.4. Three different kinds of light rays orbits, depending on $1/b^2$ compared to the maximum of W_{eff}, i.e. $W_{eff}(3GM/c^2) = c^4/27G^2M^2$ [1]. At the top, $1/b^2 = W_{eff}(3GM/c^2)$; in the middle, $1/b^2 < W_{eff}(3GM/c^2)$; at the bottom, $1/b^2 > W_{eff}(3GM/c^2)$. $1/b^2$ is shown with dashed lines (or a dot) on the left, compared to W_{eff} as a function of c^2r/GM (r/M in $c = 1$ units). The shape of the corresponding light ray orbit is shown on the right.

W_{eff}, as shown on figure 1.4.

Given this, one can find the deflection angle α of a light ray passing by a mass M at an impact parameter $b \gg GM/c^2$:

$$\alpha = \frac{4GM}{c^2 b} \ . \tag{1.2.6}$$

Observations of gravitational lensing can then provide an estimate of the mass of an intermediate object between a light source and an observer. This technique is therefore used to estimate the mass of galaxies/clusters of galaxies providing gravitational lensing of other luminous objects behind them. By comparing the mass obtained to the estimated mass from the luminous bulk, one can deduce the mass of dark matter contained in the galaxy/cluster of galaxies.

1.2.2.1. *Bullet Cluster*

The most famous evidence of dark matter obtained through gravitational lensing is the observation of a collision between two clusters of galaxies, known together as the Bullet Cluster. As the two clusters are colliding, stars from the galaxies (far from one another) are not really affected and continue their way through the collision, only slightly slowed down due to gravitational effects. On the other hand, hot interstellar gases from the two clusters (most of their baryonic matter) interact electromagnetically, causing them to be slowed down much more than the stars. Therefore, most of the mass of the colliding clusters should be slowed down and trail behind each of the two unaffected clusters of stars, but gravitational lensing showed otherwise: the strongest lensing - i.e. most of the mass - came from the regions of the two clusters [8]. This observation is shown on figure 1.5. It thus suggests that there is more than the visible mass in the clusters of galaxies, that was electromagnetically unaffected in the collision - as of the visible mass - : neutral, massive dark matter.

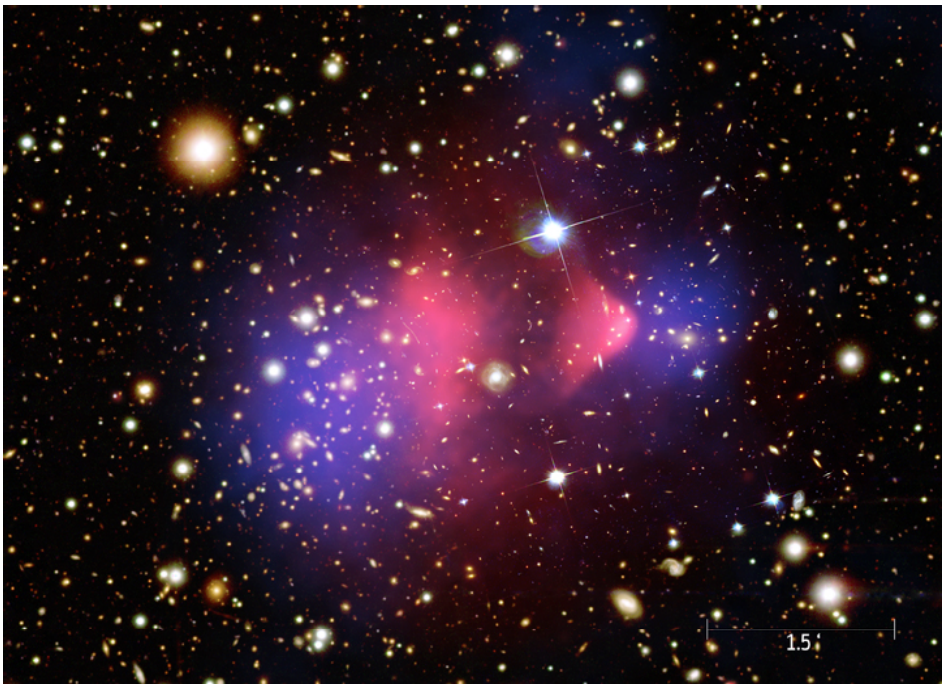

FIG. 1.5. Colorized data the bullet cluster collision [9]. In red is the X-ray light coming from hot interstellar gases; in blue is the reconstructed mass from gravitational lensing. Most of the mass comes from the two regions ahead of the interstellar gases, coincident with the visible galaxies.

1.2.3. Cosmic microwave background

From as early as 10^{-6} seconds after the Big Bang to about 378 000 years later, the Universe was a hot plasma of protons, electrons and photons. It was so dense that photons could only travel very short distances before scattering, making it opaque as well. As the Universe was expanding, it was also cooling down. About 378 000 years after the Big Bang, a time known in cosmology as the epoch of recombination, the Universe had cooled enough so that free protons and electrons were able to combine to form neutral hydrogen. Photons could then travel freely throughout the Universe, as they were being decoupled from matter. These relic photons are still observable today as the Universe background radiation (not associated with any star, galaxy or other cosmic object), called the cosmic microwave background (CMB).

The Universe's background radiates as a black body, at a temperature of 2.72548 ± 0.00057 K [10]. It is almost perfectly isotropic, with anisotropies of only a few parts in 10^5

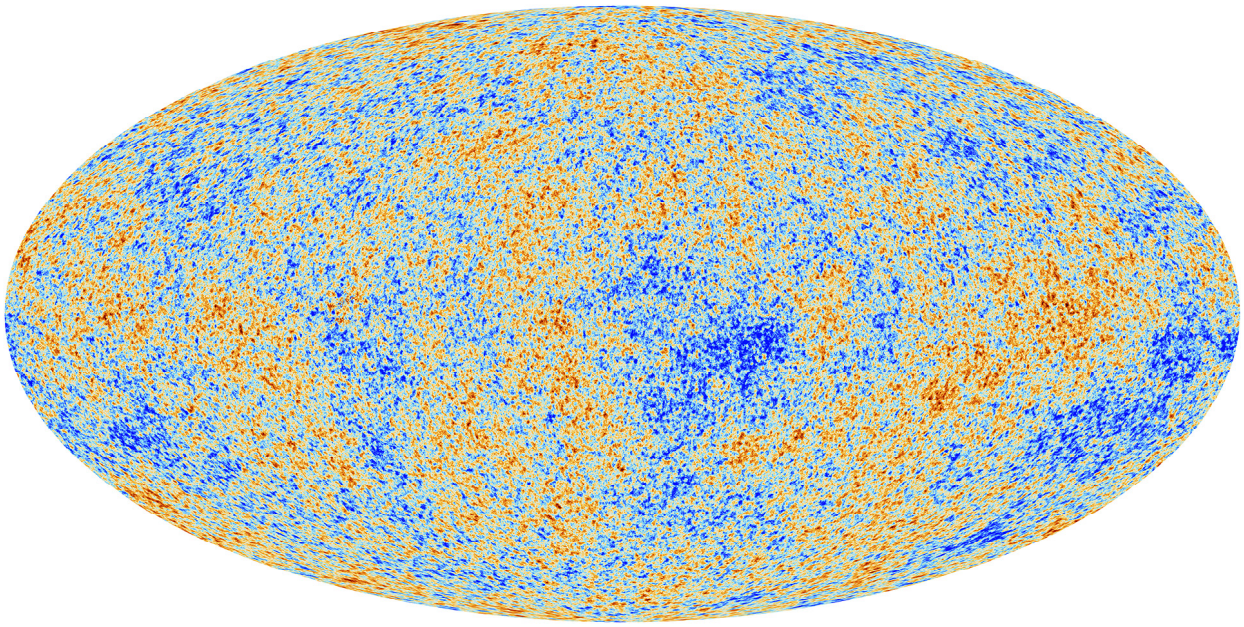

FIG. 1.6. Cosmic Microwave Background anisotropy map, as measured by the Planck space observatory in 2013 [11].

(a few μK over 2.73 K). Its anisotropies have been measured most precisely by the Planck spacecraft in 2013, as shown on figure 1.6. This temperature map can be decomposed into a sum of spherical harmonics Y_{lm} with coefficients a_{lm}, as

$$T(\theta,\phi) = \sum_{l=0}^{\infty} \sum_{m=-1}^{l} a_{lm} Y_{lm}(\theta,\phi) \ . \tag{1.2.7}$$

Temperature deviations ΔT can then be written in terms of the angular momentum l:

$$\Delta T^2 = \frac{l(l+1)C_l}{2\pi} \tag{1.2.8}$$

with coefficients

$$C_l = \frac{1}{2l+1} \sum_{m=-l}^{l} |a_{lm}|^2 \ . \tag{1.2.9}$$

The measured temperature power spectrum as a function of the angular momentum is shown on figure 1.7, where we can observe a series of so called "acoustic" peaks. These peaks all have their physical significance: the (angular) position of the first peak indicates a flat Universe (section 1.1.1), while its amplitude, compared to the second and third peaks, give

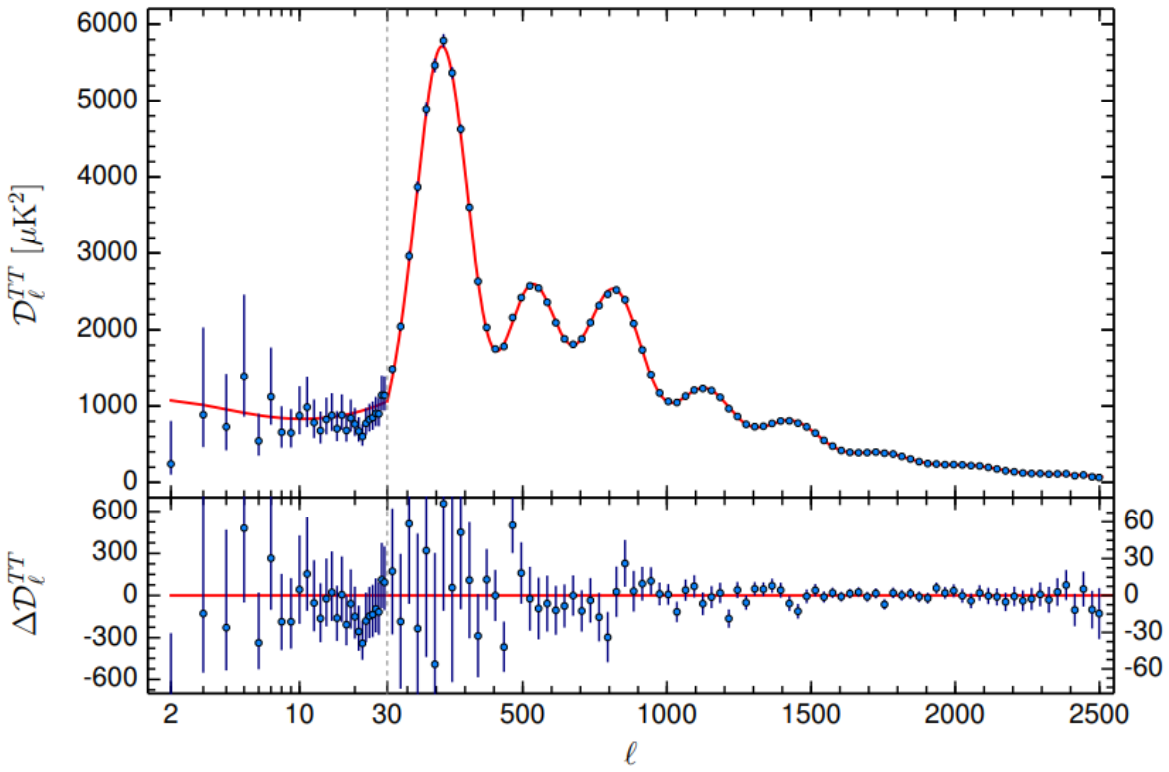

FIG. 1.7. Planck 2015 temperature power spectrum, D_ℓ^{TT} ($= \Delta T^2$) in function of the angular momentum ℓ [2]. Thick line is the theoretical fit from the ΛCDM model.

information on the baryon and dark matter density (and therefore Ω_b and Ω_c), respectively. The results obtained (1.2) agree really well with the ΛCDM model and are hardly explained otherwise, providing powerful evidence of the presence of dark matter in the Universe.

Chapter 2

DARK MATTER CANDIDATES

As detailed in the previous chapter, the presence of dark matter in the Universe is well documented and hardly refutable. What is still unknown about it are its constituents; is there a dark matter particle? If so, what is it made of, what are its properties? Multiple candidates were proposed since the postulate of dark matter; many of them were practically excluded. The main current candidates are presented in this chapter.

2.1. Axions

Axions were theorized in 1977 by Roberto Peccei and Helen Quinn, as a solution to the strong CP problem, i.e. that the strong interaction has close to zero charge-parity (CP) violation, which seems quite unnatural as quantum chromodynamics allow such violation. Their model, known as the Peccei-Quinn model, introduces a new global $U(1)$ symmetry to the QCD Lagrangian through a CP-violating term θ [12]. This symmetry is broken at low energies (below about 100 MeV), suggesting that there would be a very light scalar boson, the axion. Axions would be spinless, chargeless particles, acquiring a small mass m_a from non-perturbative QCD effects:

$$m_a \approx 0.62 \left(\frac{10^7 \text{ GeV}}{f_a} \right) \text{ eV}(/\text{c}^2) \ , \tag{2.1.1}$$

where f_a is the $U(1)$ symmetry breaking scale ($c = 1$ units will be used in this chapter). At the level of a few μeV of mass, axions could be good dark matter candidates. According to Peccei [13], with calculations from astrophysical observations, notably the Wilkinson Microwave Anisotropy Probe [14], the axion mass is bounded between

$$2.1\text{x}10^{-5}\ \text{eV} < m_a \leq 10^{-3}\ \text{eV}\ . \tag{2.1.2}$$

In 2016, with the Fermi Large Area Telescope, Berenji et al. obtained an upper limit on the axion mass of 0.079 eV experimental, at a 95% confidence level [15].

2.2. Sterile neutrinos

Sterile neutrinos are different from the Standard Model neutrinos in that they don't interact by any Standard Model interaction; they only interact by gravity. They could be right-handed neutrinos (spin parallel to momentum), which still have to be observed, in opposition to the Standard Model left-handed neutrinos.

For the neutrinos to obtain mass in the Standard Model, one can add a Dirac mass (m_D) term to the Lagrangian [16]:

$$\mathcal{L}_D = -m_D(\overline{\nu_R}\nu_L + \overline{\nu_L}\nu_R) \tag{2.2.1}$$

where the D subscript indicates Dirac fermions (solutions to the Dirac equation), and the R and L are the right- and left-handed chiral states. This mass term would imply that right-handed chiral neutrinos exist. However, as the neutrino masses are extremely small compared to other Standard Model fermions, this would suggest that they obtain their mass through another mechanism.

As they transform as singlets under the Standard Model gauge transformations, one

can introduce right-handed neutrinos (and left-handed anti-neutrinos) in the Lagrangian by adding a gauge-invariant Majorana mass (M) term:

$$\mathcal{L}_M = -\frac{1}{2} M(\overline{\nu_R^c}\nu_R + \overline{\nu_R}\nu_R^c) \tag{2.2.2}$$

where ν_R^c is the CP conjugate of the right-handed neutrino, i.e. the left-handed anti-neutrino. We can then combine the two mass terms to obtain the combined Lagrangian

$$\mathcal{L}_{DM} = -\frac{1}{2}\left[m_D\overline{\nu_L}\nu_R + m_D\overline{\nu_R^c}\nu_L^c + M\overline{\nu_R^c}\nu_R\right] + h.c. \tag{2.2.3}$$

with $h.c.$ the hermitian conjugate, or, equivalently:

$$\mathcal{L}_{DM} = -\frac{1}{2}\begin{pmatrix}\overline{\nu_L} & \overline{\nu_R^c}\end{pmatrix}\begin{pmatrix}0 & m_D \\ m_D & M\end{pmatrix}\begin{pmatrix}\nu_L^c \\ \nu_R\end{pmatrix} + h.c. \tag{2.2.4}$$

This Lagrangian therefore provides six neutrino fields (three for each ν_L and ν_R), thus a 6 x 6 mixing matrix and six mass eigenstates. In the limit $M \gg m_D$, we obtain the mass eigenstates

$$m_\pm \approx \frac{1}{2}M \pm \left(M + \frac{2m_D^2}{M}\right) \ , \tag{2.2.5}$$

providing a light neutrino state (ν) and a heavy neutrino state (N) with masses

$$m_\nu \approx \frac{m_D^2}{M} \quad \text{and} \quad m_N \approx M \ . \tag{2.2.6}$$

The neutrino states would then be:

$$\nu \approx (\nu_L + \nu_L^c) - \frac{m_D}{M}(\nu_R + \nu_R^c) \quad \text{and} \quad N \approx (\nu_R + \nu_R^c) + \frac{m_D}{M}(\nu_L + \nu_L^c) \tag{2.2.7}$$

where we can see that the light neutrino is almost entirely left-handed, the right-handed part being largely suppressed by m_D/M; same goes for the heavy neutrino, almost entirely right-handed with the left-handed part suppressed by m_D/M.

Thus, heavy right-handed Majorana neutrino masses M seem to motivate very light neutrino mass values; considering a Dirac mass of the order of the mass of other fermions, say $m_D \sim 1$ GeV, light neutrinos would obtain a mass of $m_\nu \sim 0.01$ eV,s consistent with the current limits on neutrino masses. Heavy neutrinos would get a mass of $m_N \approx M \sim 10^{11}$ GeV.

However, the three heavy mass states could have much smaller masses, of the order of MeV or keV; in that case, they're referred as sterile neutrinos [17]. Sterile neutrinos are candidate particles for dark matter, as they are chargeless and potentially massive enough to produce the gravitational effects we observe. They can be produced by oscillation from light neutrinos or from particle decays.

From the 6 x 6 mixing matrix, they can oscillate (with small amplitudes) to light neutrinos, providing potential excess in observed neutrino fluxes compared to what is expected from the Standard Model; we could detect them this way, and maybe deduce the detection of dark matter. In 2018, the MiniBooNE experiment has observed a 4.8σ excess in ν_e flux from a short-baseline neutrino experiment at Fermilab, for a total 6.1σ excess combined with the previous results from LNSD [18]. These results could pave the way for evidences of sterile neutrinos.

2.3. WIMPs

The most common hypothetical candidates for dark matter particles are called WIMPs, *Weakly Interacting Massive Particles*. WIMPs would be neutral, stable, non-relativistic particles beyond the Standard Model, that would only interact by gravity (as observed), and possibly by the weak nuclear force (still to be observed), or another force still unknown to physicists with an interaction cross-section of an order not higher than the weak scale. WIMPs are predicted to have a mass between 1 GeV and 100 TeV.

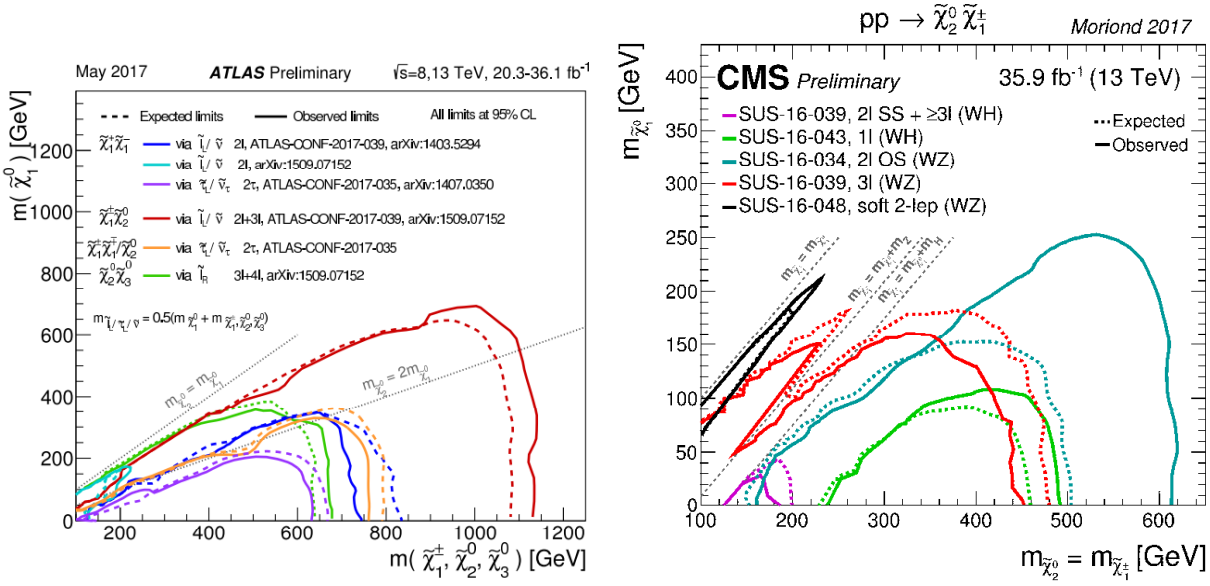

FIG. 2.1. Exclusion limits on neutralinos and chargino masses, obtained by LHC experiments at CERN [19]. On the left, limits for pair production of charginos, pair production of heavier neutralinos, or pair production of chargino and neutralino, assuming light sleptons (lepton supersymmetric partner) mediating the decays. On the right, limits for pair production of chargino and neutralino, assuming decoupled sleptons, and chargino/neutralino decay through W^*, Z^* or H.

WIMPs are well motivated by the most popular theoretical extensions to the Standard Model, supersymmetry (SuSy). They are predicted to be the lightest supersymmetric particle (LSP), likely the neutralino ($\tilde{\chi}^0$). Searches for SuSy and neutralinos are ongoing, particularly in particle accelerators experiments. No SuSy particle has been discovered yet. As of 2017, exclusion limits on the neutralino ($\tilde{\chi}^0_1$ being the lightest, $\tilde{\chi}^0_2$ and $\tilde{\chi}^0_3$ being heavier neutralinos) and chargino ($\tilde{\chi}^\pm$, another SuSy particle) masses have been set; they are presented on figure 2.1.

WIMP detection searches are also very active, as discussed in the next chapter.

Chapter 3

DARK MATTER DETECTION PRINCIPLES

Even though the existence of dark matter has been provided strong evidence (chapter 1), as well as its presence in considerable amounts in the universe, the detection of a dark matter particle is still lacking. We "saw" dark matter through its gravitational effects, but still have not detected it as a single particle. There is a lot of things we still don't know about dark matter, such as its interactions, its mass, its quantum properties, etc. Detection of dark matter would help determine these kinds of properties.

Dark matter detection uses three different techniques: direct detection (§3.1), searching for dark matter scattering (with ordinary matter); indirect detection (§3.2), searching for dark matter annihilation (with itself); and dark matter production (§3.3), from collisions between ordinary matter. Many experiments around the world are searching for dark matter in these three different fields.

The above mentioned techniques for detection of dark matter are easily visualized through a Feynman diagram of dark matter interactions, as shown on figure 3.1: direct detection searches for scattering between a dark matter particle and an ordinary matter particle, as described by reading the diagram downwards; indirect detection searches for two dark matter particles annihilating into two particles of ordinary matter, as described by reading the diagram from left to right; dark matter production looks for two particles of ordinary matter annihilating into two dark matter particles, as described by reading the

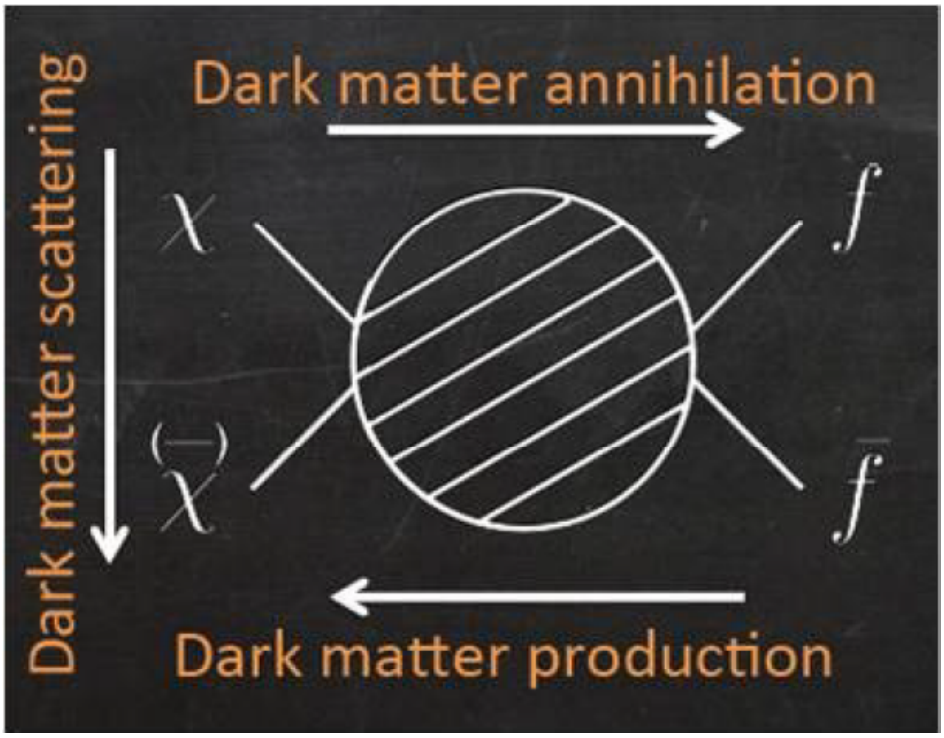

FIG. 3.1. Feynman diagram of dark matter (χ) interactions with ordinary matter (f).

diagram from right to left.

3.1. DIRECT DETECTION

Direct dark matter detection searches for direct interactions between dark matter and ordinary matter, i.e. scattering. This scattering will transfer energy to the ordinary matter particle, which can be detected. WIMP scattering on an atom nucleus will provide a recoil energy E_R given by:

$$E_R = 2E_\chi \frac{m_A m_\chi}{(m_A + m_\chi)^2}(1 - \cos\theta) \tag{3.1.1}$$

where E_χ is the energy of the WIMP, m_χ its mass, m_A the mass of the nucleus and θ the scattering angle, in the centre of mass frame. Considering the theoretical WIMP mass range, $1 - 10^5$ GeV/c^2, we can then expect nuclear recoils of the order of 1 to 100 keV. The differential event count rate in a dark matter detector, per unit mass, is given by:

$$\frac{dR}{dE_R} = \frac{R_0}{\langle E_R \rangle} e^{-E_R/\langle E_R \rangle} F^2(q) \tag{3.1.2}$$

where R_0 is the total WIMP interaction rate, $\langle E_R \rangle$ is the average recoil energy and $F(q)$ is the nuclear form factor of the detector target; each of these parameters can be calculated.

The total count rate (per target unit mass) can then be given by:

$$R_0 = \frac{2}{\sqrt{\pi}} \frac{N_A}{A} \frac{\rho_\chi}{m_\chi} \langle v_\chi \rangle \sigma_A \epsilon \tag{3.1.3}$$

where N_A is the Avogadro constant, A is the atomic mass of the target nucleus, ρ_χ is the WIMP local density, $\langle v_\chi \rangle$ its average velocity, σ_A is the interaction cross-section and ϵ is the detection efficiency. In average, dark matter is static throughout the galaxy. This means that in the solar system frame, its average velocity is that of the solar system around the galaxy, $\langle v_\chi \rangle \approx v_0 \approx 220$ km/s. Locally, in the earth frame, $\vec{v_\chi} = -\vec{v_0}$ becomes $\vec{v_\chi} = -\vec{v_0} - \vec{v}_{earth}$, with $\vec{v}_{earth}$ the earth vectorial orbital velocity around the Sun. Since the Earth velocity direction to the galaxy varies throughout the year, it will lead to oscillations of the WIMP wind over time, as illustrated on figure 3.2. If we were to detect dark matter, we could then observe an annual modulation of the WIMP signal over a year, peaking in June and reaching its minimum in December.

The average recoil energy $\langle E_R \rangle$ can be found by averaging eq. 3.1.1:

$$\begin{aligned} \langle E_R \rangle &= 2\langle E_\chi \rangle \frac{m_A m_\chi}{(m_A + m_\chi)^2} \langle 1 - \cos\theta \rangle \\ &= 2\frac{m_A m_\chi^2}{(m_A + m_\chi)^2} \langle v_\chi^2 \rangle \end{aligned} \tag{3.1.4}$$

with $\langle E_\chi \rangle = \frac{1}{2} m_\chi \langle v_\chi^2 \rangle$ the WIMP non-relativistic kinetic energy, and $\langle 1 - \cos\theta \rangle = 1 - \langle \cos\theta \rangle = 1 - 0 = 1$.

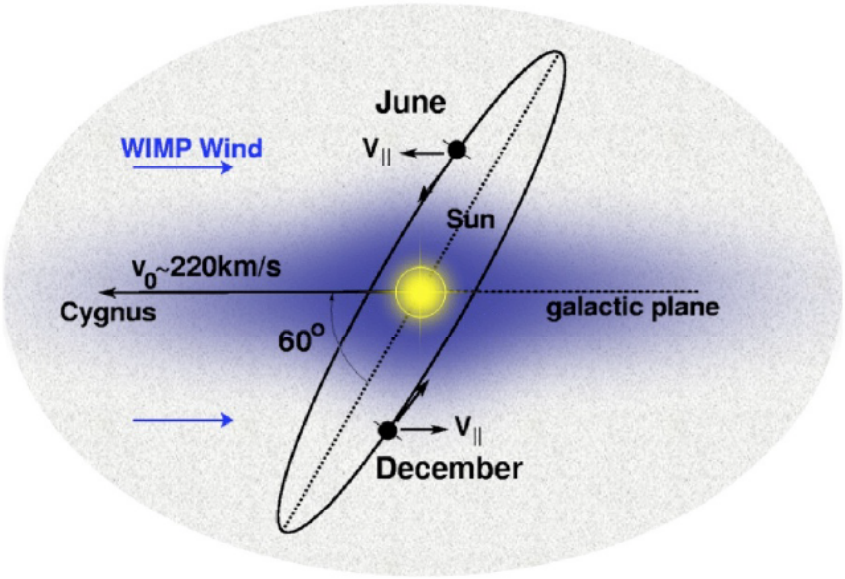

FIG. 3.2. WIMP wind in comparison with the earth orbital plane. The angle between the two gives a potential variation of the WIMP signal between summer and winter.

The WIMP-nucleus interaction cross-section σ_A can be written as [20]:

$$\sigma_A = 4G_F^2 \left(\frac{m_A m_\chi}{m_A + m_\chi} \right)^2 C_A \tag{3.1.5}$$

where G_F is the Fermi constant and C_A is a factor depending on the type of WIMP-nucleus interaction, whether it depends of the spin of both particles (spin-dependent interaction, SD) or not (spin-independent, SI). In the spin-dependent case, it is given by:

$$C_A^{SD} = \frac{8}{\pi} \lambda^2 J(J+1) \tag{3.1.6}$$

where J is the total spin of the nucleus and $\lambda = (a_p \langle S_p \rangle + a_n \langle S_n \rangle)/J$ is a factor depending on the expectation values of the proton and neutron spin, $\langle S_p \rangle$ and $\langle S_n \rangle$ respectively, with WIMP-coupling coefficients a_p and a_n.

The spin-independent case gives :

$$C_A^{SI} = \frac{1}{\pi G_F^2} (Z f_p + (A - Z) f_n)^2 \tag{3.1.7}$$

Nucleus	Z	J	λ^2
^{1}H	1	½	1
^{19}F	9	½	0.8627
^{23}Na	11	³⁄₂	0.0109
^{27}Al	13	³⁄₂	0.0099
^{35}Cl	17	³⁄₂	0.0096
^{73}Ge	32	⁹⁄₂	0.0026
^{127}I	53	⁵⁄₂	0.0026
^{131}Xe	54	³⁄₂	0.0147

TAB. 3.1. Target nuclei properties [20].

where f_p and f_n are the effective WIMP couplings to protons and neutrons. To maximize the cross-section (and therefore the chance of detecting dark matter), from 3.1.6 and 3.1.7, one would need a high λ factor for an SD-sensitive experiment, and heavy nuclei (high Z) for an SI-sensitive experiment. Table 3.1 gives Z, J and λ^2 for a few targets. Thus, experiments intending to be sensitive in the SD sector will opt for hydrogenated or fluorine targets, and SI experiments will choose heavier elements as target materials such as Si, Ge, I, Ar, Xe, etc.

3.1.1. Direct detection experiments

There are many experiments around the world that search for direct detection of dark matter. They use different techniques to detect interactions of dark matter with ordinary matter, based on three main principles: heat transfer, ionization and scintillation. In the first case, experiments will look for and try to detect energy transferred from the incoming WIMP to the detector target through elastic scattering, providing additional heat - sometimes in form of phonons - in the material. In the second case, experiments will search for extra charge in the detector, as the incoming WIMP ionizes the target material. Finally, in the third case, a WIMP would interact with the target, emitting electromagnetic radiation that can be detected. A summary of all the direct detection experiments and their detection techniques is shown in a diagram on figure 3.3.

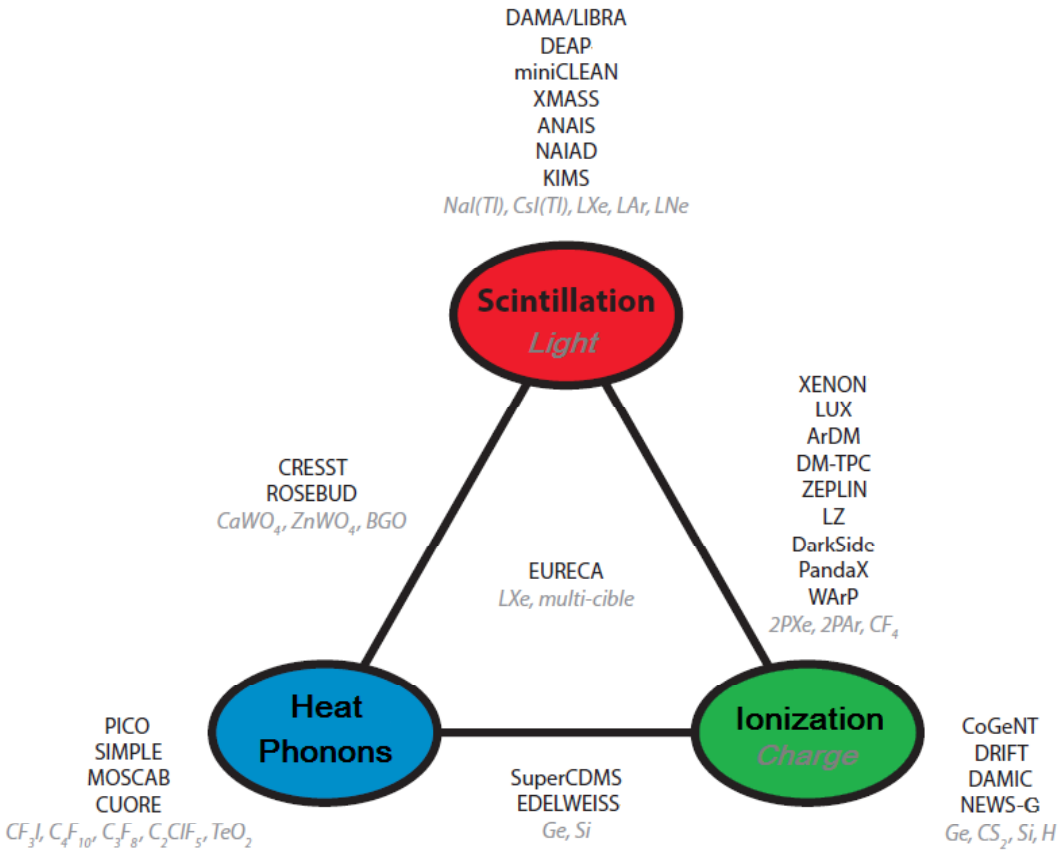

FIG. 3.3. Diagram of the dark matter direct detection experiments and their corresponding techniques.

Experiments looking for direct detection via heat transfer use mostly superheated fluids to detect energy depositions, such as PICO [21] (see chapter 4 for more details), MOSCAB [22] and SIMPLE [23]. Energy depositions in superheated fluids create phase transitions, which will be the main feature of this type of detectors (see section 4.1 for a more elaborate explanation). Other experiments, such as SuperCDMS [24], use semiconducting crystals to detect energy transfers through phonons, i.e. vibrations in the crystal lattice.

The SuperCDMS experiment combines the technologies of phonon detection and ionization. They use germanium and silicon semiconducting crystals at cryogenic temperatures that produce phonons, as well as electron-hole pairs, when interacting with an incoming particle. Figure 3.4 shows one detector of the array, along with a schematic representation of the experimental setup that will take place in SNOLAB, Sudbury, Ontario [25], for the next

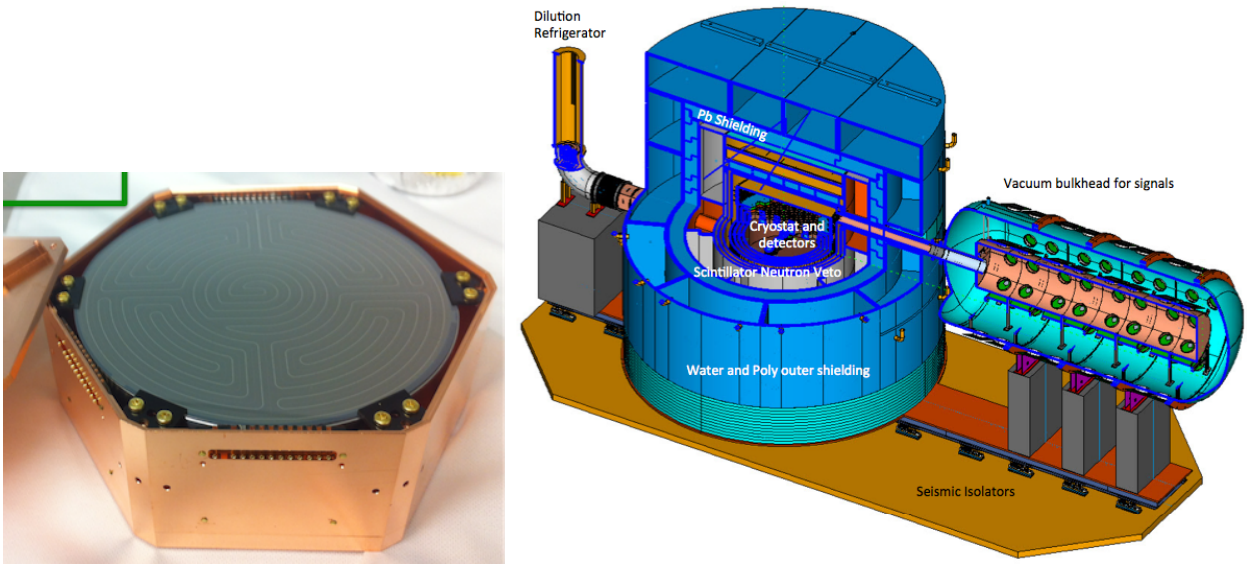

FIG. 3.4. One SuperCDMS detector, 76mm of diameter (left) and the experimental setup to take place in SNOLAB (right) [24].

dark matter search run of SuperCDMS. On top of each detector are superconducting bands that detect and measure the energy of the phonons, by measuring a drastic change in their resistivity when they absorb them: by putting superconductors at their critical temperature T_C, a small input of heat will increase their temperature above T_C, making them no longer superconductors. This principle is shown on figure 3.5. On both side of each detector are electrodes that create an electric field in the detector and collect the free charges that are drifted to them. Their energy is also measured, providing a phonon to ionization energy ratio that gives information on the type of particle that interacted in the detector. Indeed, while both neutral and charged particles will induce phonons when depositing energy in the detector, charged particle will induce much more ionization than neutral particles. This technique allows to identify different types of particles and potentially, WIMPs.

Experiments looking for ionization from WIMPs use easily ionized materials - often gases -, put inside high voltages. These gases collect a number of charges that is proportional to the energy of the incoming ionizing particle; these detectors are called drift chambers. For example, the NEWS-G experiment [27] uses spherical vessels filled with noble gases, built as proportional counters with a small sensor at the center of the vessel providing the

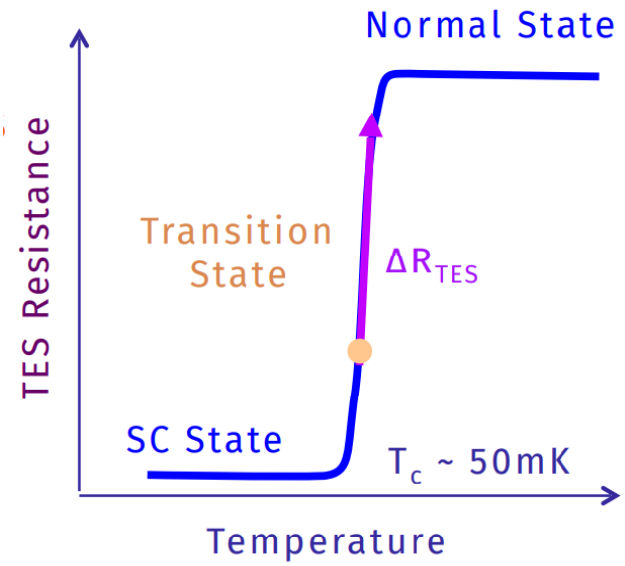

FIG. 3.5. Superconductor transition above T_C through heat absorption in SuperCDMS detectors. [26].

high voltage inside the chamber, in order to allow charge collection at the central electrode. Figure 3.6 shows one NEWS-G copper vessel, with a schematic view of the electric field in the chamber. When a particle interacts in the detector, electrons from primary ionization drift towards the sensor. Accelerated through the electric field, they then gain enough energy to create secondary ionizations, producing an avalanche process resulting in a few thousands electrons captured at the sensor. Meanwhile, all ions (from primary and secondary ionizations) drift the other way, to the grounded vessel, inducing the greater part of the current (signal). The more energetic the incoming particle, the more primary and secondary ionizations, and the more current at the end.

Drift chambers can also be built as multi-wire proportional chambers (MWPC), where multiple wires are combined in a grid, each acting as an independent proportional counter, to reconstruct the 2D position of the ionization event. Figure 3.7 illustrates the design of such detectors, and its 2D reconstruction.

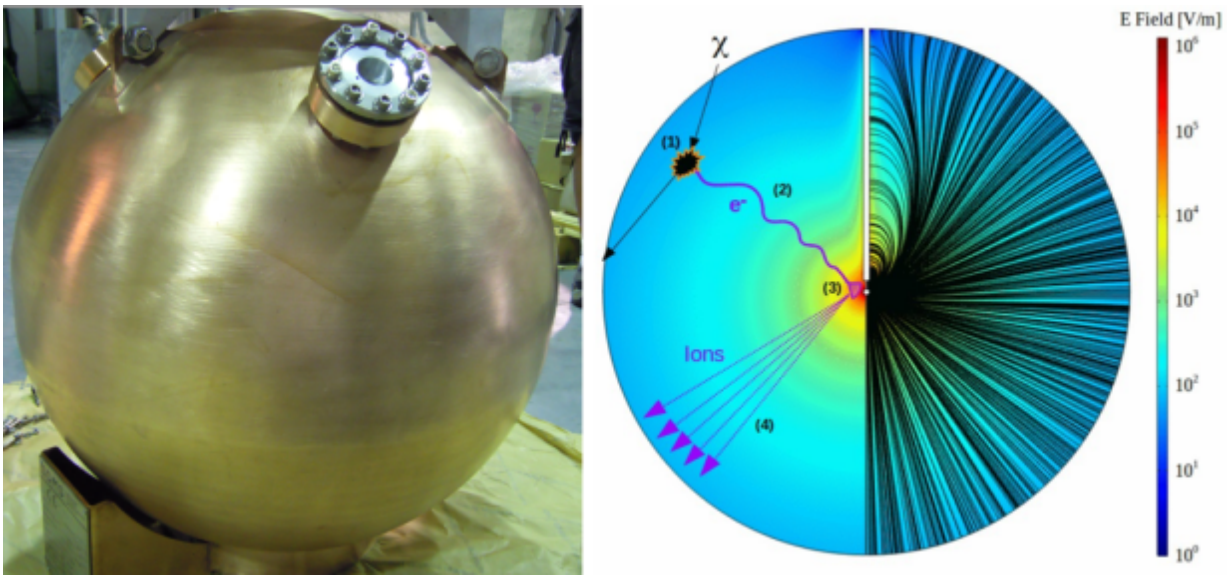

FIG. 3.6. One 60-cm NEWS-G copper vessel (left) and the electric field inside a chamber (right). Field lines are shown on the right part of the picture, and intensities on the left part (corresponding to the log scale on the right) [27].

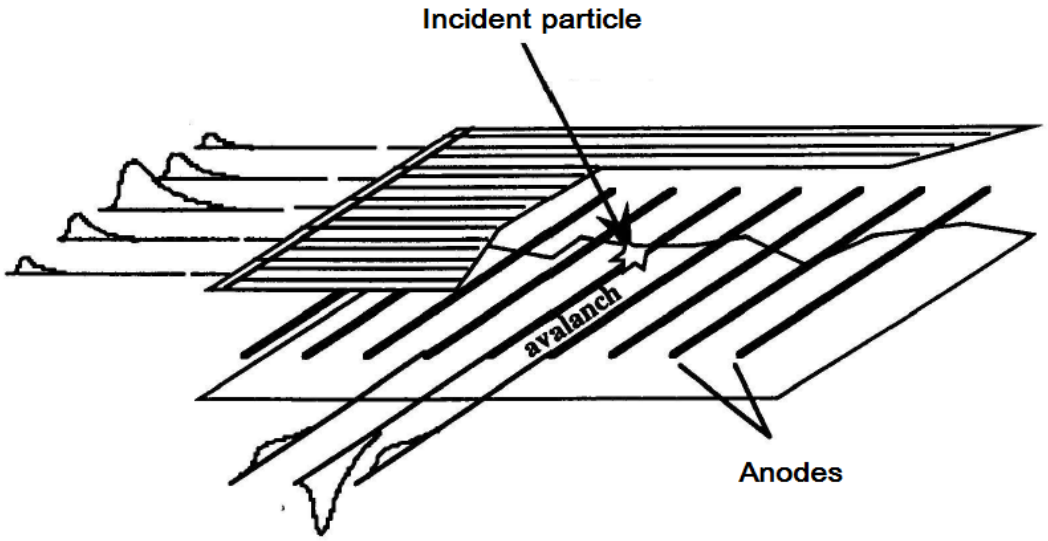

FIG. 3.7. Multi-wire proportional chamber.

Some experiments combine the ionization and scintillation techniques, notably XENON [28], LUX [29], DarkSide [30] and PandaX [31]. These two techniques are put together in a type of detector called time projection chambers (TPC): electrons and ions are collected under the same principle as MWPCs, giving a 2D reconstruction of the event, while photons are collected independently - usually in photomultiplier tubes (PMT); difference in time

FIG. 3.8. The XENON100 detector, filled with 105 kg of LXe [28].

between the collection of photons (almost instantly) and electrons (μs or a few ms) allows to reconstruct the depth of the event, and thus its 3D position. For example, the XENON Experiment uses liquid xenon (LXe) as the active target in its TPC, enclosed between an anode on top and a cathode at the bottom, each paired up with a set of PMTs to collect scintillation light. Figure 3.8 shows the XENON100 detector.

Finally, experiments such as DAMA [32], DEAP [33] and MiniCLEAN [34], use only the scintillation technique as their dark matter detection principle. For example, the DEAP Experiment uses liquid argon (LAr) as its active target; events in the detector will come from excitation of the LAr, itself coming from either a nuclear recoil of argon itself, atomic excitation of argon from electromagnetic events, alpha particles, or the recoil of heavy nuclei. Excited argon will produce UV light as it de-excites, with a wavelength of 128 nm. A wavelength shifter - more precisely tetraphenyl butadiene (TPB, $C_{28}H_{22}$) - is then used to shift the UV light to the visible spectrum, that can then be collected in PMTs. Waveforms

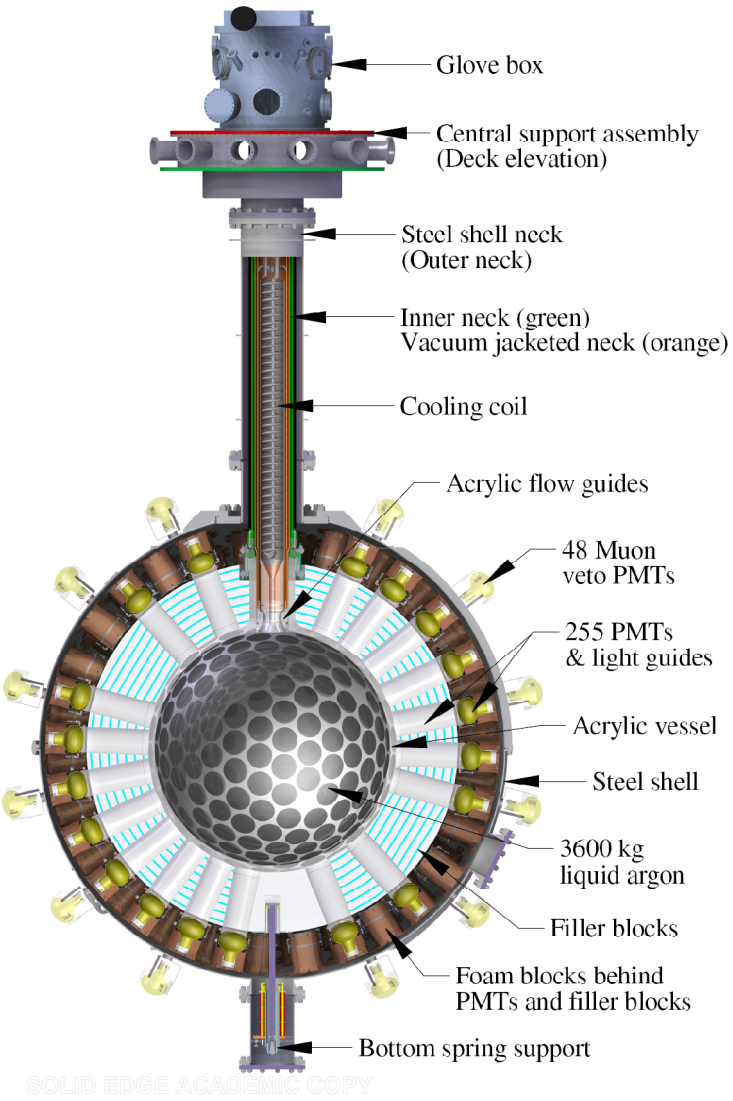

FIG. 3.9. The DEAP-3600 detector, filled with 3600 kg of LAr [33].

of signals in the PMTs are then analyzed to allow particle discrimination and eventually, dark matter detection. Figure 3.9 presents the DEAP-3600 dark matter search detector.

3.2. INDIRECT DETECTION

Dark matter indirect detection experiments will search in outer space for excess signal created in certain final states of dark matter decaying or annihilating with itself. Looking in the sky at regions where dark matter is present in high density, such as the galactic center,

dwarf galaxies or galaxy clusters, dark matter can provide signals by decaying into Standard Model (SM) particles, or by annihilating into them. The flux of particles coming from dark matter decaying or annihilating can be factored into two parts, one that depends on the dark matter theoretical model used, and one that depends on the dark matter distribution. The latter, referred as the "J-factor", is defined as [35]:

$$J_{dec}(\psi) = \int_{los} \rho(\psi,l)dl \tag{3.2.1}$$

for decay, and

$$J_{ann}(\psi) = \int_{los} \rho^2(\psi,l)dl \tag{3.2.2}$$

for annihilation, where ψ is a sky direction, l is a distance along the line-of-sight (los) and ρ is the dark matter density. The differential intensity of particles observed (per area A, time t, solid angle Ω and energy E), from the direction ψ, is then:

$$\frac{dN_{dec}}{dA\ dt\ d\Omega\ dE} = \frac{1}{4\pi}\frac{1}{m_\chi \tau}\frac{dN_x}{dE}J_{dec}(\psi) \tag{3.2.3}$$

for decay, and

$$\frac{dN_{ann}}{dA\ dt\ d\Omega\ dE} = \frac{1}{4\pi}\frac{\langle\sigma v\rangle}{2m_\chi^2}\frac{dN_x}{dE}J_{ann}(\psi) \tag{3.2.4}$$

for annihilation, where τ is the lifetime of the dark matter particle (for the decay case) and dN_x/dE is the differential spectrum of x-particles emitted, per annihilation or decay.

The total spectrum of x-particles can simply be written as the sum of all its final states f spectra, with the corresponding branching ratios B_f:

$$\frac{dN_x}{dE} = \sum_f B_f \frac{dN_{x,f}}{dE} \tag{3.2.5}$$

The final states will be stable SM particles that are kinematically accessible from the dark matter initial state. They therefore include photons, neutrinos, electron-positron pairs,

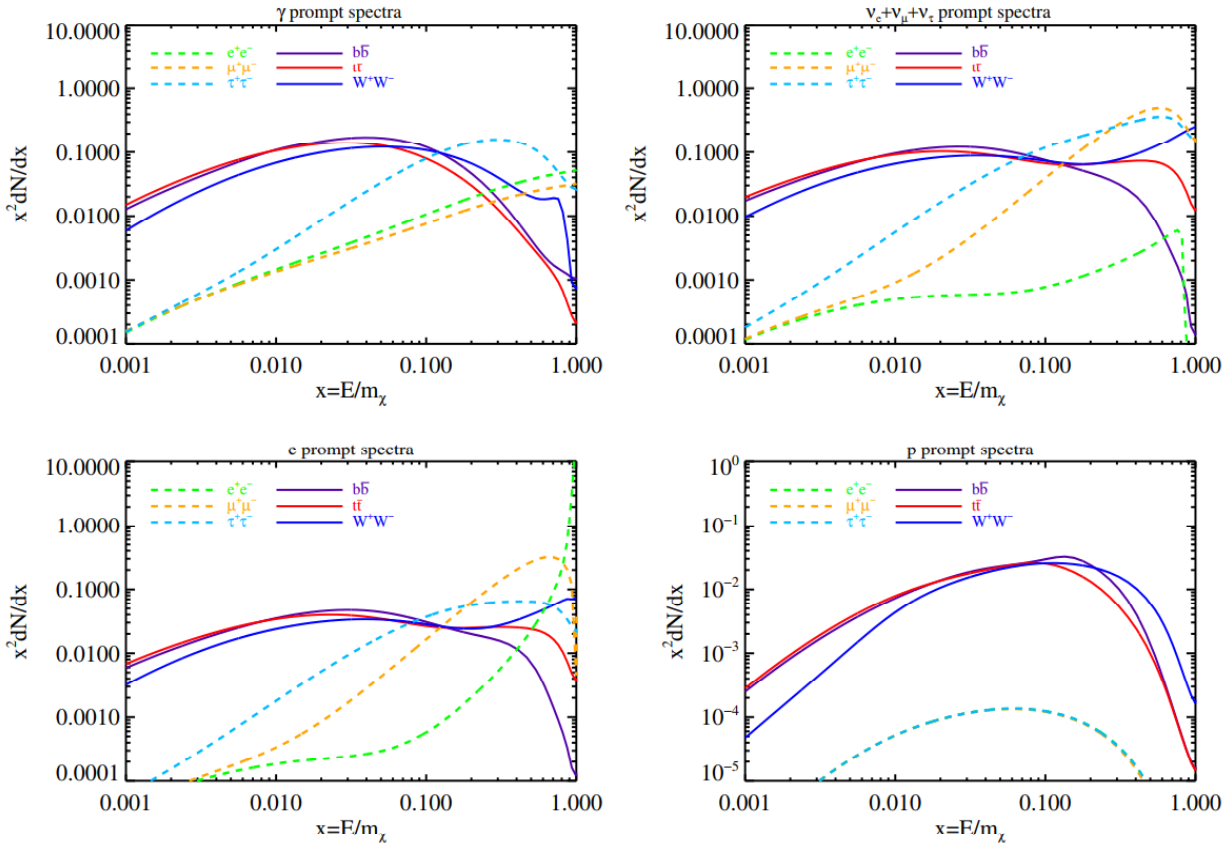

FIG. 3.10. Spectra from dark matter particles annihilation, for final state photons (top left), sum of all neutrino flavors (top right), electrons (bottom left) and protons (bottom right), for $m_\chi = 500$ GeV [35].

proton-anti-proton pairs, and heavier nuclei. The spectra for photons, neutrinos, electrons and protons, from dark matter annihilation, are shown on figure 3.10. Dark matter will be attempted to be detected by finding hints of these spectra through other background radiation from outer space.

3.2.1. Indirect detection experiments

From the previous section and figure 3.10, indirect detection experiments can therefore be separated in three categories: gamma-ray telescopes, neutrino detectors and cosmic-ray detectors.

The first category includes experiments/apparatuses such as the Fermi Gamma-ray

FIG. 3.11. Picture of the VERITAS telescope array [38].

Space Telescope (or The Fermi Large Area Telescope, LAT) [36], H.E.S.S [37] and VERITAS [38]. Gamma rays are good candidates for potential indirect detection of dark matter: first because the WIMP mass scale provides a large part of its decays and annihilation in the gamma-ray energy range; second because they are excellent for mapping the source of the signal - since they travel to the observer without deflection - and for carrying spectral information that can be very useful for the characterization of the dark matter particle when (if) detected. However, the Earth's atmosphere completely blocks (absorbs) cosmic gamma rays, so one has two options: detect them directly from space (e.g. LAT), or detect them indirectly from Cherenkov radiation in the Earth's atmosphere, at the Earth's surface (e.g. H.E.S.S, VERITAS). Figure 3.11 shows VERITAS telescopes.

Neutrino detectors include experiments such as IceCube [39], ANTARES [40] and Super-Kamiokande [41]. They require a large volume of water or ice to observe Cherenkov radiation coming from particles interacting with cosmic neutrinos. Like gamme rays, neutrinos are useful to trace back the source and energy of the signal, as neutrinos hardly interact at all with matter. Figure 3.12 shows the IceCube cubic kilometre detector, anchored at the South Pole, within Antarctica's ice. IceCube consists of 5 160 digital optical modules (DOM), each with a ten-inch photomultiplier tube, detecting light from charged leptons doing Cherenkov radiation after interactions with neutrinos in Antarctica's ice. The DOMs are arranged in 86 vertical layers inside holes melted into the ice, and arrayed over a

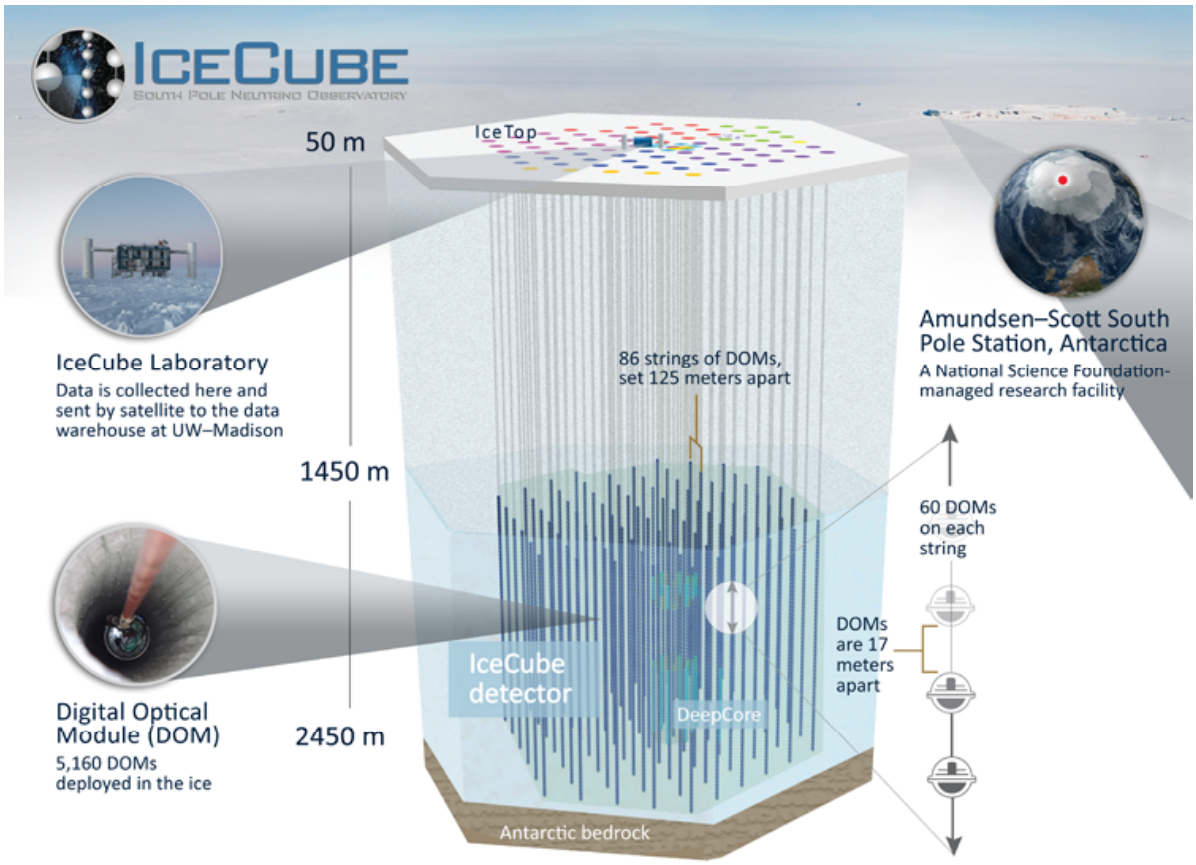

FIG. 3.12. Ice Cube neutrino detector [39].

cubic kilometre ranging from 1 450 meters to 2 450 meters in depth.

Finally, cosmic-ray detectors search for products of dark matter decay and annihilation in local charged cosmic ray fluxes and include experiments such as PAMELA [42] and AMS-02 [43], but also ground-based Cherenkov detectors (H.E.S.S, VERITAS, etc). They are advantageous for being highly sensitive due to low backgrounds produced by standard astrophysical processes, but lack the ability of mapping the source of the signal because of diffusion and deflection of the charged cosmic rays.

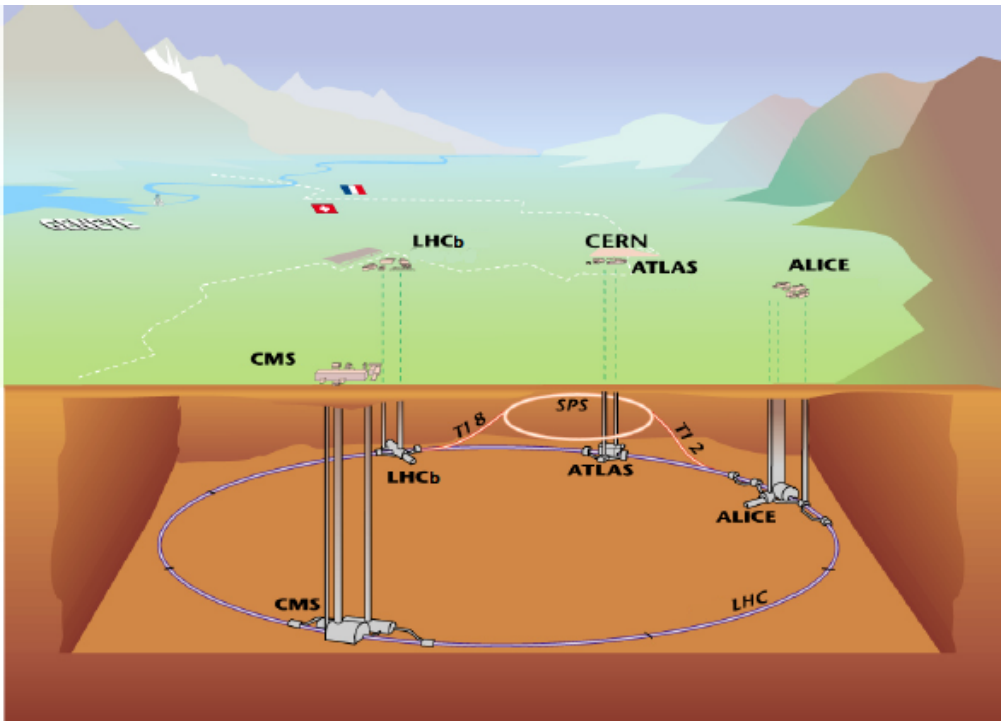

FIG. 3.13. CERN's LHC and experiments.

3.3. PRODUCTION

The third and last way to potentially detect dark matter is by producing it in high-energy laboratories, such as particle colliders. Particle colliders have been the bread and butter of new particle discoveries in the last decades, from the burst of discoveries in the 1960-70's to the highly awaited observation of the Higgs boson in 2012. Currently, the most powerful particle collider in the world is the Large Hadron Collider (LHC), located at CERN, on the border between Switzerland and France [44]. As of 2018, it collides protons at 13 TeV of energy in the center of mass. It was home of the Higgs boson discovery in 2012, and still runs for the search of new physics. Figure 3.13 shows the CERN accelerator complex and the four experiments around its 27-km accelerator ring 175 m underground, namely ATLAS [45], CMS [46], ALICE [47] and LHCb [48].

Particle collider experiments have different types of particle detectors to identify and reconstruct the products of the collisions. Taking the ATLAS detector as an example, from inside to outside (figure 3.14): charged particle trackers measure, by ionization, the

trajectory of charged particles coming from the collisions; electromagnetic calorimeters measure the energy of electromagnetic particles such as electrons, positrons and photons, through Bremsstrahlung radiation; hadronic calorimeters measure the energy of hadrons by stopping them in high-density materials, through nuclear interactions; finally, muon spectrometers measure muons momenta after they passed through all previous detectors without interacting much. The difficulty with collider experiments to successfully detect dark matter is that dark matter will not interact with any of the detectors that reconstruct the events. The presence of a WIMP in a collison event will therefore have to be inferred, through what is referred to as the missing transverse momentum; since the collision initially has zero momentum in the plane transverse to both colliding beams, it needs to also have zero momentum in this plane in the final state. Once the whole event has been reconstructed and all particles identified, the sum of all transverse momenta should be zero; if not, this means that some particle(s) didn't interact in any of the detectors, carrying the missing momentum that was not measured. Neutrinos are the most common particles responsible for missing transverse momentum, making it difficult to definitely attribute it to a WIMP, and therefore to be able to detect it.

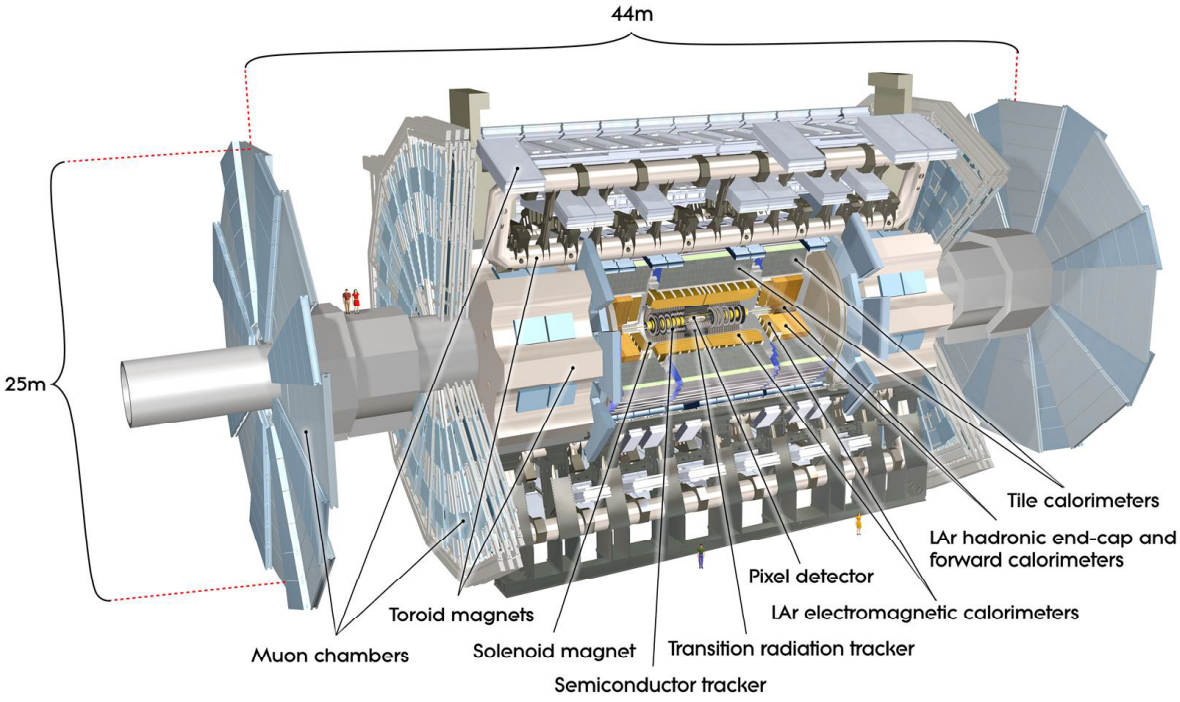

FIG. 3.14. The ATLAS detector at LHC [45].

Chapter 4

THE PICO EXPERIMENT

This chapter describes the PICO experiment for the direct detection of dark matter. PICO is a bubble chamber experiment (§4.1) that uses superheated liquids (§4.1.1) to try to detect interactions between dark matter and ordinary matter. The PICO Collaboration was formed in 2013 by the union of the PICASSO [49] and COUPP [50] collaborations. Its latest results are presented in section 4.5.

4.1. Bubble chambers

Bubble chambers are particle detectors that were invented in 1952 by Donald Glaser [51], and which had their success in the 1970's, leading to discoveries such as the charged and neutral currents. They use superheated liquids to detect energy depositions from incoming particles; their principle is explained in the next sections.

4.1.1. Superheated liquids

Superheat is a metastable state where a fluid is maintained in its liquid state while being above its boiling point. This state is obtained, for example, by reducing the pressure of a liquid below its vapour pressure, while keeping its temperature constant. At a fluid's vapour pressure (i.e. on the saturation curve delimiting the liquid and vapour states on a phase diagram), the liquid and gaseous phases coexist in equilibrium (see phase diagram

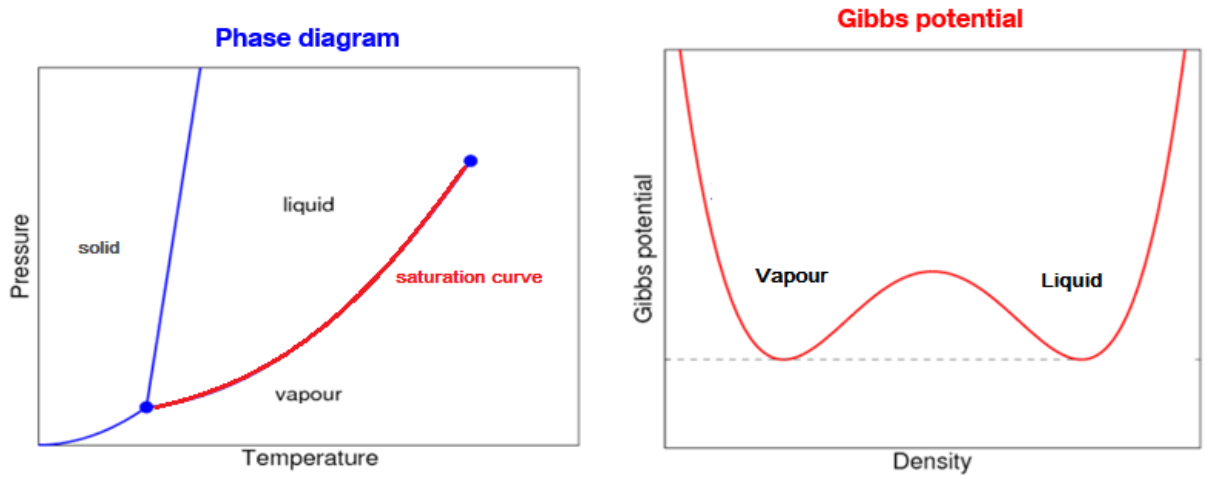

FIG. 4.1. Typical phase diagram, with the liquid-vapour saturation curve highlighted (left) and the Gibbs potential on the saturation curve (right).

and Gibbs potential on figure 4.1), as they occupy equal minima in the Gibbs potential. Reducing the pressure at a constant temperature (or increasing the temperature at a constant pressure) then leads to a superheated state, as shown on figure 4.2. The minimum of the superheated liquid Gibbs potential is local, and above the vapour minimum; this leads to a metastable state, where an amount ΔE of energy given to the system will lead to a phase transition from liquid to vapour. Bubble chambers are based on this principle, i.e. that energy depositions in superheated liquids will create phase transitions; their detection and functioning principles are detailed in the next section.

4.1.2. Detection principle

Bubble chambers are filled with fluids that become their active mass when put into a superheated state. As explained in the previous section, the superheated fluid then becomes sensitive to potential phase transitions, when energy is deposited into it. That way, an incoming particle passing through the superheated liquid deposits energy by scattering off the fluid's atoms (nuclei or electrons) and creates a phase transition - a gas bubble is formed.

To be operational, bubble chambers use a piston (or similar device) that regulates

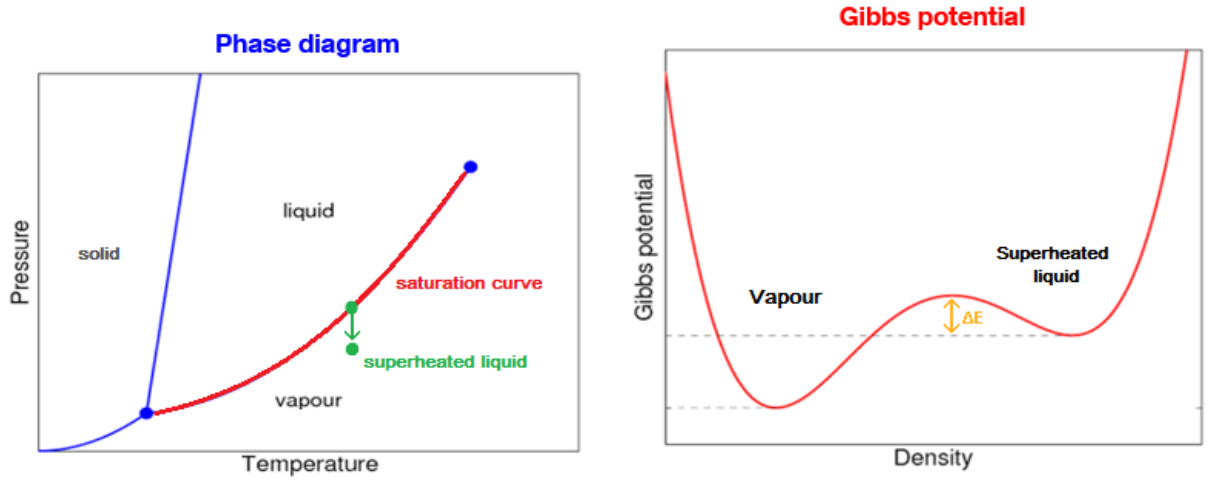

FIG. 4.2. Superheat phase diagram (left) and Gibbs potential of a superheated state (right).

the pressure of the active fluid. Because superheat is easier (and faster) achieved by controlling the pressure instead of the temperature, temperature is held constant in the detector, while the pressure is externally controlled. By default, the chamber when inactive is compressed, under high pressure, keeping the active fluid in the stable liquid state. To get the chamber active, the pressure is then lowered until the liquid is in a superheated state, and stays as is until an event occurs and energy is deposited in it. When a phase transition happens and a bubble is formed, the chamber is quickly recompressed, crushing the gas bubble back to liquid, and the chamber is inactive again and ready for the next expansion cycle. To detect the bubble formations, cameras monitor the inside of the detector and are set to trigger the recompression as soon as a bubble is seen. Some bubble chambers are also submerged in a constant magnetic field, curving tracks of charged particles. A simple drawing in figure 4.3 shows all of this together.

Two types of events can occur in a bubble chamber: ionization tracks and nuclear recoils. The former happens when a charged particle goes through the detector and, on its way, strips electrons from the active fluid's atoms; these δ-electrons then create bubbles, forming a track of bubbles on the incoming particle's path. An example is shown on figure 4.4. The latter occurs when a neutral particle passes through the chamber and does elastic

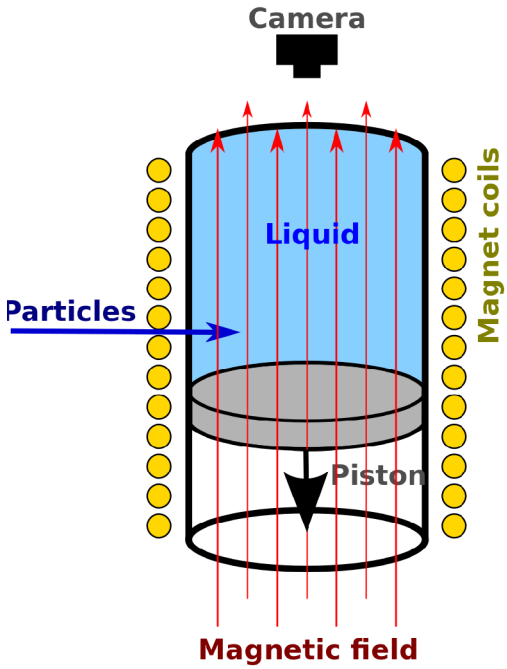

FIG. 4.3. Schematic representation of a bubble chamber [52].

scattering with one or many of the active fluid's nuclei; each recoil nucleus then creates a bubble, leading to events with one or many randomly spaced bubbles, as the incoming particle can scatter in any direction and can create an multitude of bubbles, anywhere in the detector. An example is shown on figure 4.5.

4.2. PICO DETECTORS

PICO is an experiment that uses bubble chambers to search for dark matter; this section presents the PICO dark matter detectors.

4.2.1. Characteristics

PICO detectors are all built in a similar way and share many characteristics, which are listed below.

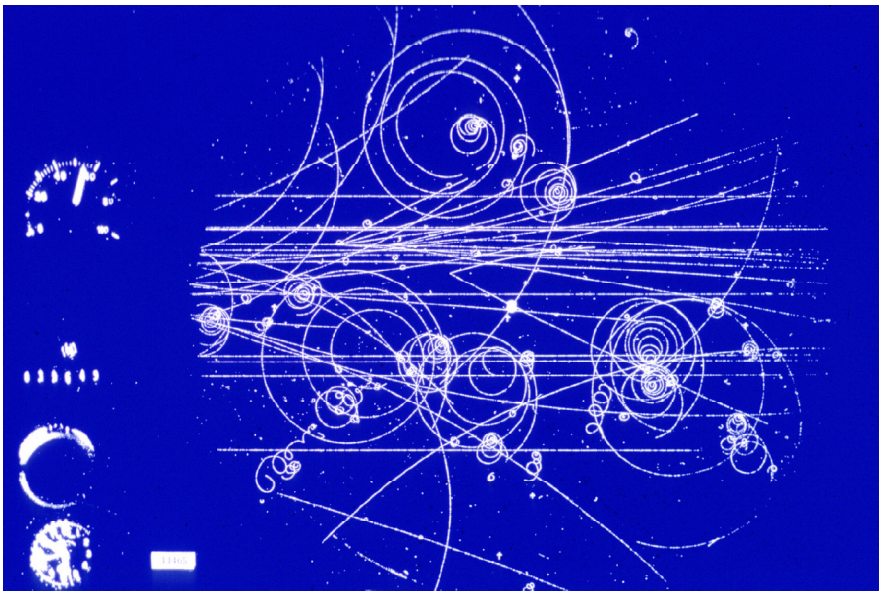

FIG. 4.4. Ionization tracks in CERN's first liquid hydrogen bubble chamber in 1960 [53].

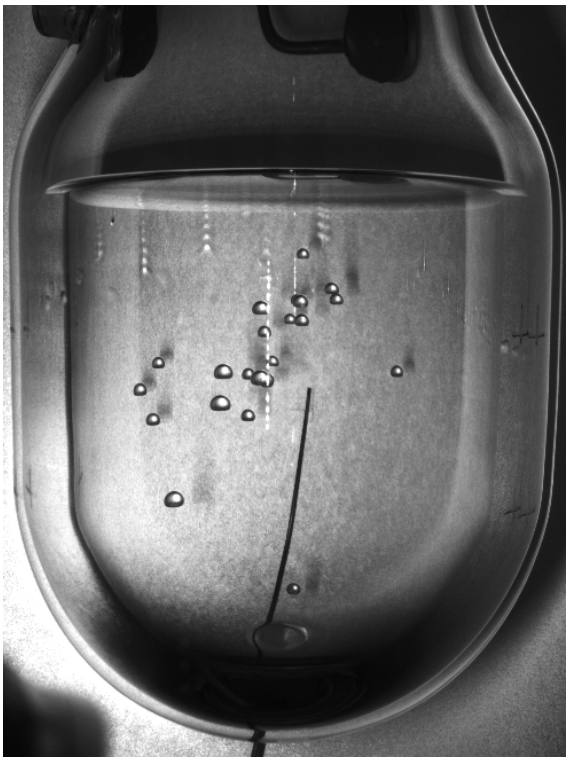

FIG. 4.5. Photo of a multi-bubble event from neutron scattering in the PICO-2L bubble chamber [21].

(i) Their active fluids are contained in ultra-clean quartz or silica vessels. Since we want to reach very high sensitivity levels for the search of dark matter, the inner

vessels containing the superheated liquids need to be particulate-clean and very low in radioactive contamination, keeping background as low as possible. Likewise, since rough surfaces are potential nucleation sites for bubbles in superheated liquids, the walls of PICO bubble chambers have to be very smooth. For these reasons, fused quartz or silica vessels are used for PICO detectors.

(ii) All PICO detectors acquire live data and are controlled through a Data AQuisition system (DAQ) connected to them. It allows to regulate the pressure inside the detector and to record acoustic signals, and provides informations on the current state of the chamber : temperature, pressures inside and outside, live pictures of the detector, etc.

(iii) The pressure inside PICO bubble chambers is regulated by hydraulic systems connected to bellows on top of the chambers; to keep the interior of the detector compressed or expanded, bellows contract or stretch, respectively. Pressure can be set precisely to obtain the desired level of superheat, and then recompression reverts to the inactive state. A picture of the bellows mounted on top of an inner vessel is shown on figure 4.6. Larger PICO detectors are immersed inside a pressure vessel so that the pressure inside and outside of the chamber are equal; smaller test chambers don't have pressure vessels and require thick, high pressure rated inner vessels. Usually, ordinary mineral oil is used in the hydraulic system.

(iv) In order to see bubble events in PICO chambers, a set of cameras monitor the detectors at all times. As soon as a bubble is detected, a signal is sent to the DAQ to recompress the chamber and end the superheat state. The cameras are also used to count the number of bubbles for each event.

(v) Every PICO detector is equipped with a set of piezoelectric transducers that record the sound which accompanies bubble formation in the chamber. They are mounted directly on the glass jar to minimize the acoustic loss through propagation. Acoustic signals of each event are recorded and used to classify different types of events.

(vi) Most PICO detectors have a non-reactive buffer fluid on top of the active liquid, so that the latter lays only inside the inner vessel, and that there are no events occurring in other parts of the detector (inside the bellows, etc.). PICO usually uses water or linear alkylbenzene (LAB) as buffer fluids.

(vii) PICO detectors typically use "Freons" - halocarbons, chlorofluorocarbons, hydrofluorocarbons, etc, i.e. compounds containing primarily carbon and fluorine - as their active fluid. As explained in section 3.1, fluorine is a target of choice for SD-sensitive dark matter search experiments. C_3F_8 is the most common target for PICO chambers, although other compounds have also been used such as C_2ClF_5 (see chapter 5) and $C_2H_2F_4$ (see chapter 6).

4.2.2. Detectors

The PICO experiment uses a series of bubble chambers of various size, for calibration purposes and for dark matter search. Here are the main ones.

4.2.2.1. *PICO-2L*

PICO-2L was the first chamber of the newly formed PICO Collaboration in 2013. It is a two litre bubble chamber for the search of dark matter, located at SNOLAB. It has been decommissioned in early 2017 after two runs of dark matter search with respectively 2.90 $\pm$ 0.01 and 2.91 $\pm$ 0.01 kg of C_3F_8 as the active fluid [**54, 55**]. The design of PICO-2L is shown on figure 4.7; two cameras look inside the pressure vessel, and three piezos are

FIG. 4.6. PICO-2L inner vessel and bellows [21].

mounted on the fused silica jar. Water is used as the buffer fluid.

4.2.2.2. *PICO-60*

PICO-60 is the latest primary dark matter search detector for the PICO experiment, also located at SNOLAB. It is a 40 litre bubble chamber that has been decommissioned in 2017 after two runs of dark matter search with respectively 36.8 ± 0.2 kg of CF_3I and 52.2 ± 0.5 kg of C_3F_8 as active fluids [56, 57] (appendix A). PICO-60 is designed as shown on figure 4.8; four cameras look inside the pressure vessel, and nine piezos are mounted on the fused silica jar. Water is used as the buffer fluid.

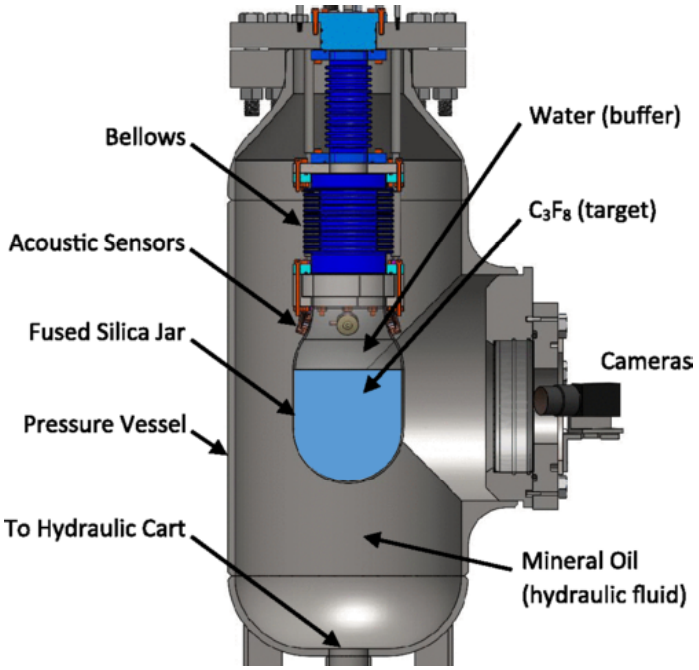

FIG. 4.7. A schematic view of the PICO-2L detector [54].

4.2.2.3. *PICO-40L*

PICO-40L is the next primary dark matter search detector of the PICO Collaboration that is expected to be running in early 2019, in the same location as PICO-60 in SNOLAB. It will use the same 40 litres vessel than PICO-60, but its design is different: the chamber will be upside down! The new design will allow to remove the buffer fluid from the chamber: as shown on figure 4.9, the top part of the detector (containing the active fluid) is kept warm, while the bottom part (hydraulic system) is kept cold so that the target liquid in that region is not superheated. By using an inner jar as a piston inside another outer jar, no buffer liquid is needed; this way, it is removing a main fraction of the background events in the detector.

PICO-40L will be used to test the new "right-side up" design for future PICO detectors, especially PICO-500 (§4.2.2.4). If the experiment is conclusive and indeed background-reduced (compared to the last PICO-60 dark matter search run), the design shall be retained.

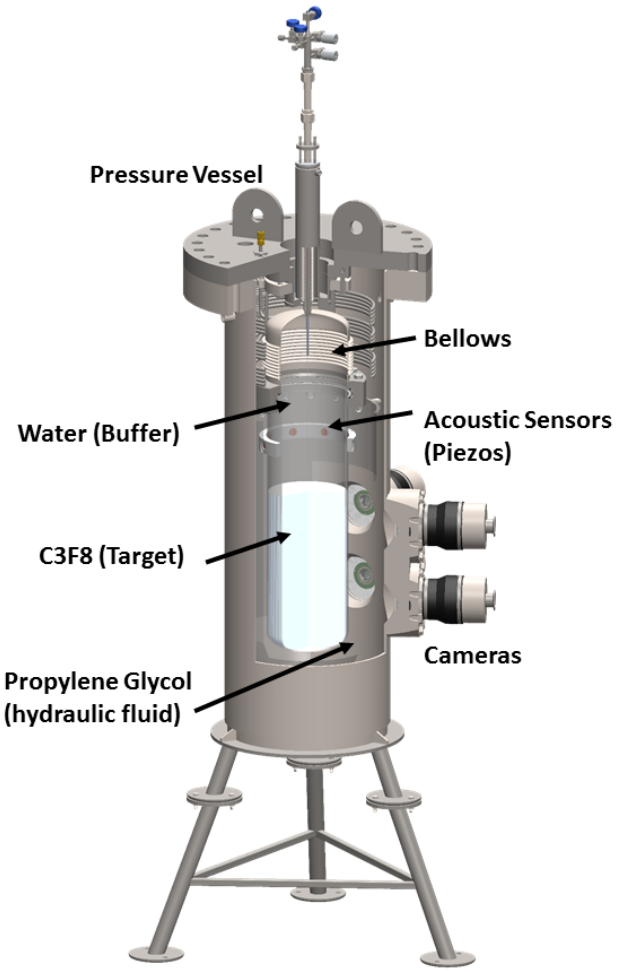

FIG. 4.8. A schematic view of the PICO-60 detector.

4.2.2.4. *PICO-500*

PICO-500 is the next generation PICO dark matter search detector; it is a 500 litres bubble chamber. It is currently under design (with the "right-side up" version by default) and its construction is planned to begin in 2019. Figure 4.10 shows a drawing of it using a pressure vessel inside a water tank, which currently belongs to the MiniCLEAN experiment at SNOLAB.

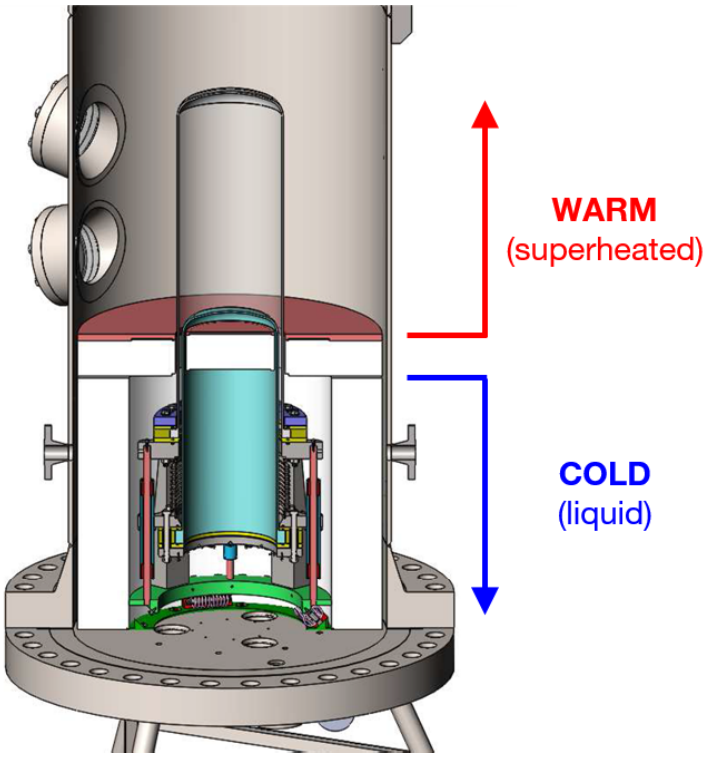

FIG. 4.9. Design of the PICO-40L detector [58].

4.2.2.5. *PICO-0.1*

PICO-0.1 is not a dark matter search detector, but a calibration chamber. It is a 75ml bubble chamber that is used to make threshold calibrations, to study different active fluids and to make any kind of tests, pertaining to the performance of this kind of detector. Its small size facilitates its operation in neutron test beams and active liquids are rapidly interchangeable, as the chamber is easier commissioned and decommissioned. It is also easy to make radioactive source calibrations, as its small size makes it less sensitive to ambient background and more sensitive to radioactive sources put right beside and directed towards it. Some pictures of it are shown on figure 4.11.

PICO-0.1 does not have a pressure vessel; instead, its jar is a centimetre-thick high pressure rated quartz glass. Two piezos are mounted on the jar to record acoustic signals, and two 150 frames per second cameras are monitoring it, located 90° from each other. Two LED panels alternatively light the chamber, each in synchronization with one camera.

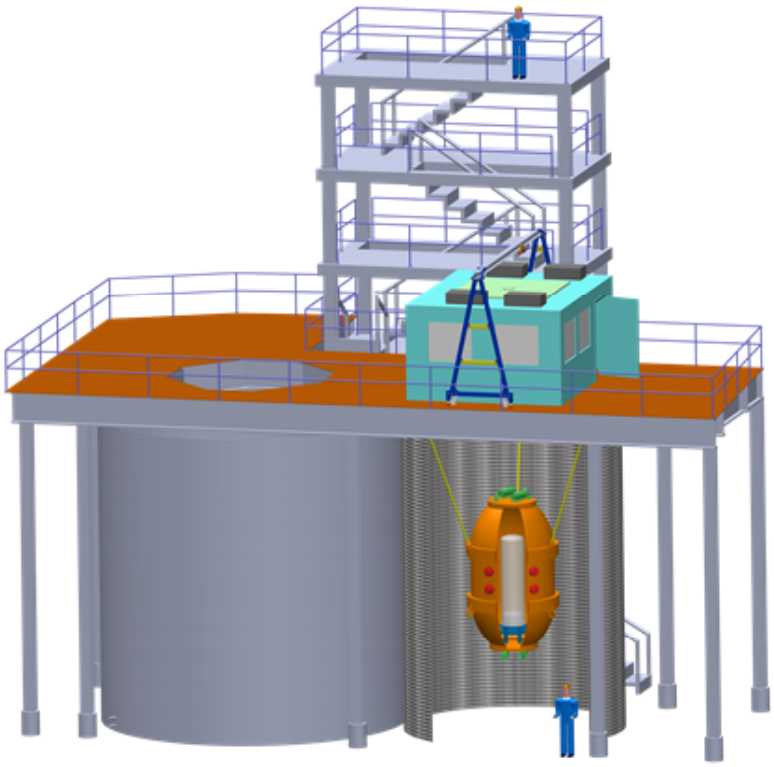

FIG. 4.10. PICO-500 in its pressure vessel, inside a water tank.

PICO-0.1 is immersed in a water bath to regulate its temperature; the water bath has a beam tube leading to the chamber to allow the insertion of radioactive sources close to the chamber. The complete setup is shown on figure 4.12.

The PICO-0.1 chamber was transferred from Fermilab to the University of Montreal accelerator laboratory and the calibration program carried out with this chamber is the main topic of this thesis; chapters 5 and 6 describe measurements (and analysis) made with this chamber.

4.3. SEITZ MODEL

In 1957, Frederick Seitz wrote *On the Theory of the Bubble Chamber*, in which he studied and described the theory behind bubble nucleation in bubble chambers [**59**]. His model,

FIG. 4.11. PICO-0.1. On the left, the chamber alone with its "top hat" containing the bellows. On the right, the chamber and its hydraulic cart.

nowadays called the "Seitz Model", shown to be adequate and is still used to explain and predict bubble formations in bubble chambers. This section summarizes this model and its main parameters.

4.3.1. The heat spike model

The Seitz Model states that the bubble formation mechanism in bubble chambers is primarily due to the production of highly localized hot regions, or "temperature spikes" in the superheated liquid. These "heat spikes" will generate local phase transitions, leading to the formation of bubbles larger than the critical size needed for them not to collapse under their surface tension.

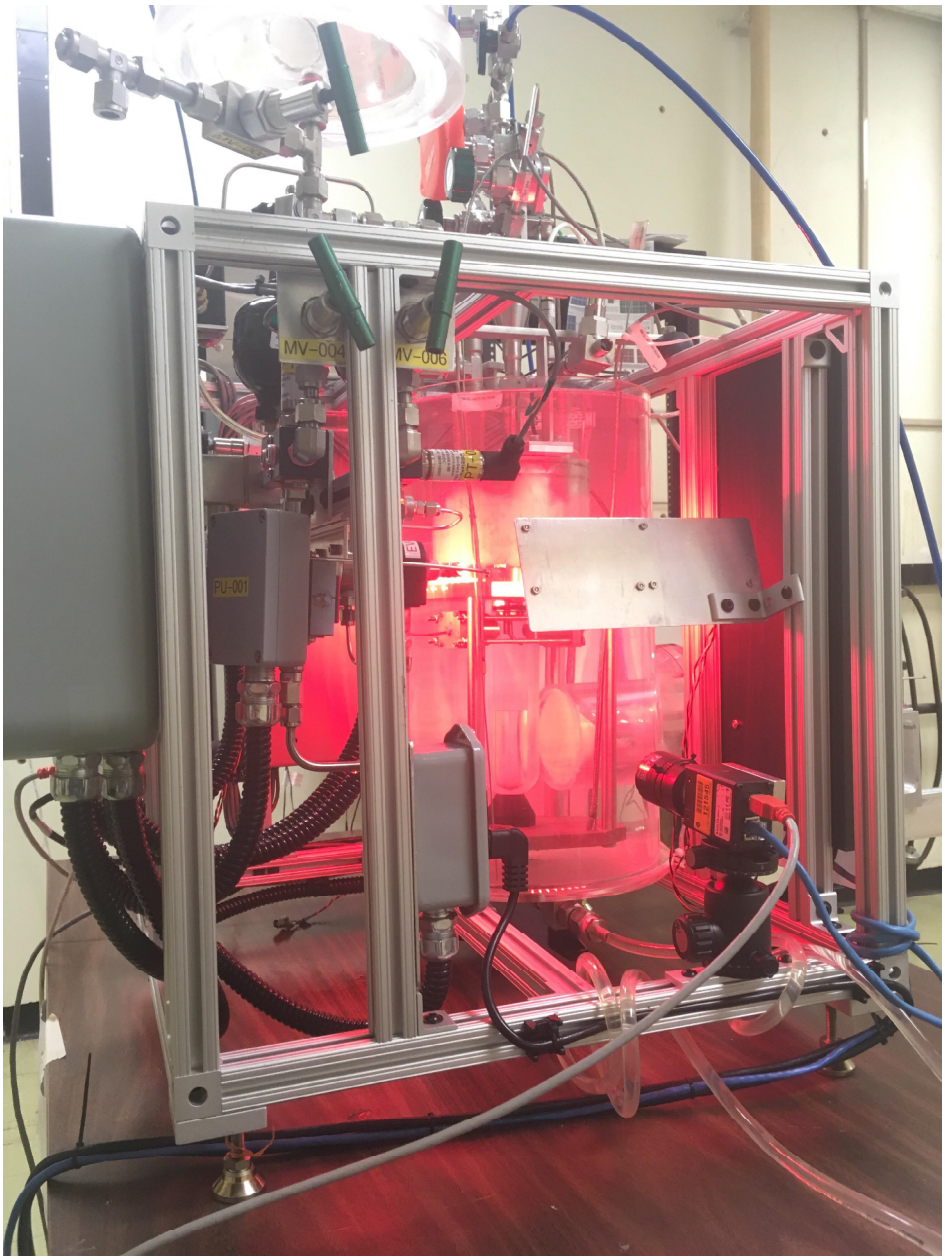

FIG. 4.12. PICO-0.1 complete setup.

The effective pressure experienced by a spherical bubble due to its surface tension is simply given by

$$p_e = \frac{2\sigma}{r} \tag{4.3.1}$$

where σ is the surface tension and r the radius of the bubble. At equilibrium, this pressure corresponds to the gas pressure inside the bubble, minus the fluid pressure outside of it :

$$p_e = p_b - p_f \ . \tag{4.3.2}$$

where p_b and p_f are the pressure of the bubble and the fluid, respectively. The pressure in the gas bubble can be expressed as:

$$p_b \approx p_v - (p_v - p_f)\frac{\rho_v}{\rho_f} \tag{4.3.3}$$

where p_v is the saturated vapor pressure, ρ_v the saturated vapor density and ρ_f the fluid density. Considering $\frac{\rho_v}{\rho_f} \ll 1$, we then get $(p_v - p_f)\frac{\rho_v}{\rho_f} \ll p_v$. We can therefore write

$$p_b \approx p_v \ . \tag{4.3.4}$$

The gas pressure of the bubble is in good approximation the saturated vapor pressure of the fluid; we will henceforth use this equality. From 4.3.1, 4.3.2 and 4.3.4, a bubble will then satisfy the condition

$$R_c = \frac{2\sigma}{p_e} = \frac{2\sigma}{p_v - p_f} \tag{4.3.5}$$

where R_c is the critical radius, i.e. the radius necessary to form a non-collapsing bubble. This means that a bubble acquiring a radius $r \geq R_c$ will continue to steadily grow, evaporating surrounding fluid with $p_f < p_v$ (since the fluid is in a superheat state), while a bubble with $r < R_c$ will only collapse on itself.

The energy required to form a bubble comes from four components [**60**] : the work done by expanding a bubble to its critical size - with radius R_c - against the pressure of the surrounding fluid, the energy required to evaporate the liquid, the work needed to form the

bubble surface (liquid-vapor interface), and the work lost into irreversible processes, such as acoustic emission, etc. The first term can then be written as:

$$W_c = -\frac{4\pi}{3} R_c^3 (p_v - p_f) \tag{4.3.6}$$

The vaporization term can be written as a function of the entropy change ΔS between the initial and final state:

$$W_v = T\Delta S \ . \tag{4.3.7}$$

In terms of the specific entropies s of the bubble and the fluid, we get:

$$W_v = \frac{4\pi}{3} R_c^3 \rho_v T (s_b - s_f) \ , \tag{4.3.8}$$

which can be expressed in terms of the latent heat of evaporation h_{lv}:

$$W_v = \frac{4\pi}{3} R_c^3 \rho_v h_{lv} \ . \tag{4.3.9}$$

The bubble surface term is a combination of the free energy of its surface, $4\pi R_c^3 \sigma$, and of its heat absorption from the surrounding fluid, $-4\pi R_c^3 T \frac{\partial \sigma}{\partial T}$:

$$W_s = \frac{4\pi}{3} R_c^3 \left(\sigma - T \frac{\partial \sigma}{\partial T} \right) \ . \tag{4.3.10}$$

Finally, the irreversible work is W_{irr} and is small compred to other terms; it can be neglected. Combining 4.3.6, 4.3.9 and 4.3.10, we obtain the total energy required to form a bubble :

$$\begin{aligned} E_c &= W_c + W_v + W_s + W_{irr} \\ &= -\frac{4\pi}{3} R_c^3 (p_v - p_f) + \frac{4\pi}{3} R_c^3 \rho_v h_{lv} + \frac{4\pi}{3} R_c^3 \left(\sigma - T \frac{\partial \sigma}{\partial T} \right) + W_{irr} \end{aligned} \tag{4.3.11}$$

where E_c stands for critical energy. A bubble is thus formed when an amount of energy $E \geq E_c$ is deposited in the superheated fluid, creating a bubble with radius $r \geq R_c$.

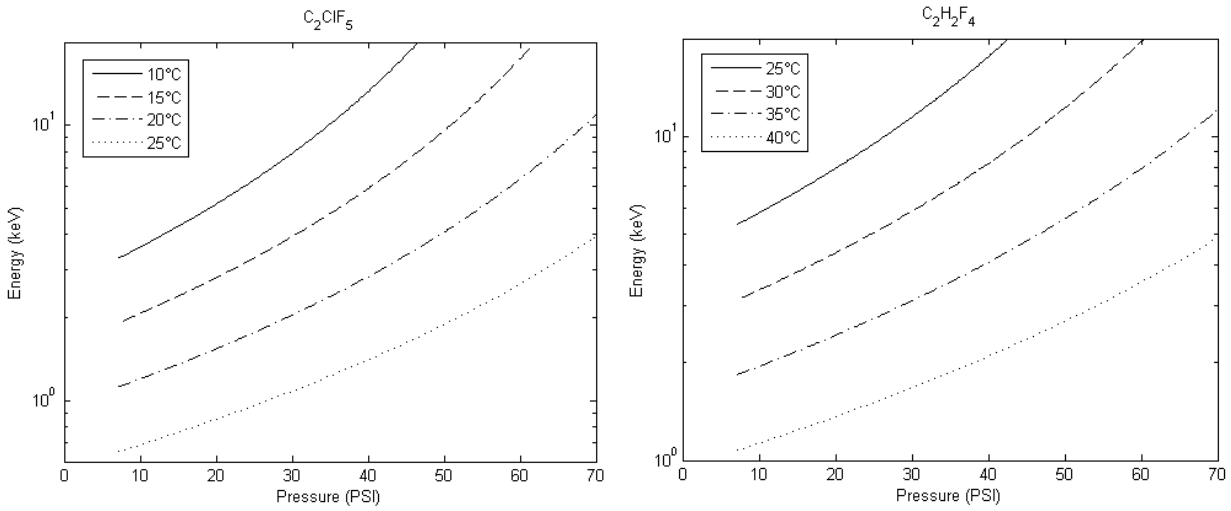

FIG. 4.13. Seitz critical energy curves for different temperatures, for C_2ClF_5 (left) and $C_2H_2F_4$ (right).

From thermodynamic properties of fluids obtained from the NIST database [61], one can calculate the Seitz critical energy for different pressure and temperature set points, as shown on figure 4.13 for C_2ClF_5 and $C_2H_2F_4$.

4.3.2. dE/dx threshold

In addition to the "heat spike" model where a bubble is created when the energy deposited in the superheated fluid E_{dep} satisfies $E_{\text{dep}} \geq E_c$, another criterion is necessary for the formation of the bubble, namely an effective enough stopping power dE/dx of the incoming particle. In order to successfully form a bubble, a particle has to deposit $E_{\text{dep}} \geq E_c$ inside a short distance, such that the heat input leads to a bubble of critical radius R_c. This distance is called the critical length L_c, and the criterion can be written as:

$$E_{\text{dep}} = \int_{L_c} \frac{dE}{dx} dx \geq E_c \tag{4.3.12}$$

L_c is typically expressed as a function of R_c, since it is the most useful scale in this context. We then have

$$L_c = b \cdot R_c \tag{4.3.13}$$

where b is named the Harper parameter, and varies from author to author. $b = 2$ is commonly used, but it also ranges up to 18, to quote for example [**62, 63**]. The Harper parameter shall be studied in the following chapter for the specific case of C_2ClF_5 as the active fluid for PICO-0.1, and more precisely in section 5.3.2.

4.4. Detector response

Given the criterion $E_{\text{dep}} \geq E_c$ to create a bubble in a superheated liquid, E_c can also be viewed as a threshold energy; any E_{dep} larger than E_c will create a bubble, making bubble chambers operating as threshold detectors.

Being threshold detectors, bubble chambers have their unique response to incoming particles; their event count rate at a given energy threshold will depend only on energy deposition above threshold. Given recoils with a specific energy spectrum, the detector response at a fixed threshold will be proportional to the integral of the spectrum above this threshold. A good example to illustrate this behaviour is elastic neutron scattering with the active fluid's nuclei: from kinematics, the recoil energy E_R of a nucleus of atomic mass A, from elastic scattering with an incoming neutron of energy E_n, is given by :

$$E_R = \frac{2A}{(A+1)^2}(1 - \cos\theta)E_n \tag{4.4.1}$$

where θ is the neutron scattering angle, in the centre of mass frame. Taking C_3F_8 as an example (PICO's usual target for dark matter search), the maximum recoil energies (with $\theta = \pi$) of carbon and fluorine nuclei are then:

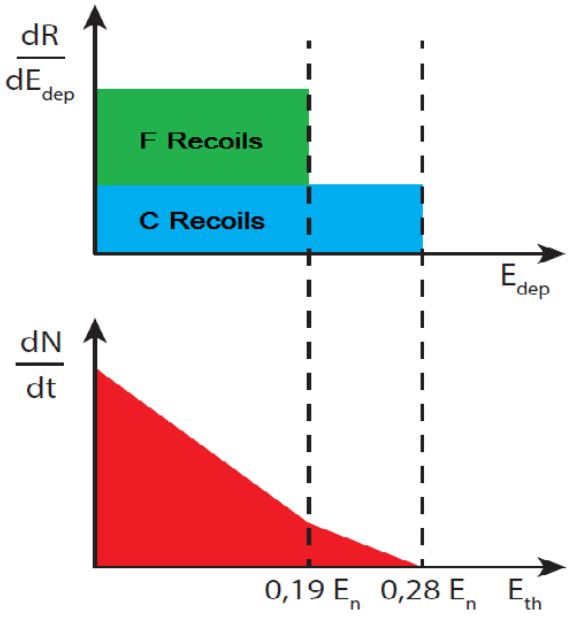

FIG. 4.14. Recoil energy spectra for carbon and fluorine, for elastic scattering with neutrons of energy E_n (top). Detector response (count rate $R = dN/dt$) in function of its threshold energy E_{th}, for the same type of event (bottom).

$$\begin{aligned} \text{C (A=12)} &: E_{R_{max}} \approx 0.28 E_n \\ \text{F (A=19)} &: E_{R_{max}} = 0.19 E_n \ . \end{aligned} \tag{4.4.2}$$

Assuming an isotropic neutron scattering, θ ranges randomly from 0 to 2π. The recoil spectra of the nuclei will then have a box shape, ranging from $E_R = 0$ to $E_R = E_{R_{max}}$, as shown on top of figure 4.14. The detector response will therefore look like the bottom of figure 4.14, as integrating the box-shaped spectrum above each energy threshold will result in a linear count rate curve, rising as we decrease the threshold energy.

4.5. CURRENT RESULTS

As dark matter has not been directly detected yet, experiments try to reach the best sensitivity in trying to do so. The PICO experiment currently holds the world-leading exclusion limits for the direct detection of spin-dependent WIMP-proton interaction, as a result of PICO-60 last dark matter search run [57] (appendix A), as shown on figure 4.15. Spin-independent WIMP-nucleon interaction limits are also shown on figure 4.16.

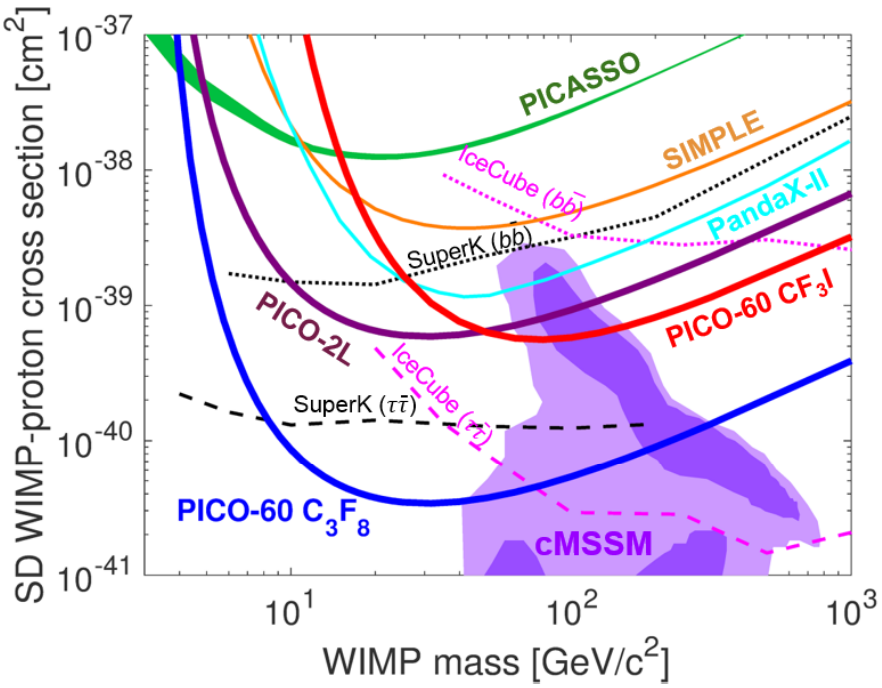

FIG. 4.15. Spin-dependent WIMP-proton cross-section limits set by different dark matter detection experiments. Thick lines are direct detection experiments, while dashed lines are indirect detection experiments.

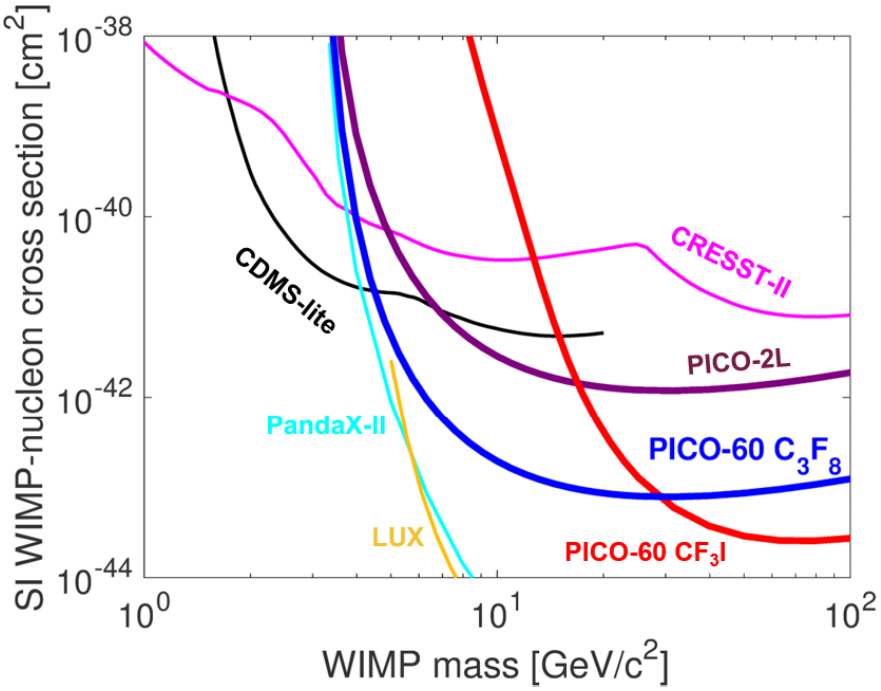

FIG. 4.16. Spin-independent WIMP-nucleon cross-section limits set by different dark matter detection experiments.

Chapter 5

SEITZ THRESHOLD CHARACTERIZATION WITH C_2ClF_5

C_2ClF_5 can be used in a PICO detector in order to precisely characterize the Seitz threshold, through the reaction between a thermal neutron (neutron with a kinetic energy of the order of its thermal energy, i.e. ∼0.025 eV) and a chlorine nucleus from the superheated fluid:

$$^{35}\mathrm{Cl}\ (n_{th}, p)\ ^{35}\mathrm{S} + 617\ \mathrm{keV}\ , \tag{5.0.1}$$

where n_{th} is the thermal neutron. Since the incoming neutron is almost at rest, and from conservation of momentum, this reaction produces recoils of a ^{35}S nucleus and of a proton in opposite directions; the former with 17 keV of kinetic energy, the latter with 600 keV [64]. Because the reaction products are monoenergetic, this reaction provides a precise scale for the Seitz threshold, since the recoil energies are perfectly known inside the detector. A study to characterize the Seitz threshold with this reaction is subject of the present chapter.

5.1. C_2ClF_5 THERMODYNAMICS

"Freons" such as C_3F_8, C_4F_{10} and even C_5F_{12} have been proven to be thermodynamically appropriate for bubble chamber experiments. PICO uses C_3F_8 as its active fluid for the search of dark matter, and C_2ClF_5 has really similar thermodynamic properties. Table 5.1

Property	C_3F_8	C_2ClF_5
T_B (°C)	-36.789	-38.942
T_C (°C)	71.95	79.79
$P_{v\ 15°C}$ (PSIA)	95.180	99.596
$\rho_{l\ 15°C}$ (g/ml)	1.3795	1.3388

TAB. 5.1. Thermodynamic properties of C_3F_8 and C_2ClF_5 [61].

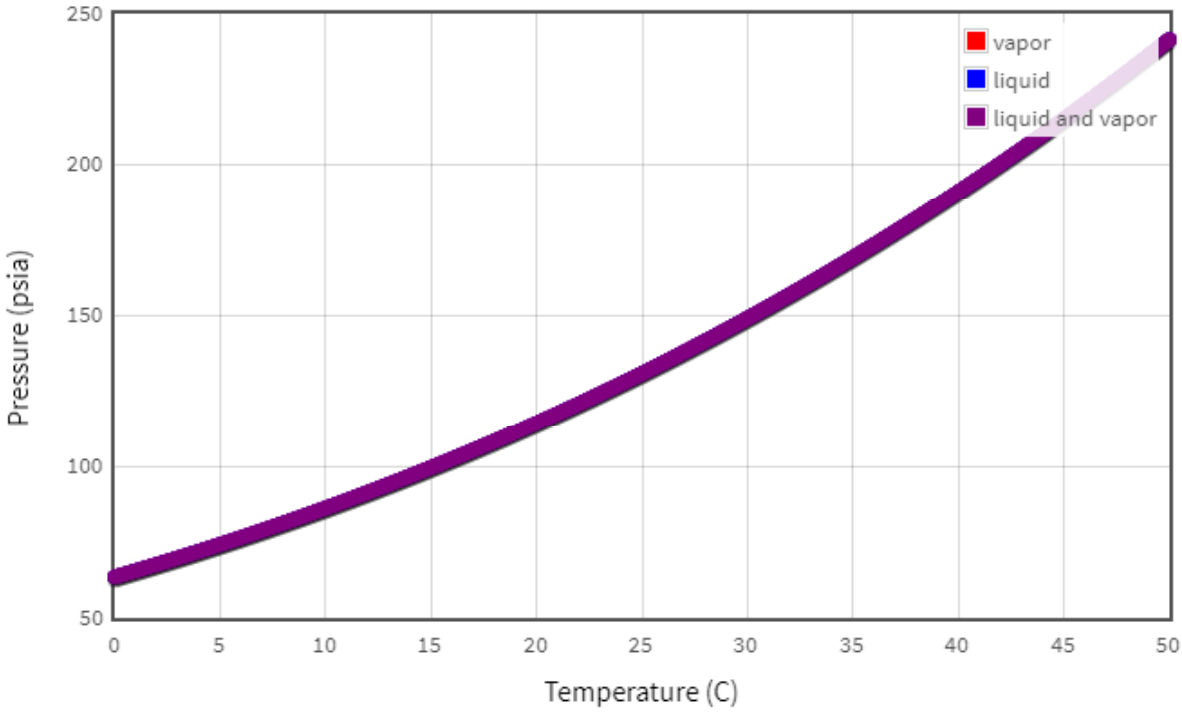

FIG. 5.1. C_2ClF_5 vapor pressure as a function of temperature [61].

compares both for a few properties. Figure 5.1 then presents the C_2ClF_5 vapor pressure as a function of temperature.

5.2. ^{35}S 17 keV monoenergetic recoil data

This section presents the ^{35}S 17 keV monoenergetic recoil data: how the desired reaction with monoenergetic recoils was obtained, how the sulfur recoil was specifically studied, as well as PICO-0.1 17 keV data and analysis.

5.2.1. Thermal neutrons

In order to obtain thermal neutrons inside the PICO-0.1 detector, we start out with fast neutrons from an antimony-beryllium (SbBe) source: ^{124}Sb is an unstable isotope of antimony, that can be produced at Polytechnique Montreal's SLOWPOKE nuclear reactor [65]; natural antimony (57.21% ^{121}Sb and 42.79% ^{123}Sb) is activated by neutron capture in the reactor, producing ^{122}Sb and ^{124}Sb with half-lives of 2.72 and 60.20 days, respectively. In the present case, three sources were reactivated (they had already been activated in the past), with respective measured activities of 834.7, 566 and 525 μCi on August 3$^{\text{rd}}$, 2016.

^{124}Sb decays into an excited state of ^{124}Te through β^- decay, which de-excites into a lower energy state by emitting gamma-rays with energies of 1691.03 or 2091.70 keV [66]. By putting ^{9}Be beside the ^{124}Sb gamma source, these high-energy gammas can knock out a neutron from the beryllium; neutrons knocked out by 1691.03 keV gammas (97%) come out with 22.8 keV of kinetic energy, and those by 2091.70 keV gammas (3%) with 378 keV.

These fast neutrons are then slowed down by paraffin until they become thermal. Paraffin is a kind of wax made of hydrogen and carbon, therefore having a high stopping power for neutrons (because of its great amount of hydrogen atoms). As shown on figure 5.2, 2.25 cm of paraffin are enough to thermalize the great majority of the 22.8 keV neutrons; a thickness of 4 cm of paraffin was used for this study. By placing the SbBe neutron source and paraffin next to PICO-0.1, a sufficient flux of thermal neutrons reaches the chamber and allows to study the reaction

$$^{35}\text{Cl}\ (n_{th}, p)\ ^{35}\text{S}\ . \tag{5.2.1}$$

5.2.2. Sulfur and proton recoils

Via the reaction 5.2.1, a sulfur nucleus and proton recoils with energies of 17 keV and 600 keV respectively are produced inside the PICO-0.1 detector. According to the critical

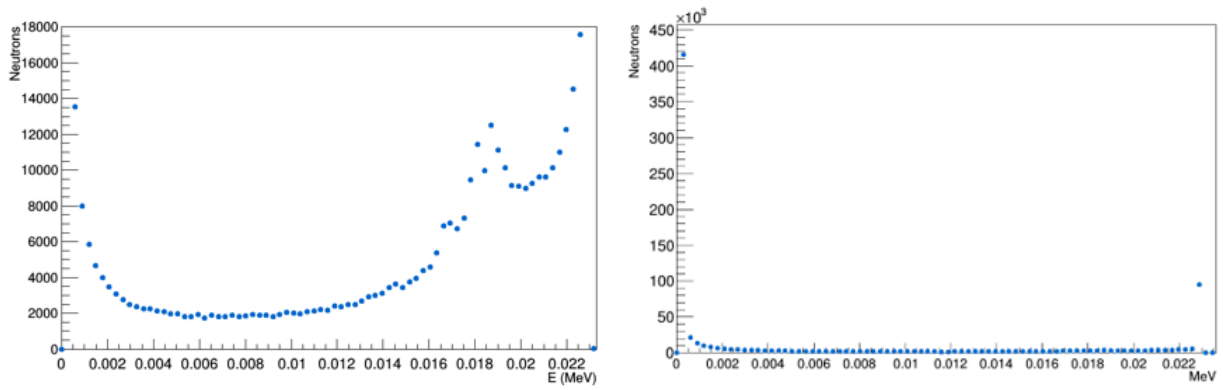

FIG. 5.2. Thermalizing 22.8 keV neutrons with 2.25 cm of paraffin : on the left, the original 22.8 keV spectrum; on the right, the spectrum after passing through the paraffin.

energy criterion of the Seitz model (§4.3.1), both of these recoils should create bubble events at energy thresholds between 0 and 17 keV. However, from the dE/dx criterion (§4.3.2), no proton events are expected at thresholds higher than a few keV. Indeed, since protons are light, charged and fast, they will mostly interact with electrons and deposit small amounts of energy within L_C; they will lose all of their 600 keV along extended tracks in the superheated liquid. Thus, even at thresholds as low as a few keV, their small energy depositions along their track will not be sufficient to create bubbles in the detector. Only the 17 keV sulfur nuclei deposit enough energy above threshold and can therefore be used to characterize precisely the Seitz threshold.

As detailed in section 4.4, the expected response from a PICO threshold detector is an integral of the recoil energy spectrum above the threshold energy. For a monoenergetic spectrum such as for the 17 keV sulfur recoils, integrating a Dirac delta function results in a step (or Heaviside) function, as shown on figure 5.3. Therefore, the $^{35}Cl\ (n_{th}, p)\ ^{35}S$ data can be used to characterize the Seitz threshold, specifically its precise location and its steepness.

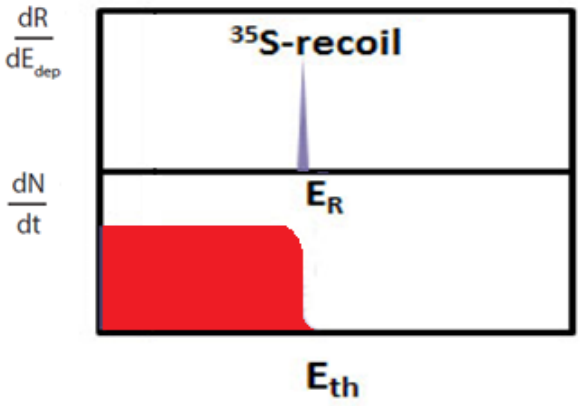

FIG. 5.3. Expected PICO-0.1 response to 17 keV monoergetic sulfur nucleus recoils from ^{35}Cl (n_{th},p) ^{35}S. At the top, the (monoenergetic) recoil energy spectrum. At the bottom, the expected count rate response by varying the threshold below E_{th}.

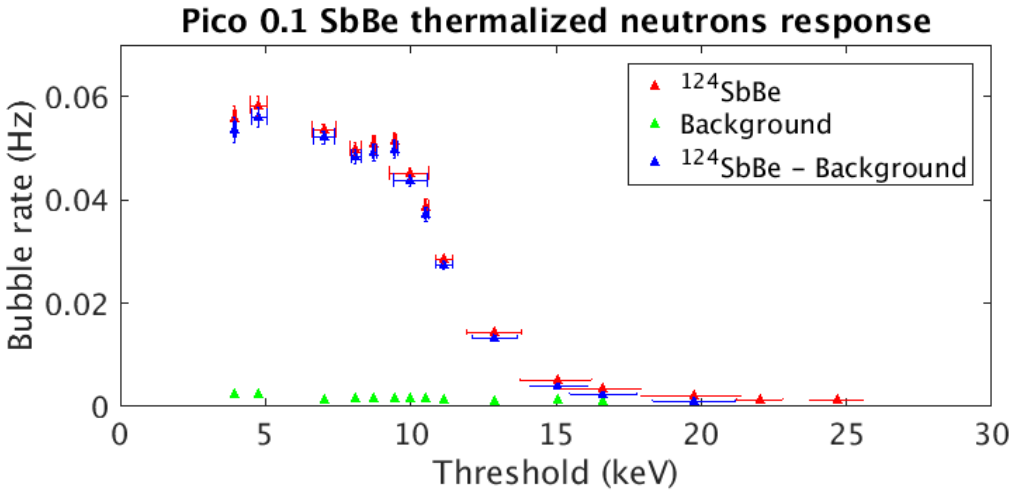

FIG. 5.4. PICO-0.1 response to thermal neutrons with the reaction ^{35}Cl (n_{th},p) ^{35}S, producing 17 keV monoenergetic ^{35}S recoils.

5.2.3. Data

The count rate response obtained with PICO-0.1 is shown on figure 5.4. Instead of a sharp step at 17 keV (as on the bottom of figure 5.3), a much smoother, slowly rising step, starting at a lower energy than 17 keV is observed. The count rate starts to rise at around 17 keV, and reaches its half-height at about 11 keV. The full plateau is reached 10 keV. An explanation of this behavior is given in the following sections.

5.3. *SRIM* SIMULATIONS

In order to explain the behavior of the 17 keV monoenergetic recoil data in PICO-0.1 shown on figure 5.4, a comparison with simulations made with the *SRIM* program (*Stopping and Range of Ions in Matter*) was performed. This program allows to calculate and simulate interactions and tracks of ions of given energy in a given material. In this case, tracks of 17 keV ^{35}S were simulated in C_2ClF_5.

5.3.1. Bubble efficiency

Given the recoil energy of a given nucleus and the critical parameters of the Seitz model, *SRIM* can be used to calculate the efficiency for bubble formation in C_2ClF_5. Indeed, from the energy deposited by a recoiling sulfur nucleus along its track, and from the critical radius and energy (R_C and E_C respectively) needed to form a bubble (section 4.3), one can determine if the simulated recoil creates a bubble or not. In order to do so, the energy depositions along the ion track are obtained from *SRIM*. Then, a window of critical length $L_C = b \cdot R_C$ is moved along the track and a check is performed whether the critical energy E_C was deposited inside this window, by taking the area under the curve (dE/dx vs. distance). If this is the case, a bubble event can be formed; if not, the recoil did not produce any nucleation. An example for both cases is shown on figure 5.5. Repeating this a large number of times for a given recoil, the predicted bubble efficiency (bubble events over all events) at a given threshold energy can be calculated:

$$\varepsilon(E_{th}) = \frac{\#\ of\ events\ with\ nucleation\ at\ E_{th}}{total\ \#\ of\ events\ at\ E_{th}} \tag{5.3.1}$$

Using this method, efficiency curves can be calculated at any threshold energies and and fitted to the 17 keV ^{35}S recoils data (figure 5.4); since *SRIM* gives separate contributions to the energy deposition (nuclear and electronic recoils), one can also calculate efficiency curves for each of them, in addition to the curve for the total deposited energy. In order to produce said curves, the proper critical radius R_C for each critical energy E_C has to be

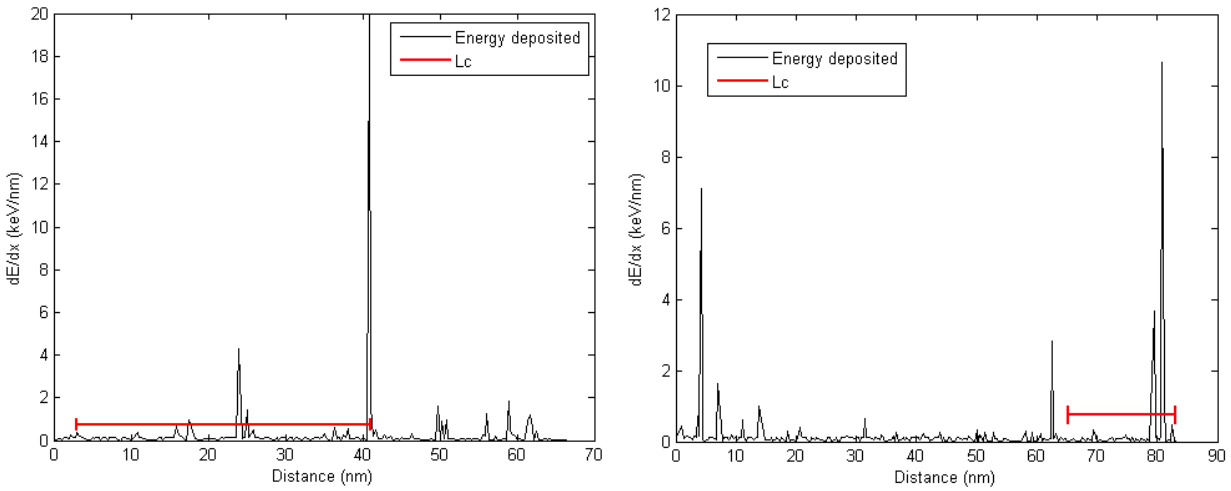

FIG. 5.5. Example of searching for a bubble event in *SRIM*. On the left, sufficient energy was deposited inside the critical length, and nucleation occurs. On the right, The end of the track is reached without ever having enough energy deposited inside the critical length to create a bubble; no nucleation occured.

determined; those are calculated from the Seitz model at either a constant temperature or constant pressure. Results are shown in figure 5.6 for constant temperature (since this is the common mode of operation for a PICO detector, i.e. the pressure is varied while keeping the temperature constant).

In the following sections, different efficiency curves are produced by varying parameters that affect the efficiency and/or the Seitz threshold, with the aim to try to obtain a curve that could explain best the behaviour of the 17 keV data.

5.3.2. Harper parameter

First, an effort was made to reproduce the 17 keV data by finding a Harper parameter b that would generate an efficiency curve with a similar shape. By varying from $b = 0.1$ to $b = 2$, the curves shown on figure 5.7 were obtained. As can be seen, none of them results in the correct shape, or even come close to it. At $b = 2$, the predicted total efficiency curve becomes a sharp step at 17 keV, rising to maximum efficiency; for a critical energy smaller than the recoil energy, the bubble efficiency is 100%. Therefore, it would be the same for

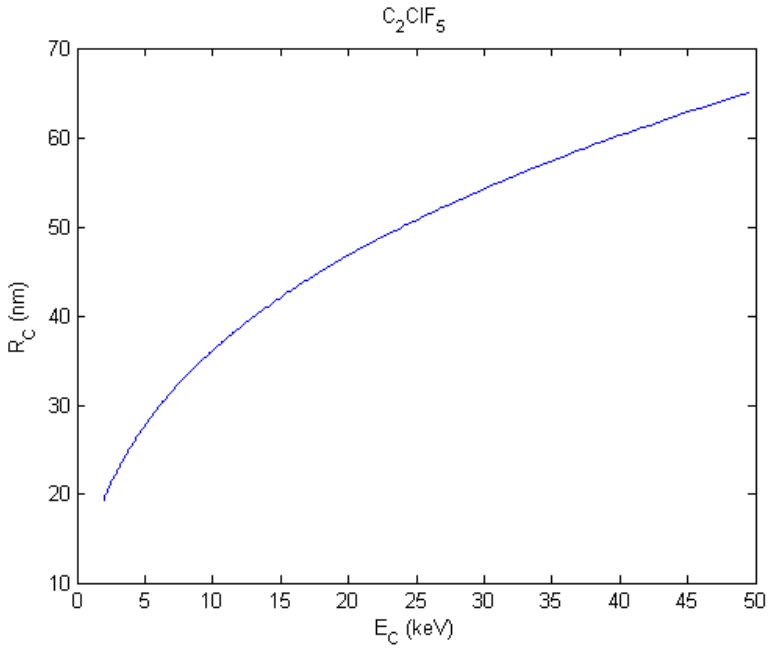

FIG. 5.6. Relation between the critical radius R_C and the critical energy E_C calculated from the Seitz model for C_2ClF_5, here at a constant temperature of 15°C.

larger b's too - the greater the b, the larger the efficiency. One would only obtain a larger nuclear recoil efficiency, which is not yet maximum for $b = 2$.

One can then try to "fine-tune" the Harper parameter to fit the data. This is shown in figure 5.8, with the best fit obtained with

$$b = \frac{100}{(E_C/keV)^{2.2}} \tag{5.3.2}$$

However, in previous experiments, it was shown that the Harper parameter cannot decrease with increasing critical energy, and therefore that parametrisation cannot be a valid approach. Since it was not possible to fit the data without a decreasing or with a constant Harper parameter, it was concluded that the Harper parameter alone cannot explain the behaviour of the 17 keV data, and that other physical explanations had to be explored to reproduce the data.

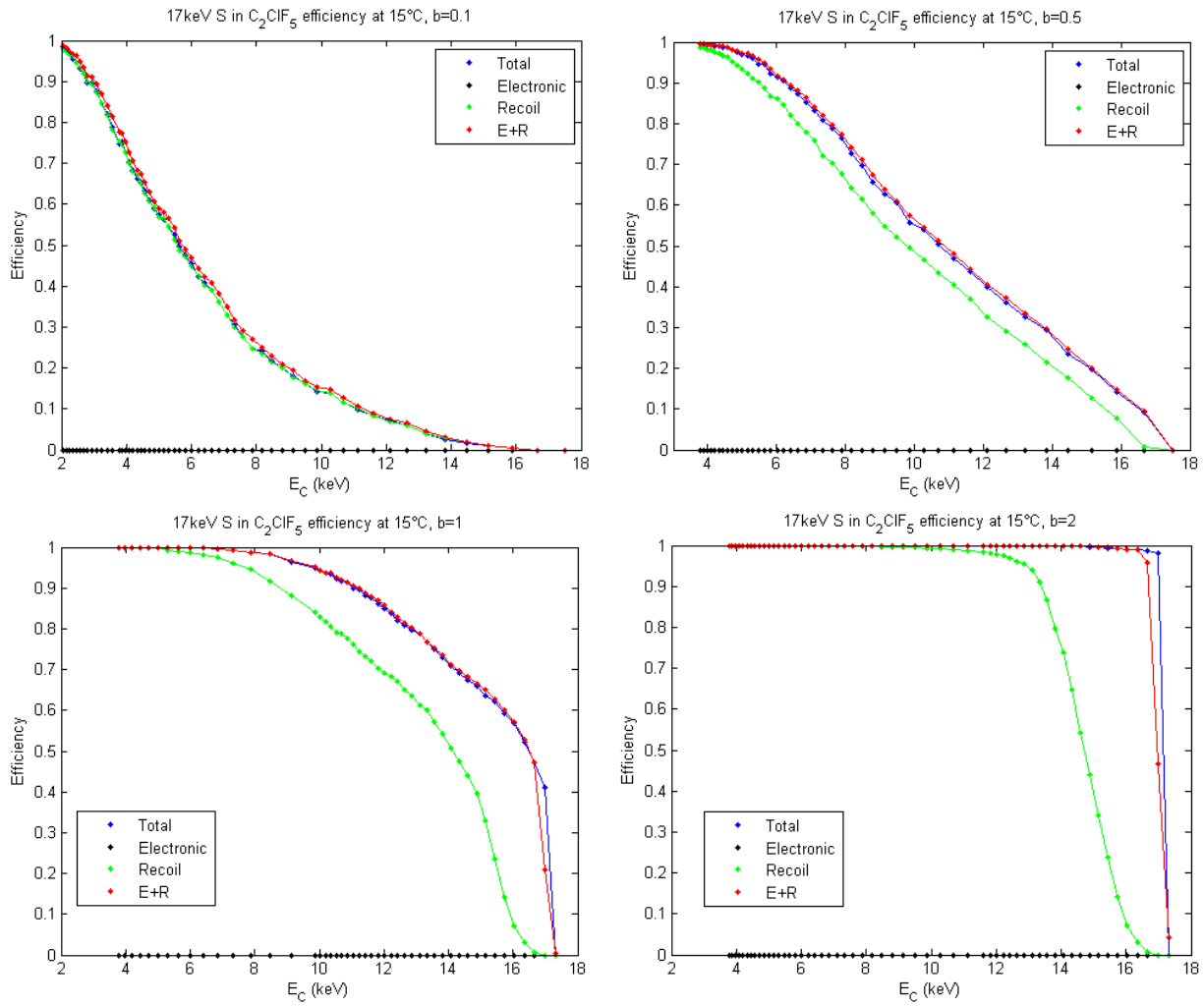

FIG. 5.7. Efficiency curves produced with *SRIM* for 17 keV ^{35}S nucleus recoils in C_2ClF_5, for different b parameters. From top-left to bottom-right : $b = 0.1$, $b = 0.5$, $b = 1$ and $b = 2$. Each efficiency point is calculated with 1000 *SRIM* recoil simulations.

5.3.3. Surface tension

In a second try, the hypothesis that the surface tension used in the Seitz model is not correctly considered was investigated; indeed, usually the Seitz threshold is calculated assuming a planar surface tension instead of a spherical one, as for a bubble. In fact, it was found that the surface tension for a spherical surface could be as much as 7% larger than for the planar case used in the Seitz Model; modifying the surface tension this way would modify the Seitz threshold as shown on figure 5.9. Considering this modification, the Seitz threshold and its correspondent efficiency were recalculated; the result is shown on

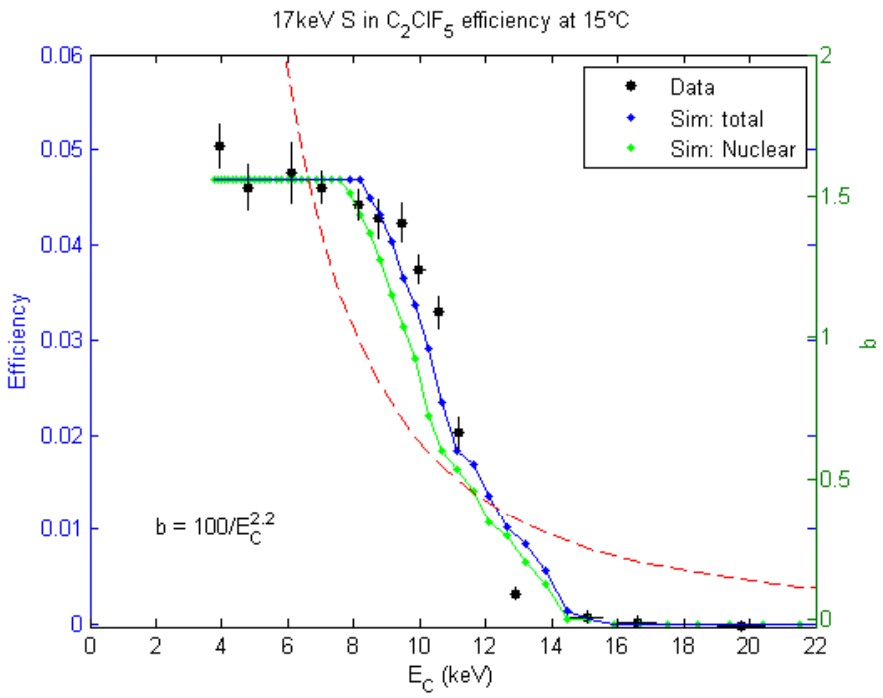

FIG. 5.8. "Fine-tuning" the Harper parameter to reproduce the 17 keV data. We use $b = \frac{100}{(E_C/keV)^{2.2}}$. Efficiency is in arbitrary units. Each efficiency point is calculated with 100 *SRIM* recoil simulations.

figure 5.10. At this point, the Seitz threshold is shifted to the right, closer to a real 17 keV step, but the data still cannot be reproduced with *SRIM*. Although the nuclear-recoil-only efficiency curve resembles a lot to the real data, there is no physical reason to believe that only nuclear recoils, and not electronic recoils, contribute to the formation of bubbles. This hypothesis is therefore rejected, and it is concluded that a modification from a planar to a spherical surface tension is not sufficient to explain the behaviour of the 17 keV data.

5.3.4. Heat dissipation

In a third approach, the process of heat dissipation during the formation of bubbles in a superheated liquid was explored. From the work of Denzel, Diemand and Angélil [67] on molecular dynamics simulations, one expects that the heat dissipation during the bubble formation can be 3 to 10 times faster than the bubble growth itself. This could result in a loss of energy deposited in the superheated liquid that was approximated to be about

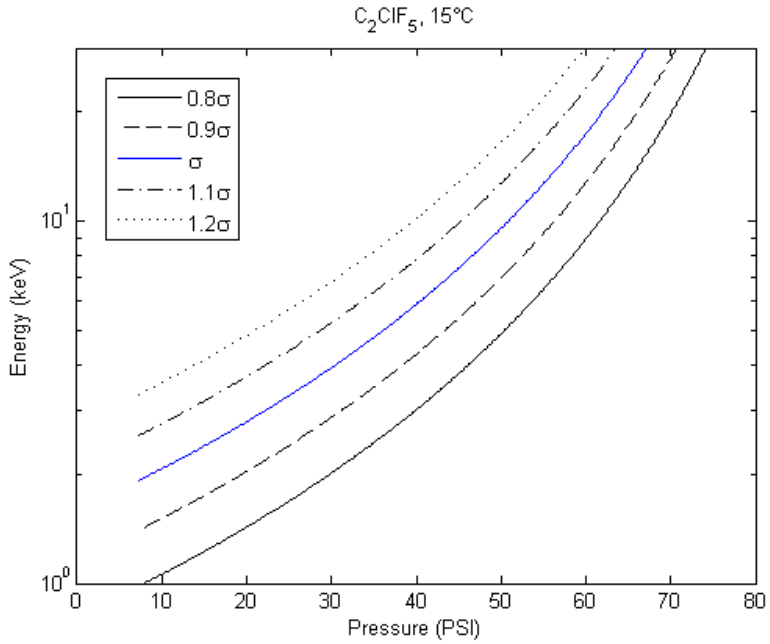

FIG. 5.9. Seitz threshold recalculated with smaller and larger surface tensions (0.8 to 1.2 times the original), for C_2ClF_5 at 15°C.

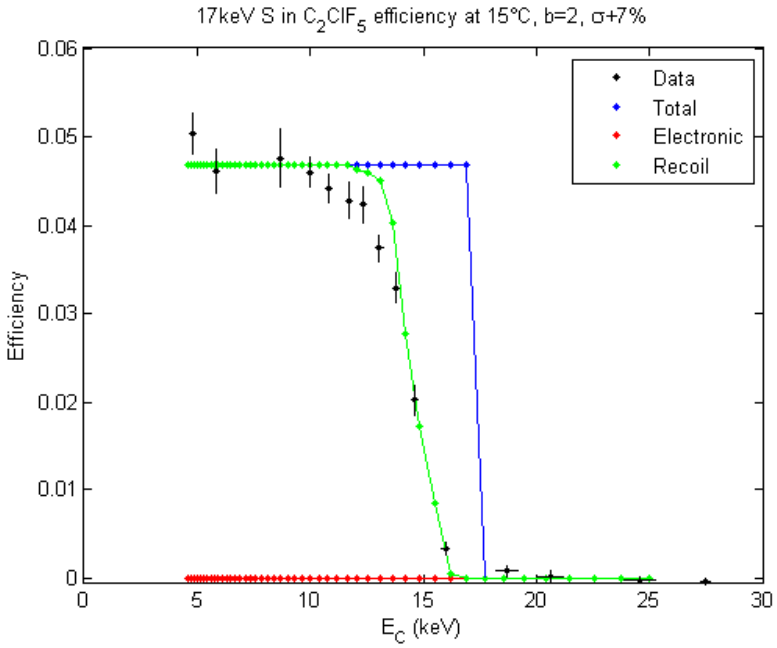

FIG. 5.10. Efficiency curve produced with *SRIM* for 17 keV ^{35}S nucleus recoils in C_2ClF_5, with a 7% larger surface tension from the Seitz model. $b = 2$ is used. Efficiency is in arbitrary units. Each efficiency point is calculated with 100 *SRIM* recoil simulations.

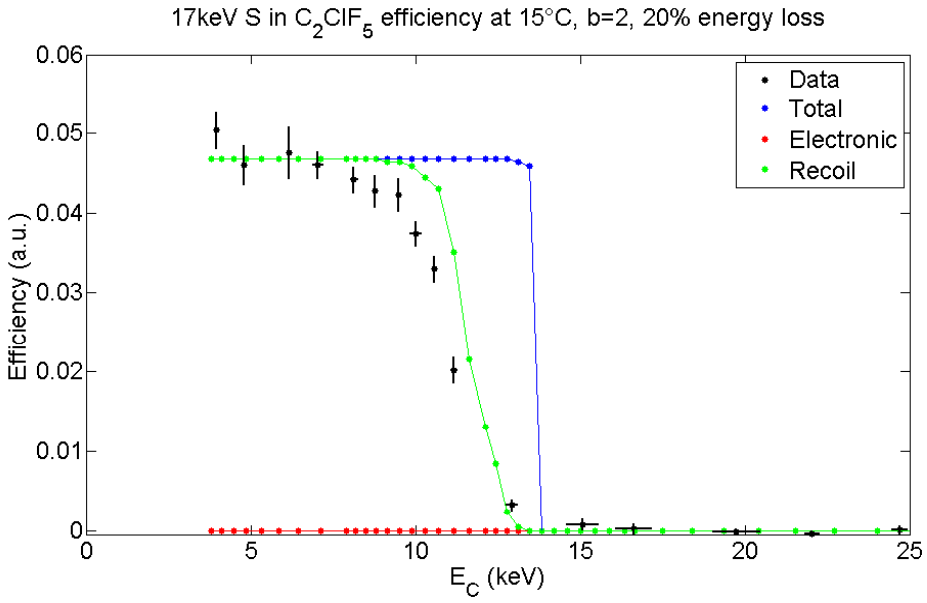

FIG. 5.11. Efficiency curve produced with *SRIM* for 17 keV ^{35}S nucleus recoils in C_2ClF_5, with a 20% energy loss from the original recoil and the energy deposition. $b = 2$ is used. Each efficiency point is calculated with 100 *SRIM* recoil simulations.

20%. This effect was included in *SRIM* by removing 20% of the recoil energy and all energy depositions on the tracks; the efficiency obtained is shown on figure 5.11. Not unexpected, the curve is pretty much the same as the one in figure 5.7 (bottom right, $b = 2$) but shifted down in energy. One could consider a greater energy loss to create a larger shift of the efficiency curve, but one still would not obtain the proper shape to reproduce the data. Therefore, the hypothesis that heat dissipation can explain the 17 keV data was rejected and other physical explanations had to be investigated.

5.3.5. Critical radius distribution

Finally, a more statistical interpretation of the critical radius R_C was considered: in particular, the assumption was made that R_C is part of a distribution instead of having a precise value obtained from the Seitz model. For this purpose, it seems natural to consider the normal (or gaussian) distribution, with mean μ and standard deviation σ, as generically described by:

$$f(x) = \frac{1}{\sqrt{2\pi\sigma^2}} \exp\left(-\frac{(x-\mu)^2}{2\sigma^2}\right) \tag{5.3.3}$$

From this, R_C is now taken as a normally distributed random value around the Seitz model R_C (renamed R_{C_S} here), from a distribution of standard deviation $\sigma = \epsilon R_{C_S}$; ϵ is a free parameter, typically taken between 0 and 1. Thus, for each *SRIM* simulation made for calculating the nucleation efficiency, a randomly generated value is selected from the R_C distribution centered on R_{C_S}. This way, the intended probability distribution for the critical radius is obtained.

Having different, normally distributed R_C's for each simulation of an efficiency point (efficiency at a given E_C) would have the effect of smoothening the efficiency curve, since R_C distributions at different E_C's would overlap; instead of a distinct R_C for each E_C as on figure 5.6, R_C distributions would make each efficiency point more similar to each other, as they would have similar R_C's. Some results are shown on figures 5.12 and 5.13, respectively with $b = 1$ and $b = 2$. Once again, it turned out that the 17 keV data could not be reproduced. An R_C distribution does not really affect the curve for $b = 2$, nor for $b = 1$.

Finally the two last attempts were combined, namely a gaussian-distributed R_C and an energy loss from heat dissipation; the result is shown on figure 5.14. The nuclear-recoil-only efficiency curve is once again close to the data, but the total efficiency can still not explain it. Noting that a R_C normal distribution does not affect much the efficiency curve, no attempt was made for other types of distributions; only unusual shapes could have the effect needed, and therefore would not be motivated from a physics point of view.

Therefore, a completely different approach, i.e. revisiting the Seitz threshold itself, is presented in the next section.

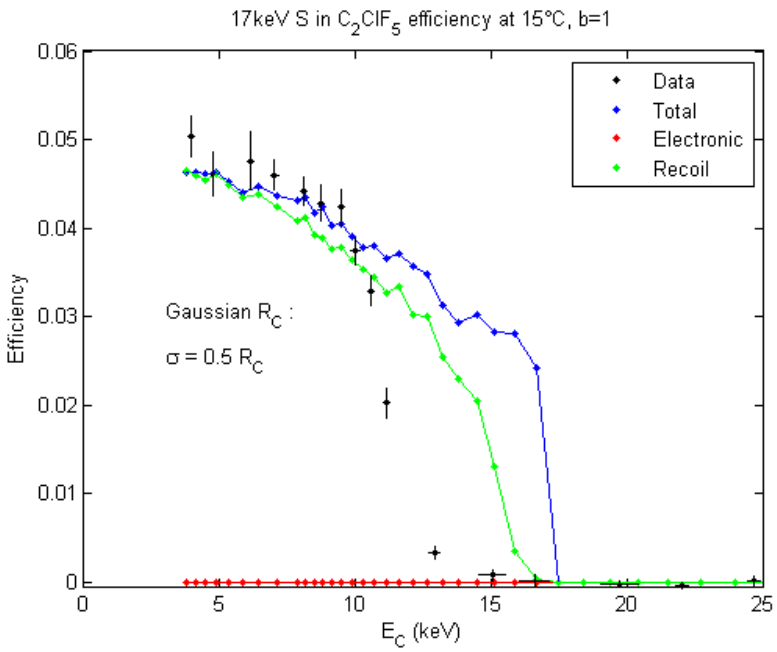

FIG. 5.12. Efficiency curve produced with *SRIM* for 17 keV ^{35}S nucleus recoils in C_2ClF_5, with a gaussian-distributed R_C, of mean $\sigma = 0.5R_C$. $b = 1$ is used. Each efficiency point is calculated with 500 *SRIM* recoil simulations.

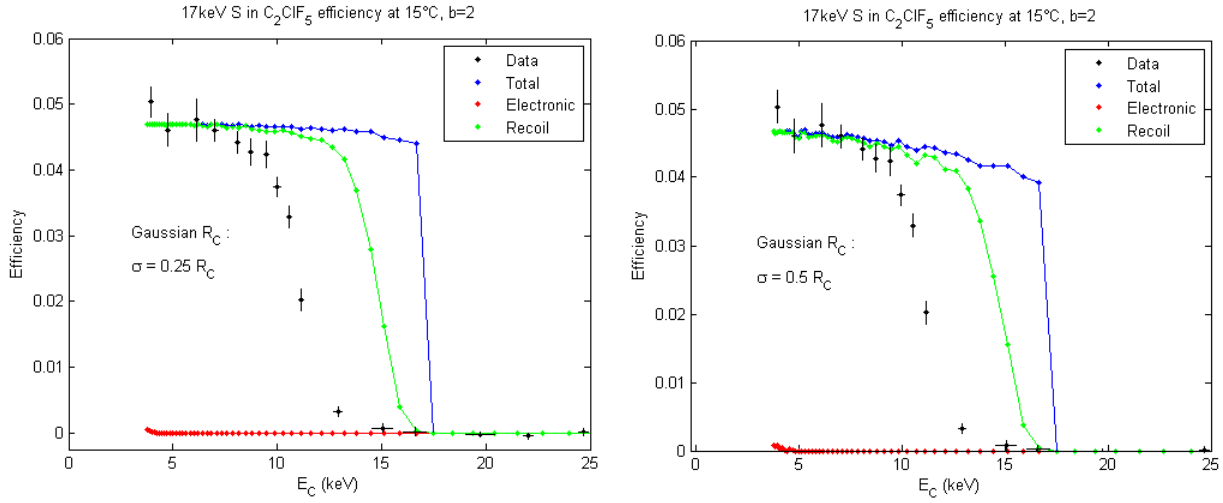

FIG. 5.13. Efficiency curve produced with *SRIM* for 17 keV ^{35}S nucleus recoils in C_2ClF_5, with a gaussian-distributed R_C, of mean $\sigma = 0.25R_C$ (left) and $\sigma = 0.5R_C$ (right). $b = 2$ is used. Each efficiency point is calculated with 500 *SRIM* recoil simulations.

5.4. GAUSSIAN BLURRED STEP SEITZ THRESHOLD

Being up to now unable to come up with a simple physical explanation of the behaviour of the 17 keV data, the question was asked how to best describe the observed threshold in a

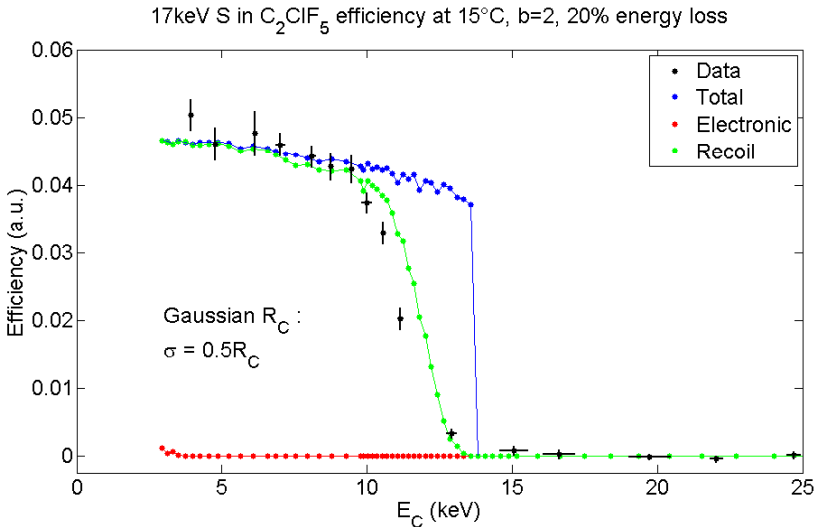

FIG. 5.14. Efficiency curve produced with *SRIM* with a gaussian-distributed R_C, of mean $\sigma = 0.5R_C$, and with a 20% energy loss from the original recoil and the energy deposition. $b = 1$ is used. Each efficiency point is calculated with 500 *SRIM* recoil simulations.

mathematical form and then seek to understand it. Therefore, an intrinsic resolution to the response of energy depositions in superheated fluids was tried out, possibly due to energy loss in dissipation (see section 5.3.4, [**67**] for more details) and other effects. The original Seitz threshold can this way be considered as a Heaviside limit of a Gaussian blurred step (GBS) function, of mean μ and width σ, as illustrated on figure 5.15. The GBS (or sigmoid) gives a smoother rise to a plateau than a Heaviside function, and is defined as:

$$H(x) \equiv \frac{1}{2}\,\mathrm{erfc}((\mu - x)/\sigma) \tag{5.4.1}$$

with erfc the complimentary error function

$$\begin{aligned} \mathrm{erfc}((\mu - x)/\sigma) &\equiv 1 - \mathrm{erf}((\mu - x)/\sigma) \\ &\equiv \frac{2}{\sqrt{\pi}} \int_x^\infty e^{-\left(\frac{\mu - y}{\sigma}\right)^2} dy \ . \end{aligned} \tag{5.4.2}$$

The Heaviside function is obtained by taking the limit $\sigma \to 0$ in equation 5.4.1.

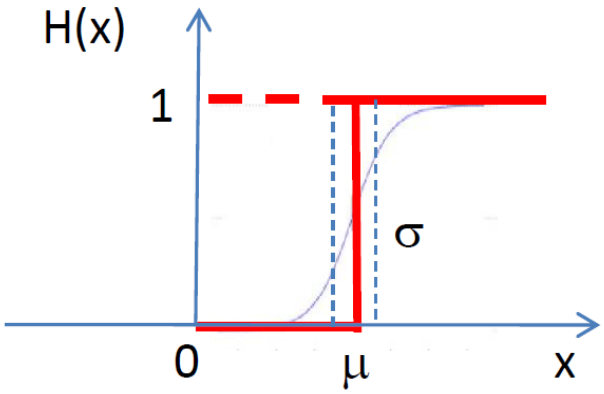

FIG. 5.15. The Gaussian blurred step function in grey (with mean μ and width σ), compared to the Heaviside function in red.

Given this, one can then find the probability for the detection of a recoil of energy E_R, which is given as a GBS centered on $E_R = E_{GBS}$, near E_{th}:

$$P(E_R,E_{GBS}) = \frac{1}{2}\left[\text{erfc}\left(\frac{E_{GBS}-E_R}{\sigma}\right) - \text{erfc}\left(\frac{E_{GBS}}{\sigma}\right)\right] \tag{5.4.3}$$

where $\text{erfc}\left(\frac{E_{GBS}}{\sqrt{2}\sigma}\right)$ is introduced to set the probability at $E_R = 0$ to 0, i.e. $P(0,E_{th}) = 0$. E_{GBS} can deviate from E_{th} as it is possible that the event probability begins to rise only at $E_R = E_{th}$, or even at a greater energy $E_R > E_{th}$. Two examples for this probability function (for two different E_{GBS}) are illustrated on figure 5.16.

The same way, a detector response ε for a monoenergetic recoil of energy E_R, as a function of the threshold energy E_{th}, can be given by:

$$\varepsilon(E_{th}) = \frac{1}{2}\left[\text{erfc}\left(\frac{E_{th}-E_0}{\sigma}\right)\right] \ , \tag{5.4.4}$$

where $E_0 < E_R$ is the energy at half-height of ε; examples are shown on figure 5.17.

Defining the energy shift ΔE as

$$\Delta E \equiv E_{dep} - E_0 \ , \tag{5.4.5}$$

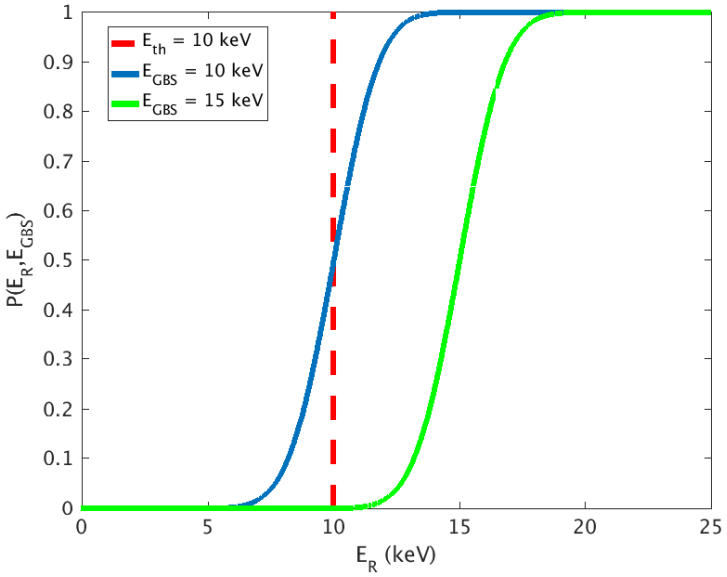

FIG. 5.16. Gaussian blurred step event probability P in function of the recoil energy E_R, for $E_{GBS} = 10$ keV (blue) and $E_{GBS} = 15$ keV (green), and for a given original Seitz threshold of $E_{th} = 10$ keV. Both probability curves have $\sigma = 2$ keV, the width of the GBS.

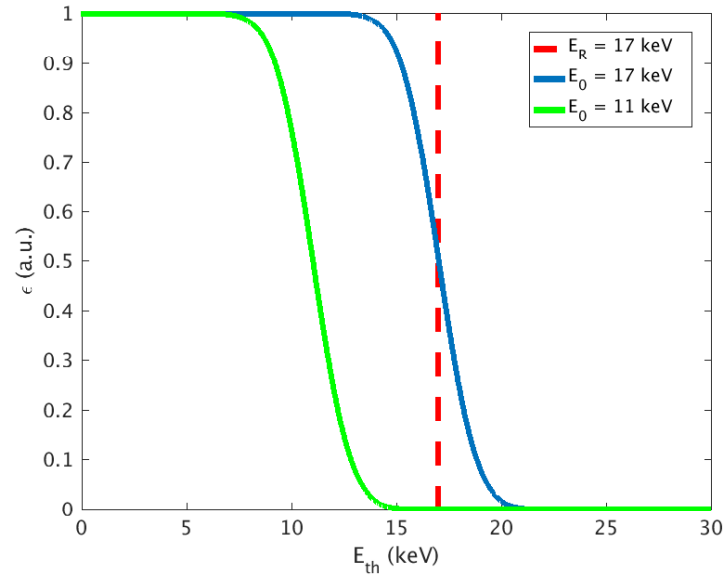

FIG. 5.17. Gaussian blurred step detector efficiency ϵ as a function of the threshold energy E_{th}, for $E_0 = 17$ keV (blue) and $E_0 = 11$ keV (green), and for a given monoenergetic recoil energy of $E_R = 17$ keV. Both efficiency curves have $\sigma = 2$ keV, the width of the GBS.

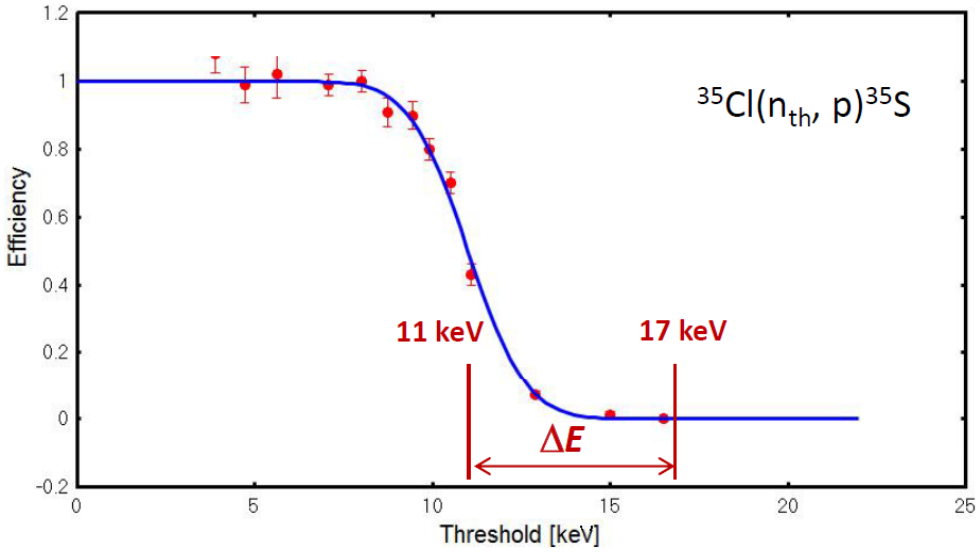

FIG. 5.18. Fit of the 17 keV data with a GBS threshold of $E_0 = 11$ keV and width $\sigma = 2$ keV. We notice a $\Delta E = 6$ keV.

where E_{dep} is the deposited energy (monoenergetic recoil energy), we can then reproduce the 17 keV data with a GBS Seitz threshold, as shown on figure 5.18.

By doing the same with other monoenergetic calibrations, one can then study trends for the ΔE shift and the width σ: on figures 5.19 and 5.20 are shown two previous monoenergetic calibrations done with PICASSO detectors - droplet detectors using the same principle as PICO detectors but with thousands of millimeter-sized droplets of superheated liquid in a gel array - using C_4F_{10} as the active fluid. Figure 5.19 shows the data of ^{214}Po alpha decay into $^{210}\mathrm{Pb} + \alpha$, producing a monoenergetic 150.7 keV ^{210}Pb recoil. The detector response is centered at $E_0 = 141$ keV, resulting in a shift of $\Delta E = 10$ keV; the response has a width of $\sigma = 16.8$ keV. Figure 5.20 shows another set of monoenergetic recoil data: 5.49 MeV alpha recoils from the alpha decay of ^{241}Am into $^{237}\mathrm{Np} + \alpha$. Alpha recoils are different from nuclear recoils because they deposit their energy on long distances, making them quite inefficient for bubble formations along most of their ranges (section 4.3.2). Therefore, they begin to create bubbles at the end of their track (the "Bragg peak"), and at much lower energies than their original kinetic energies. Since only the dE/dx on the track is known, but not the b parameter, the energy shift ΔE cannot be inferred in this case. However, one

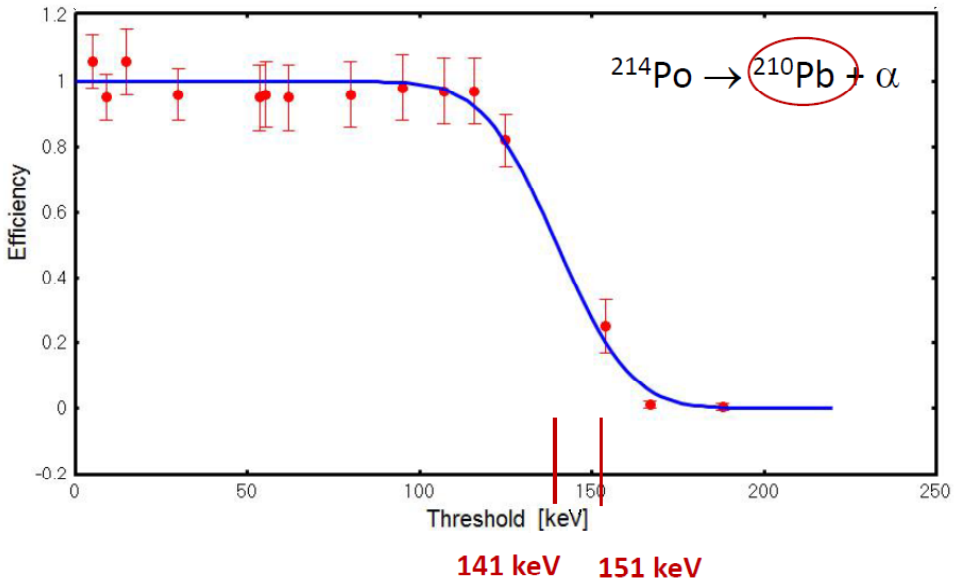

FIG. 5.19. Fit of the 151 keV monoenergetic ^{210}Pb recoil data, with a GBS threshold of $E_0 = 141$ keV and width $\sigma = 16.8$ keV. We notice a $\Delta E = 10$ keV.

can still study the efficiency curve of this monoenergetic data, and define its parameters E_0 and σ. It is found that alphas begin to create bubbles at $E_0 = 71$ keV, with a GBS of width $\sigma = 6.4$ keV.

Table 5.2 summarizes the GBS threshold parameters obtained from the study of the monoenergetic recoil data. Both ΔE and σ increase with E_{dep}, while the intrinsic resolution of the GBS σ/E_{dep} seems to remain about constant, around 10%. A further analysis could be done with more monoenergetic data calibrations, to obtain more precise information about trends for ΔE and σ, and to determine better the intrinsic resolution of the Gaussian blurred step threshold. However, it has been clearly shown that the threshold for PICO detectors can be phenomenologically well described by a sigmoid function with resolution σ and shift in energy ΔE; what is still to be done is to determine a mechanism which describes this behaviour and for this, more experimental data are needed.

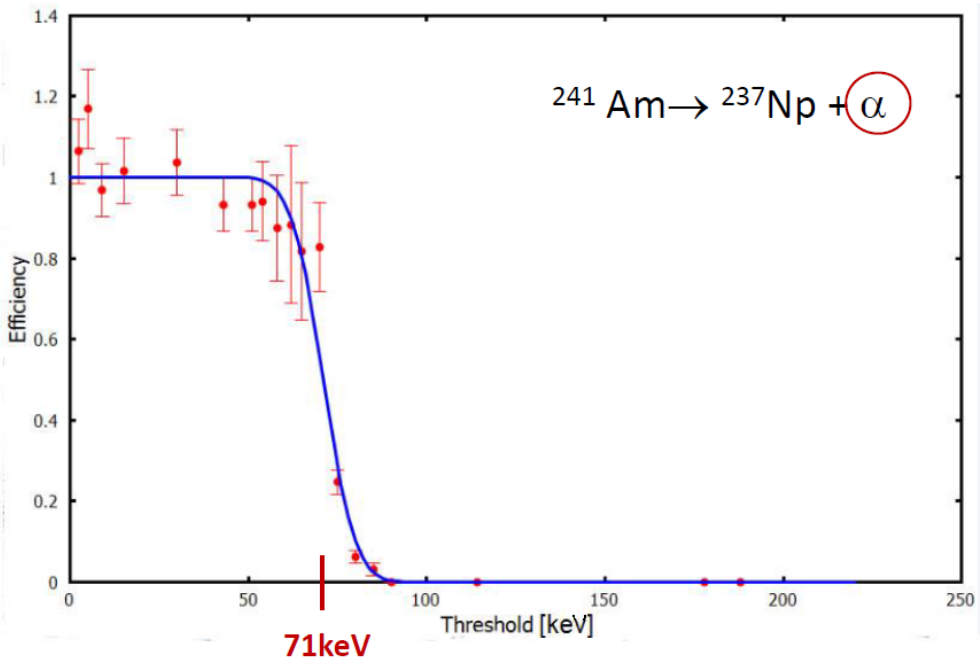

FIG. 5.20. Fit of the 5.49 MeV monoenergetic alpha recoil data with a GBS threshold of $E_0 = 71$ keV and width $\sigma = 6.4$ keV. ΔE is irrelevant here for reasons stated in the text.

E_{dep} (keV)	E_0 (keV)	ΔE (keV)	σ (keV)	σ/E_{dep}
17	11	6	2	0.12
$\gtrsim 71$	71	-	6.4	0.09
151	141	10	16.8	0.11

TAB. 5.2. Summary of GBS thresholds parameters obtained from monoenergetic recoils data. We assume that the energy deposited from the 5.49 MeV alphas to form bubbles was about (and perhaps a bit above) $E_0 = 71$ keV.

Chapter 6

DETECTING PROTON RECOILS WITH PICO-0.1

In order to search for low mass WIMPs, as low as the GeV scale, scattering on light target nuclei would substantially improve the sensitivity reach of PICO. For nuclear recoils such as carbon and fluorine, PICO detectors are already well calibrated and their response are well-known (see section 4.4). In this chapter, their response to proton recoils is studied: these recoils have never been studied in PICO detectors, and therefore it remained to be shown that they are at all observable. Proton interactions in the detector are expected to be similar to the ones from alpha particles (which are also well understood in PICO detectors): charged particles (nuclei) scatter essentially on electrons in the superheated liquid and can create multiple bubbles along their track. A visualisation of a heavy element alpha-decaying and creating events in a PICO detector is shown on figure 6.1. Similar interactions from protons are expected; PICO-0.1 is therefore used to study proton recoils in two different ways: first, from the same reaction studied in the previous chapter,

$$^{35}\mathrm{Cl}\ (n_{th}, p)\ ^{35}\mathrm{S} + 617\ \mathrm{keV}\ , \tag{6.0.6}$$

acoustic signals from the events were analysed in order to deduce the detection of proton recoils; second, proton recoil events were studied directly, from the recoils of hydrogen nuclei in $C_2H_2F_4$.

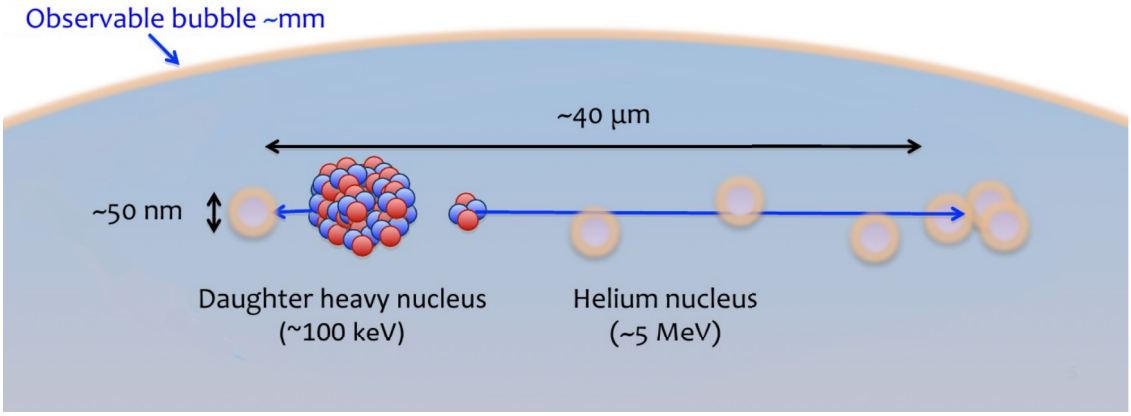

FIG. 6.1. Representation of an alpha particle recoil event, along with an heavy element nucleus recoil.

6.1. 600 KEV PROTON RECOILS IN C_2ClF_5

This section presents the data and analysis for the 600 keV proton recoils from the reaction

$$^{35}\mathrm{Cl}\ (n_{th}, p)\ ^{35}\mathrm{S}\ . \tag{6.1.1}$$

6.1.1. Proton and sulfur recoils

As detailed in the previous chapter, the reaction 6.1.1 produces a pair of monoenergetic recoils: one of 17 keV for the ^{35}S nucleus, and one of 600 keV for the proton; the former was observed and analysed in chapter 5, the latter is now investigated. As explained in section 5.2.2, proton recoils are expected to create bubbles only at low threshold energies. This expectation is furthermore supported by *SRIM* simulations: using the same procedure as described in section 5.3.1 to calculate bubble efficiencies, the 600 keV proton efficiency in C_2ClF_5 is calculated for $b = 1$ and $b = 2$. As seen on figure 6.2, the efficiency rapidly goes to zero as the threshold energy increases, for both cases. PICO-0.1 is therefore operated at low threshold (∼1-5 keV) in order to detect proton recoils.

However, as seen in the previous chapter, recoiling sulfur nuclei are detected with good efficiency from about 15 keV and below. Therefore, in order to observe proton recoil events

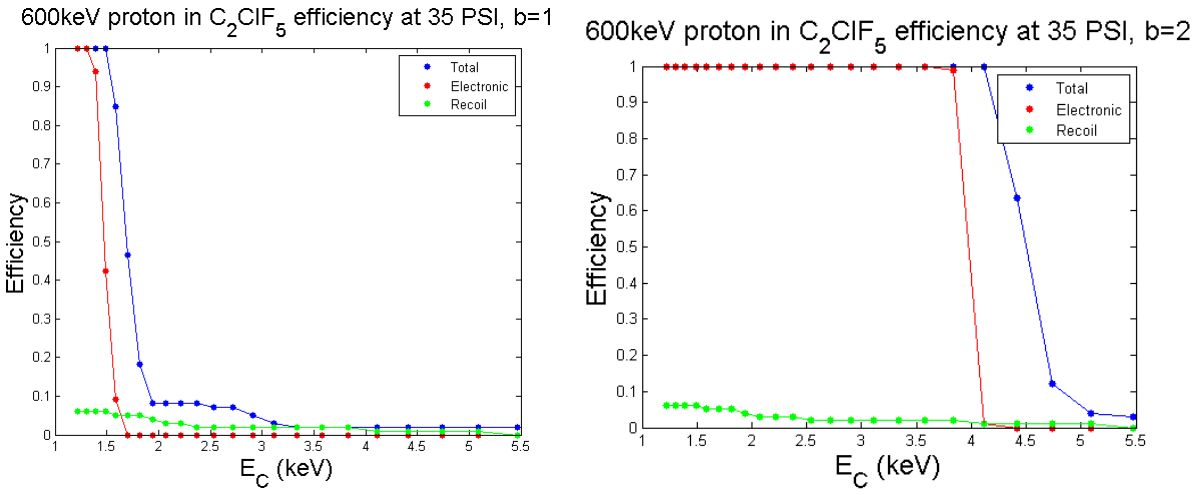

FIG. 6.2. Efficiency curves produced with *SRIM* for 600 keV proton recoils in C_2ClF_5, for $b = 1$ (left) and $b = 2$ (right). Each efficiency point is calculated with 100 *SRIM* recoil simulations.

at low threshold, one cannot isolate them from the sulfur nucleus recoil events; both are always detected together. A visualisation of this type of event, with both proton and sulfur nucleus recoils, is provided on figure 6.3. Thus, as the proton bubble is always alongside a sulfur bubble, the objective would be to distinctly see the proton events. However, this is not directly possible: as the proton has a mean range of about 11.7 μm in C_2ClF_5 (obtained from *SRIM*, see figure 6.4) and the sulfur nucleus of a few tens of nm, PICO-0.1 cameras cannot resolve if the proton created bubbles of its own; all bubbles of an event merge into one observable bubble before they can be separately distinguished. Therefore, in order to detect proton recoils within events including a bubble from the sulfur nucleus recoil, acoustic signals of the events were investigated: as described in section 4.2.1 (and 4.2.2.5 for PICO-0.1), PICO detectors are equipped with piezo-electric transducers that listen to and record the sounds of bubble events; PICO-0.1 has two.

We know that for PICO detectors, the acoustic signal amplitude of a given type of recoil only depends on the pressure and temperature conditions inside the detector, and not on the energy of the incoming scattering particle. Therefore, all nuclei recoils in C_2ClF_5 (whether C, Cl or F) will have similar acoustic signals at a fixed threshold energy point (kept under the same conditions of pressure and temperature). Knowing this, the detection

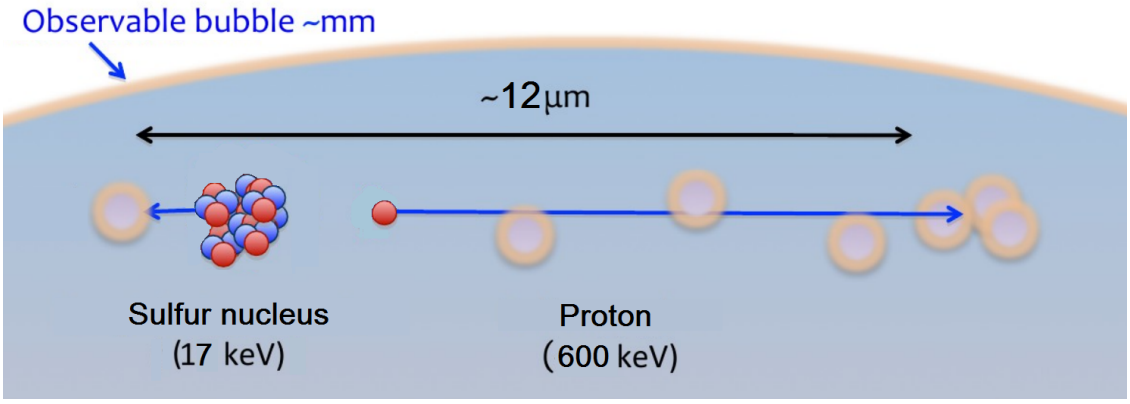

FIG. 6.3. Representation of a complete event from the reaction ^{35}Cl (n_{th}, p) ^{35}S, with both ^{35}S and proton recoils creating bubbles.

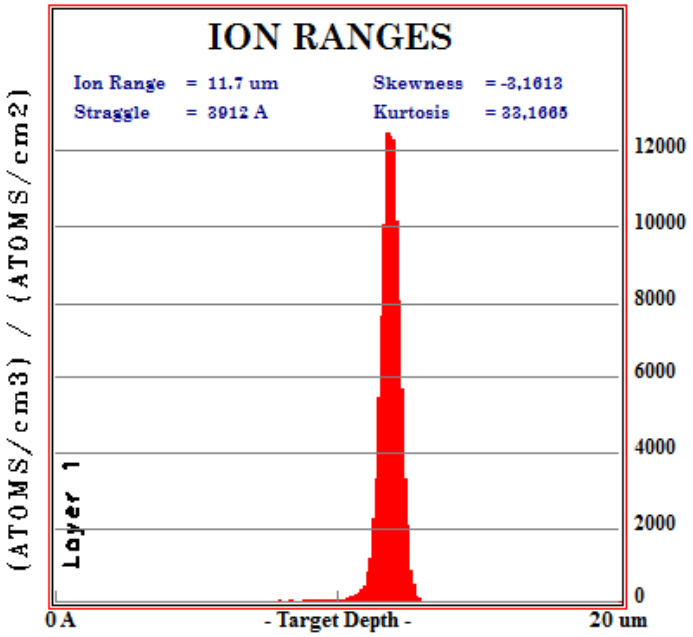

FIG. 6.4. Range distribution for 10^4 600-keV protons in C_2ClF_5.

of proton recoils was studied through the acoustic signal of events in which they occur; their contribution to an event with a sulfur nucleus recoil was analysed. Indeed, an event with only a sulfur recoil will be as of any other nuclear recoil, while an event with a recoiling sulfur combined with bubbles created by the proton will have a different acoustic signature. If the proton creates bubbles by its own, an acoustic signal of greater amplitude than an event with only a nuclear recoil is expected.

6.1.2. Acoustics analysis

In order to study proton recoils in C_2ClF_5, events from the ^{35}Cl (n_{th}, p) ^{35}S reaction are compared with nuclear-recoil-only events; these are obtained from elastic scattering with fast neutrons. As explained in the previous section, nuclear recoils from elastic scattering with fast neutrons will have similar acoustic signals than the ones from sulfur recoils alone, while events with sulfur nucleus and proton events should have a greater acoustic amplitude. To obtain fast neutrons, a 24.6 mCi ^{227}AcBe neutron source (activated at 100 mCi, 1971; half-life 7951 days) is used, with neutron energies ranging from 0 to 10 MeV.

To compare acoustic signals of each type of event, the raw signals recorded from the piezos is used, and treated as follows: the acoustic signal data is squared, and all of the signal is summed over. This gives the acoustic power of the event, in V^2. To compare events on equal footing, the same signal length is selected in each of them; the DAQ recording at a rate of 10^6 data points per second, 25000 points are taken for each acoustic power calculation, resulting in a signal of 25 ms for every event. All events begin at the moment when the bubble is formed; reconstruction of the event allows to have the precise time where the acoustic signal of the bubble begins.

6.1.2.1. *z-position dependence*

First, an effort was made to see if there was a correlation between the acoustic power and the z-position (height) of the event in the detector. As the piezos are located above the active fluid on the outside of the jar of PICO-0.1, it could be expected that the acoustic power decreases as the events are further away from the piezos (smaller z). The observed relation is shown on figure 6.5 at 15 and 25°C, and no correlation was found. Acoustic power has no dependence on its z-position in the detector. The comparison between events can't therefore be based on this relation.

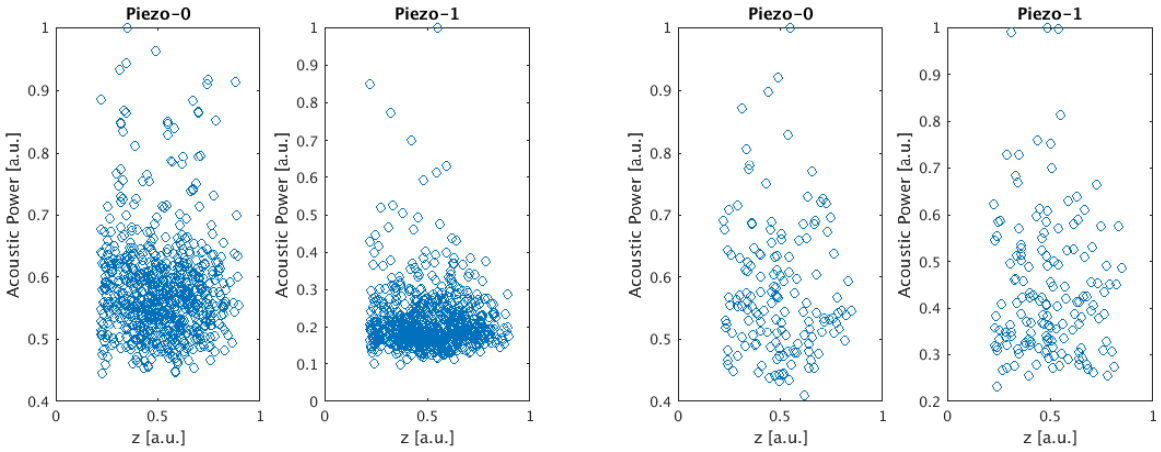

FIG. 6.5. Acoustic power of ^{35}Cl (n_{th}, p) ^{35}S events in function of their height (z) in the detector, at 35 PSI, 15°C (left) and 25°C (right).

6.1.2.2. *Acoustic power distibution*

Subsequently, the acoustic power distribution of all events at a given threshold was studied: the distribution of ^{35}Cl (n_{th}, p) ^{35}S events was compared to the distribution of fast neutron recoil events. The results for six different threshold points is shown on figure 6.6, where indeed some deviations can be seen between distributions at low threshold: for the 1.66 keV, 2.15 keV and 2.72 keV distributions, an excess at high acoustic power is observed for the ^{35}Cl (n_{th}, p) ^{35}S compared to the fast neutron recoils, suggesting that the proton recoils contribute to the acoustic signal by creating their own bubbles. For the three higher threshold distributions, both distributions seem to merge as protons stop creating events of their own. This was to be expected at some point, as explained in section 6.1.1 and from the *SRIM* simulations on figure 6.2: protons can create bubbles at low threshold, and can become increasingly inefficient as the threshold raises to ∼2-5 keV. From figure 6.6, this point where proton detection become inefficient is somewhere between 2.72 and 3.53 keV.

6.1.2.3. *Selection of frequency windows*

To enhance the distinction between the distributions of ^{35}Cl (n_{th}, p) ^{35}S events and fast neutron recoil events, the mean Fast Fourier Transform (FFT) of the acoustic signals from all events of each distribution is used, and shown on figure 6.7. By selecting the proper

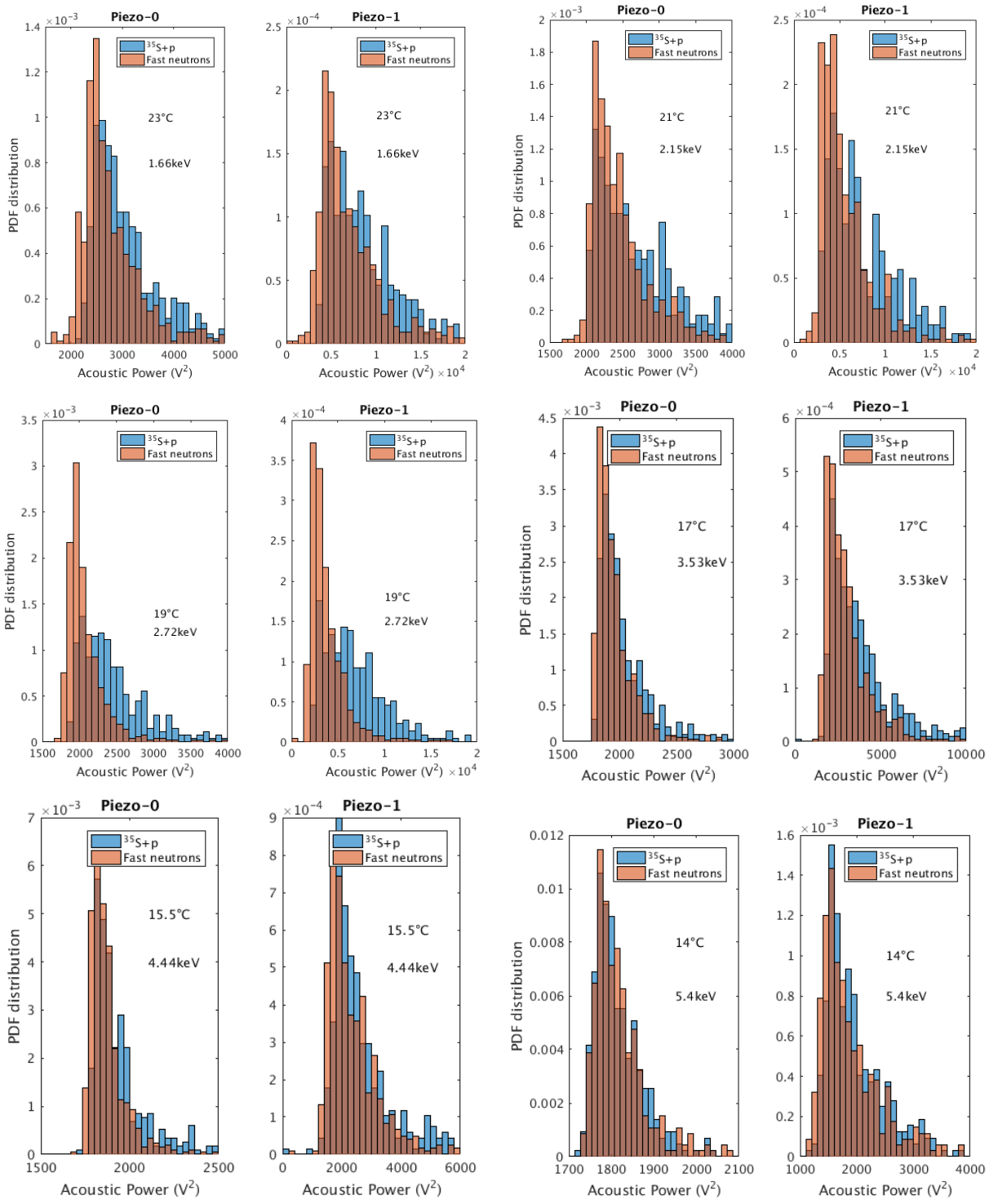

FIG. 6.6. Normalized acoustic power distributions for ^{35}Cl (n_{th}, p) ^{35}S events (blue) and fast neutrons recoil events (red), all at 35 PSI, respectively (from top-left to bottom-right) for 1.66 keV (23°C), 2.15 keV (21°C), 2.72 keV (19°C), 3.53 keV (17°C), 4.44 keV (15.5°C) and 5.4 keV (14°C). The distributions for each threshold point are shown for both piezos.

frequency windows in these FFTs, one can find a way to improve this discrepancy. From the FFTs of figure 6.7, frequency windows were chosen as follows, for all distributions:

$$\begin{gathered}[0.3,0.5] \cup [1.1,1.3]\text{x}10^5 \text{ Hz, for piezo-0} \\ [0.3,1.3]\text{x}10^5 \text{ Hz, for piezo-1}\end{gathered} \tag{6.1.2}$$

A visual representation of this frequency window selection is shown on figure 6.8, where dark sections are ignored for the next calculations. Using these frequencies only, new acoustic power distributions are obtained, as shown on figure 6.9. Since one cannot select precise frequencies directly from the raw acoustic signal, these acoustic powers were calculated by squaring the FFT of each event (in the selected frequency windows as mentioned), instead of squaring the acoustic signal itself; they are no more given in V^2 dimensions, but in arbitrary units. The original discrimination is now enhanced for the three distributions at lower thresholds, and has remained the same for the two distributions at higher thresholds; the distributions at 3.53 keV now show a small deviation, suggesting the protons might still have a small but none-zero bubble efficiency at this threshold.

From these results, it was concluded that protons do indeed produce bubble events, as it was intended; they do this with good efficiency below ~3 keV.

6.1.3. Harper Parameter

From figures 6.6 and 6.9, the proton bubble efficiency could be expected to be maximum from 0 to ~3 keV, and to drop to zero around ~4 keV. Therefore, an efficiency curve that could look (approximately) like figure 6.10 could be expected. Having another look at the Harper parameter, one can find some values that would produce such curves, as shown of figure 6.11. From this, it can therefore be concluded that the Harper parameter could take values of $3/2 \leq b \leq 5/3$; this still has to be confirmed by more measurements.

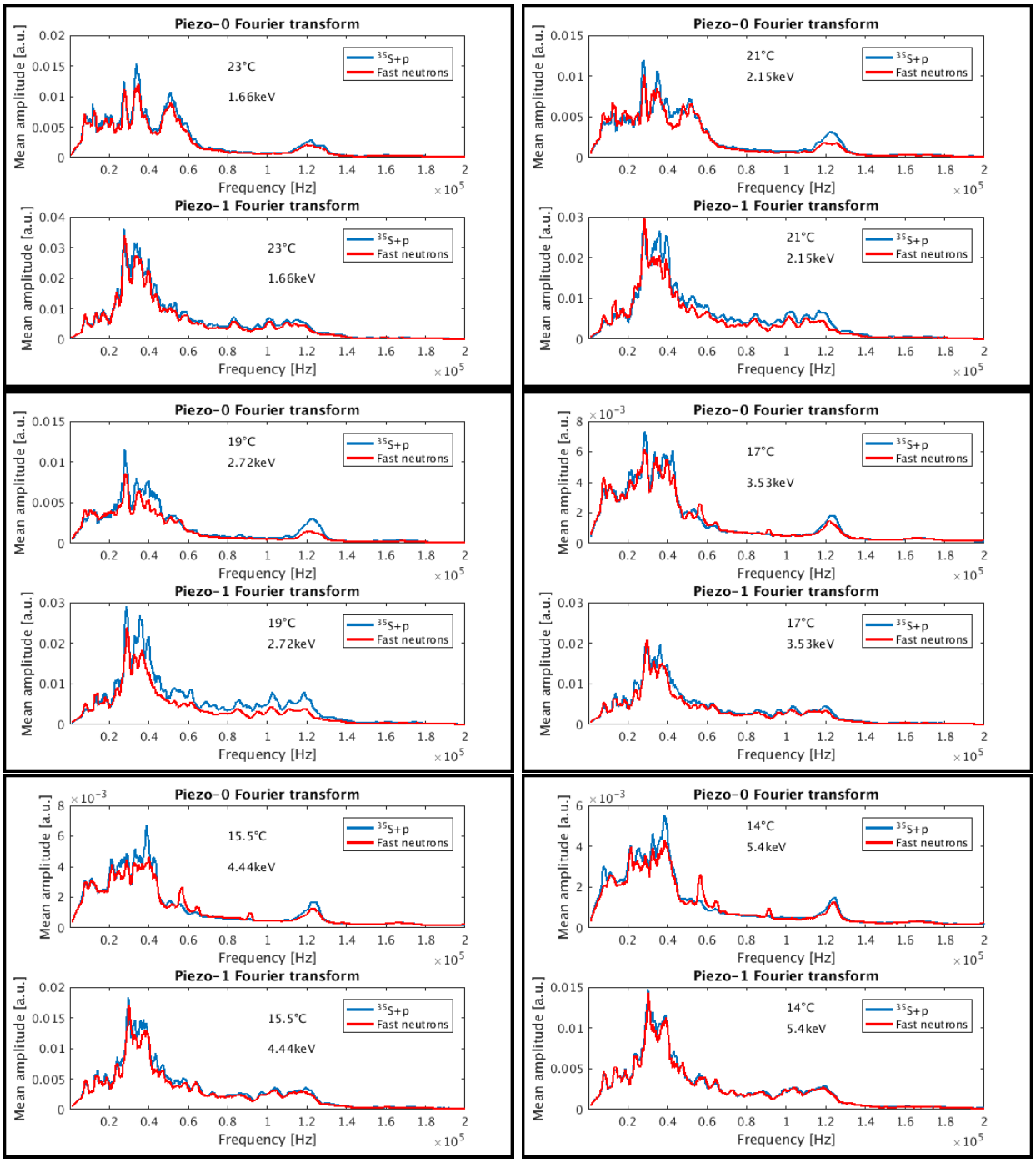

FIG. 6.7. Mean Fast Fourier Transform of ^{35}Cl (n_{th}, p) ^{35}S events (blue) and fast neutron recoil events (red), all at 35 PSI, respectively (from top-left to bottom-right) for 1.66 keV (23°C), 2.15 keV (21°C), 2.72 keV (19°C), 3.53 keV (17°C), 4.44 keV (15.5°C) and 5.4 keV (14°C). The FFTs for each threshold point are shown for both piezos.

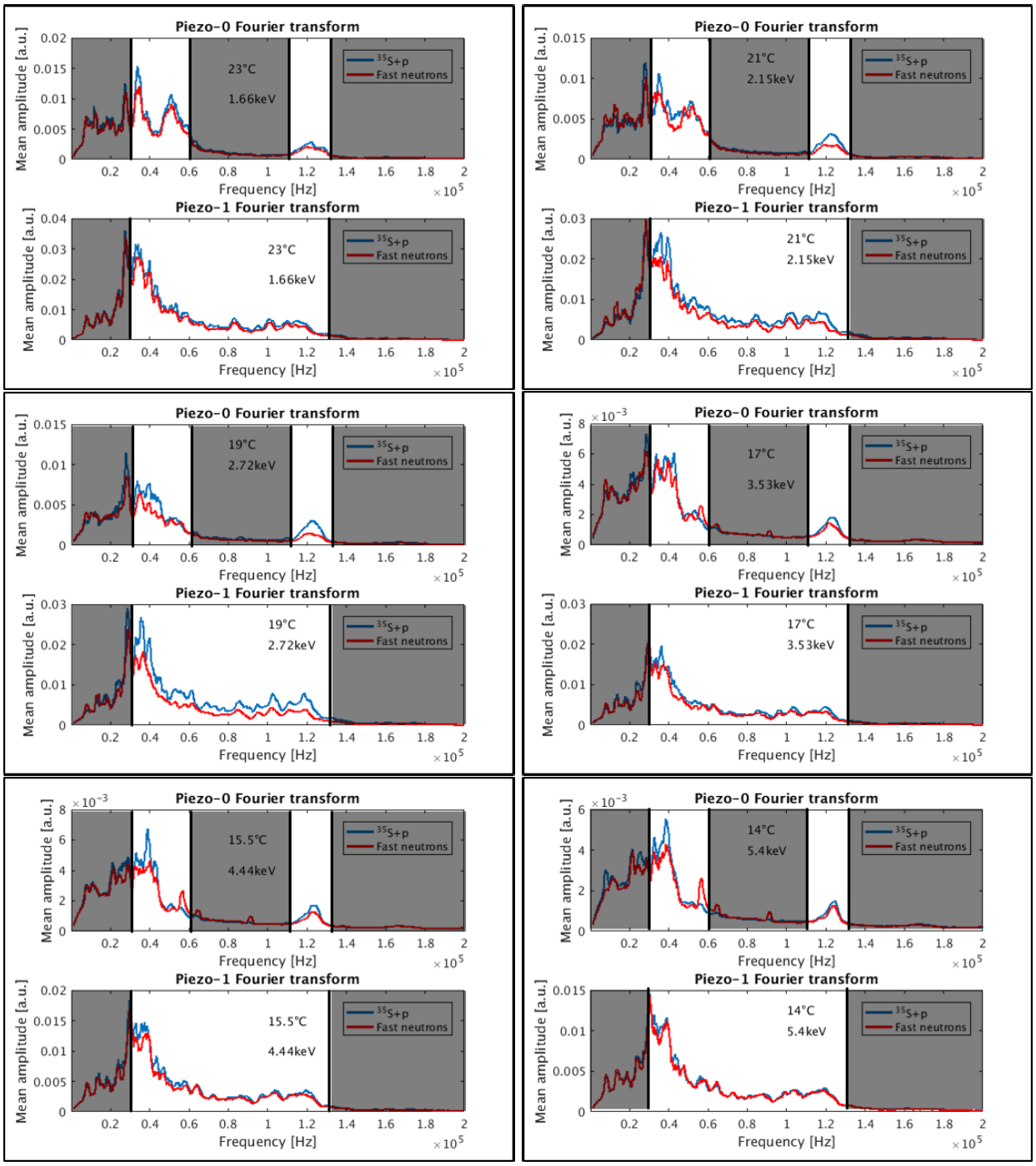

FIG. 6.8. Frequency selections for the mean Fast Fourier Transform of ^{35}Cl (n_{th}, p) ^{35}S events (blue) and fast neutron recoil events (red) of figure 6.7. Dark sections are now not taken into account.

Thus, it was concluded that proton recoils are detectable in PICO detectors, and a more direct approach is now explored by filling PICO-0.1 with $C_2H_2F_4$ and searching for hydrogen nuclei recoils from elastic scattering; results and analysis are presented in the next

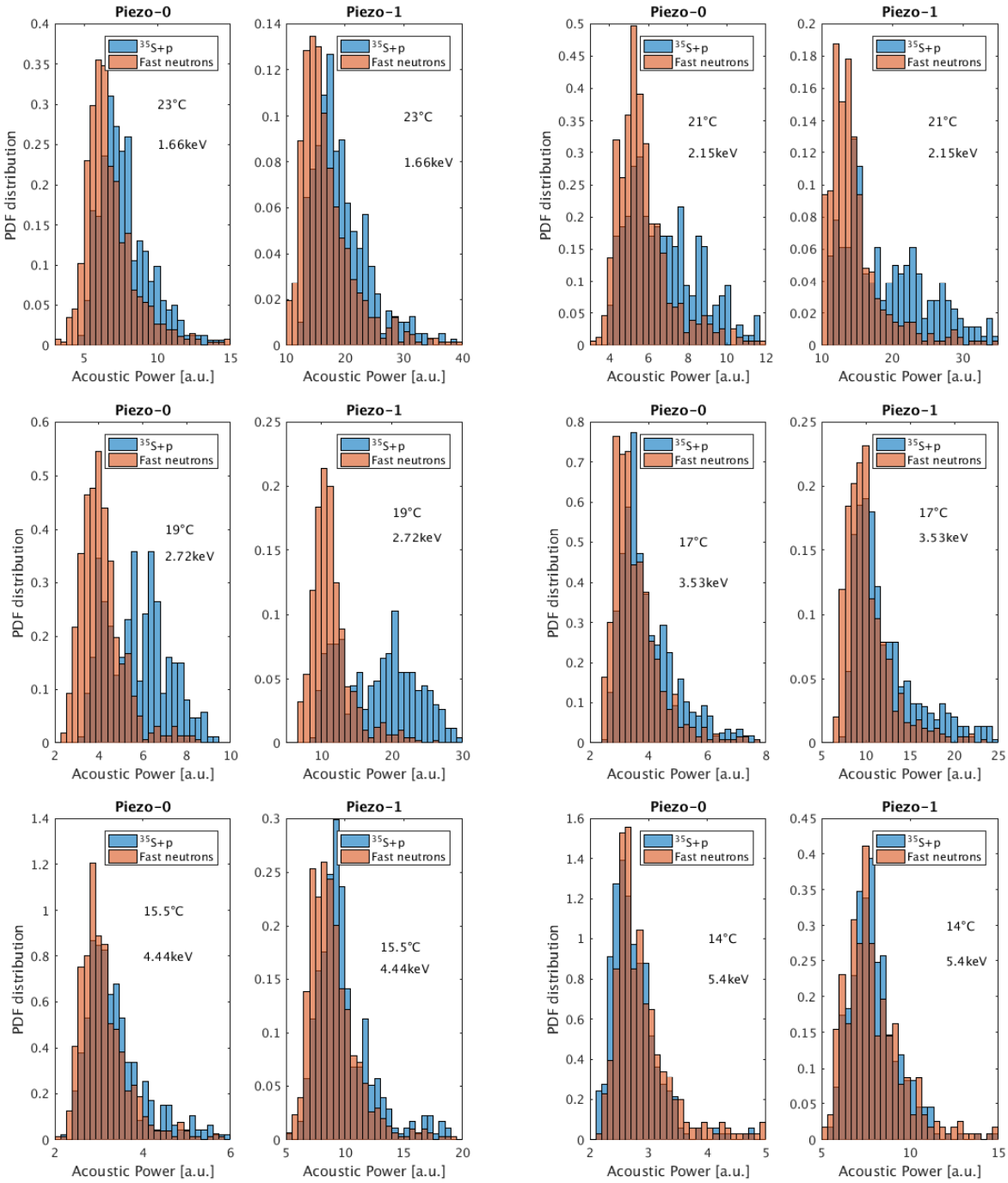

FIG. 6.9. Normalized acoustic power distributions with specific frequency selection (as described in equations 6.1.2, and shown on figure 6.8) for ^{35}Cl (n_{th}, p) ^{35}S events (blue) and fast neutron recoil events (red), all at 35 PSI, respectively (from top-left to bottom-right) for 1.66 keV (23°C), 2.15 keV (21°C), 2.72 keV (19°C), 3.53 keV (17°C), 4.44 keV (15.5°C) and 5.4 keV (14°C). The distributions for each threshold point are shown for both piezos.

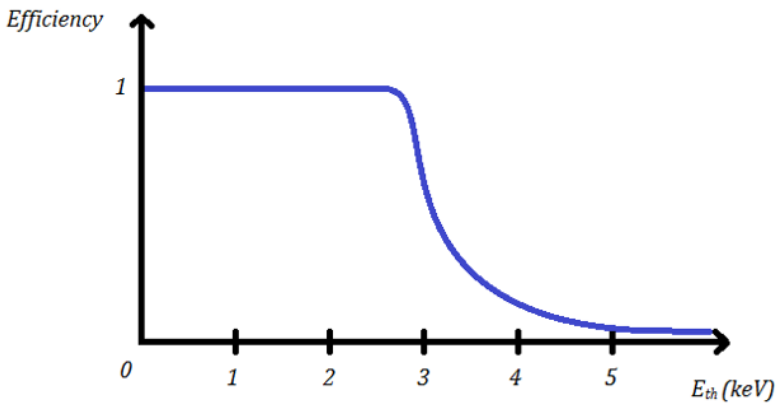

FIG. 6.10. Expected proton bubble efficiency, deduced from acoustics analysis.

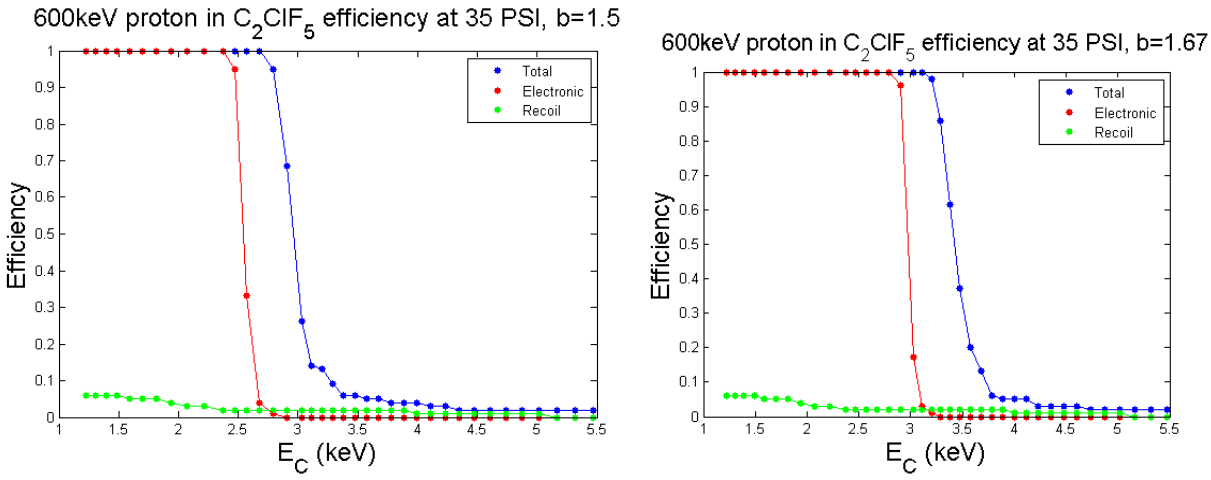

FIG. 6.11. Efficiency curves produced with *SRIM* for 600 keV proton recoils in C_2ClF_5, for $b = 3/2$ (left) and $b = 5/3$ (right). Each efficiency point is calculated with 100 *SRIM* recoil simulations.

section.

6.2. PROTON RECOILS IN $C_2H_2F_4$

Another way to detect proton recoils in PICO detectors is from typical PICO events: nuclear recoils. By using $C_2H_2F_4$ as the active fluid in PICO-0.1, one can search for recoils of hydrogen nuclei (i.e. protons). The next sections describe two ways it was done.

Property	C_3F_8	C_2ClF_5	$C_2H_2F_4$
T_B (°C)	-36.789	-38.942	-26.074
T_C (°C)	71.87	79.79	101.06
$P_{v\ 15°C}$ (PSIA)	95.180	99.596	70.833
$\rho_{l\ 15°C}$ (g/ml)	1.3795	1.3388	1.2434

TAB. 6.1. Thermodynamic properties of C_3F_8, C_2ClF_5 and $C_2H_2F_4$ [61].

6.2.1. $C_2H_2F_4$ thermodynamics

Before any further step, a brief look was taken at the thermodynamic properties of $C_2H_2F_4$, and their usability in bubble chambers. Although $C_2H_2F_4$ is not as thermodynamically close to C_3F_8 as C_2ClF_5, its properties are close enough to be adequate for operation in PICO bubble chambers; table 6.1 compares them to those of C_3F_8 and C_2ClF_5 (already presented in table 5.1), and figure 6.12 shows the $C_2H_2F_4$ vapor pressure as a function of temperature. Comparing figures 6.12 and 5.1, one can conclude that in terms of vapor pressure (a critical property for a fluid in a bubble chamber), $C_2H_2F_4$ is usable for a PICO detector.

6.2.2. 22.8 keV neutrons

First, elastic scattering with 22.8 keV neutrons from an SbBe source was studied, these neutrons being obtained as described in section 5.2.1. In this case, the respective measured activities of the three reactivated antimony sources were 724, 382 and 365 μCi, on October 31st, 2017.

6.2.2.1. *Nuclear recoils*

From the energy spectra of nuclear recoils (eq. 4.4.1), the maximum recoil energies ($\theta = \pi$) for the three atoms of $C_2H_2F_4$ are:

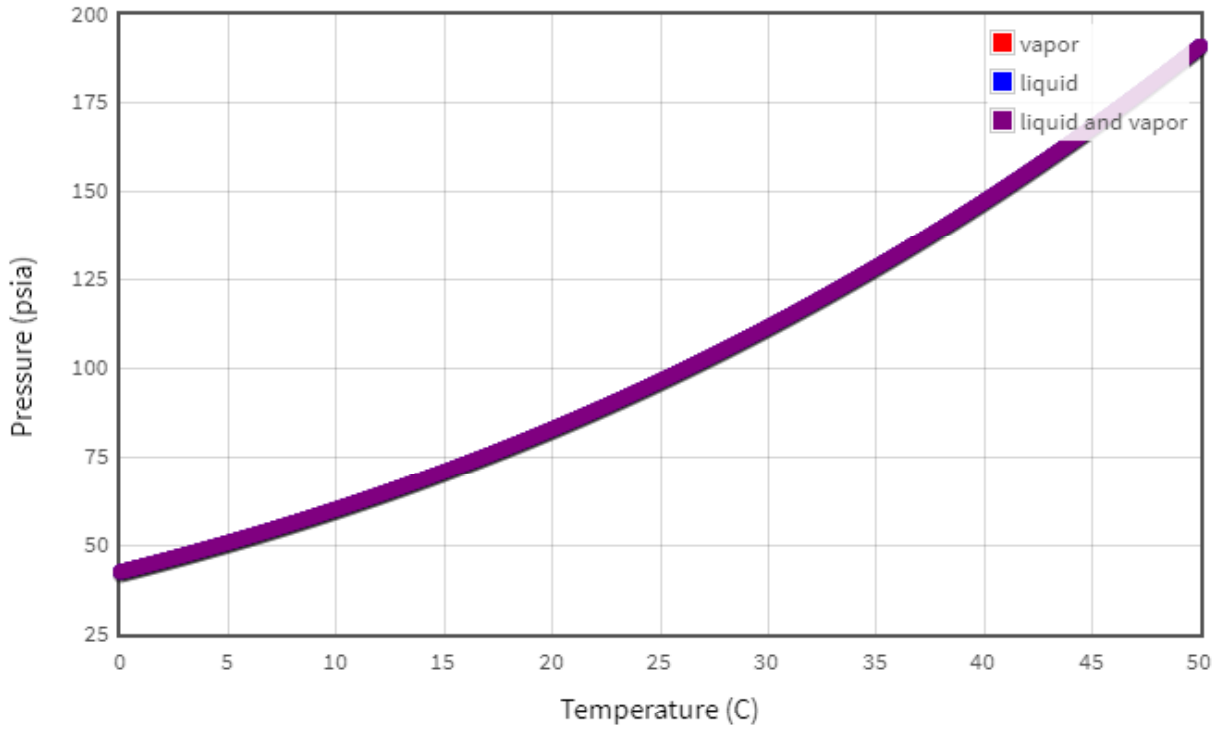

FIG. 6.12. $C_2H_2F_4$ vapor pressure as a function of temperature [61].

$$\begin{aligned} \text{H (A=1)} &: E_{R_{max}} = E_n \\ \text{C (A=12)} &: E_{R_{max}} \approx 0.28 E_n \\ \text{F (A=19)} &: E_{R_{max}} = 0.19 E_n \ . \end{aligned} \tag{6.2.1}$$

Therefore, recoils in the energy range $E_R \in [0.28,1]E_n$ in $C_2H_2F_4$ can only be recoils from hydrogen nuclei, since carbon and fluorine are too heavy to obtain these energies from elastic scattering with a neutron. One can then search for proton recoils in this region of threshold energies. For 22.8 keV neutrons, the maximum recoil energies are:

$$\begin{aligned} \text{H} &: E_{R_{max}} = 22.8 \text{ keV} \\ \text{C} &: E_{R_{max}} \approx 6.38 \text{ keV} \\ \text{F} &: E_{R_{max}} \approx 4.33 \text{ keV} \ , \end{aligned} \tag{6.2.2}$$

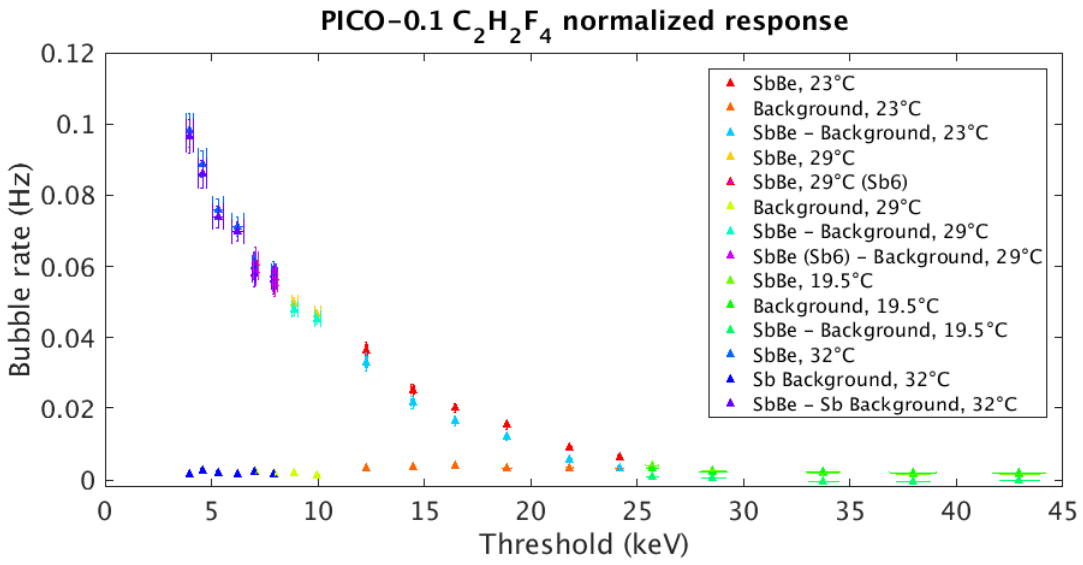

FIG. 6.13. PICO-0.1 response to 22.8 keV neutrons in $C_2H_2F_4$. All data (background and with source) are shown. Data are normalized to source activity.

providing the range $E_R \in [6.38,22.8]$ keV where only proton recoils are allowed.

6.2.2.2. *Data with water in water bath*

The PICO-0.1 response with threshold points exploring the energy range $E_R \in [6.38,22.8]$ keV is shown on figures 6.13 and 6.14. A significant count rate above background is observed in the region of interest, where only proton recoils are allowed; it seems to be a good evidence that proton recoils were detected in $C_2H_2F_4$. However, some interrogations remain: one data point above 22 keV is significantly above background (154 events vs. 75 expected from background, 6.4σ excess), where it shoudn't be allowed; the shape of the curve is hardly explained, as one could have expected a linear rise from 22.8 to 6.38 keV (see section 4.4, specifically figure 4.14, extrapolated to hydrogen recoils) while this is not observed; materials between the neutron source and the active fluid, especially a few centimeters of water, certainly have slowed down the 22.8 keV neutrons to lower energies, therefore shifting down the energy thresholds of each nuclear recoil and changing the meaning of this count rate curve. Data without water in the water bath (detector at room temperature) were therefore taken to seek understanding, and are presented in the next section.

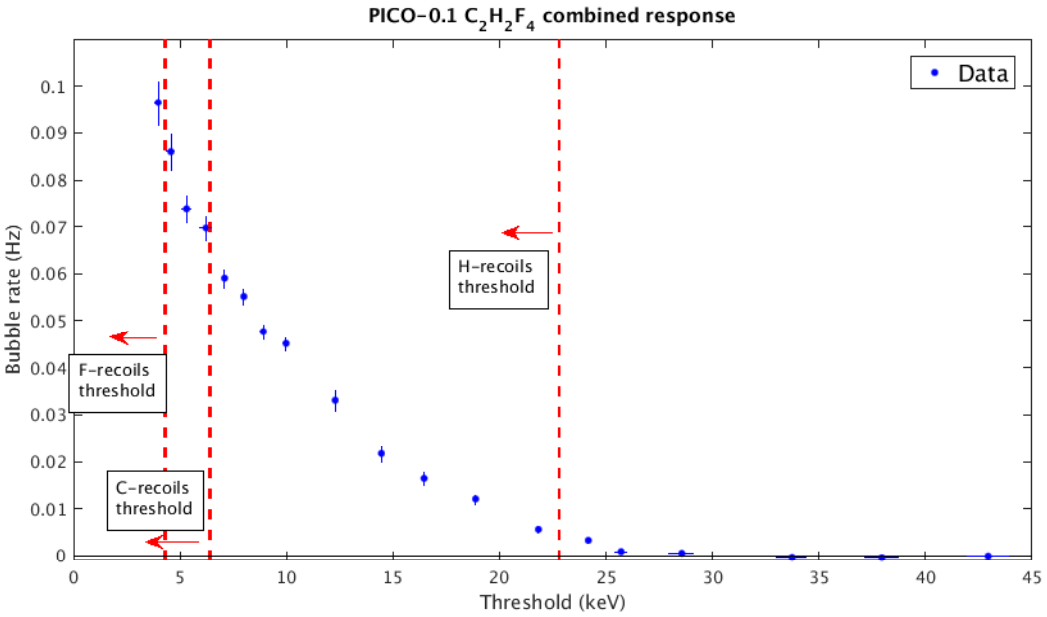

FIG. 6.14. Background-subtracted PICO-0.1 response to 22.8 keV neutrons in $C_2H_2F_4$, with visual markers for the different threshold energies of fluorine, carbon and hydrogen nuclei. Region of interest is $E_{th} \in$ [6.38,22.8] for proton recoil events. Data are normalized to source activity.

6.2.2.3. *Data without water in water bath*

In order to understand better the count rate curve obtained on figure 6.14, data were taken without water in PICO-0.1's water bath, so that 22.8 keV neutrons are less slowed down and absorbed between their emission from the SbBe source and the active fluid. Results are shown on figure 6.15. As expected, a shift in energy is observed between data with water and data without, as neutrons indeed lose energy when passing through water. By comparing the two count rate curves, it was found that neutrons were losing about 6.75 keV in water; figure 6.16 shows the same data, but the data with water in the water bath are manually shifted by 6.75 keV to higher energies. It is now clear that some process other than proton recoils creates events, as four data points above 22 keV now have significant count rates above background. One hypothesis that is emitted is that the small fraction of 378 keV neutrons (see section 5.2.1) creates bubble events; however, it is not understood why they would begin to do so only at about 32 keV. Some

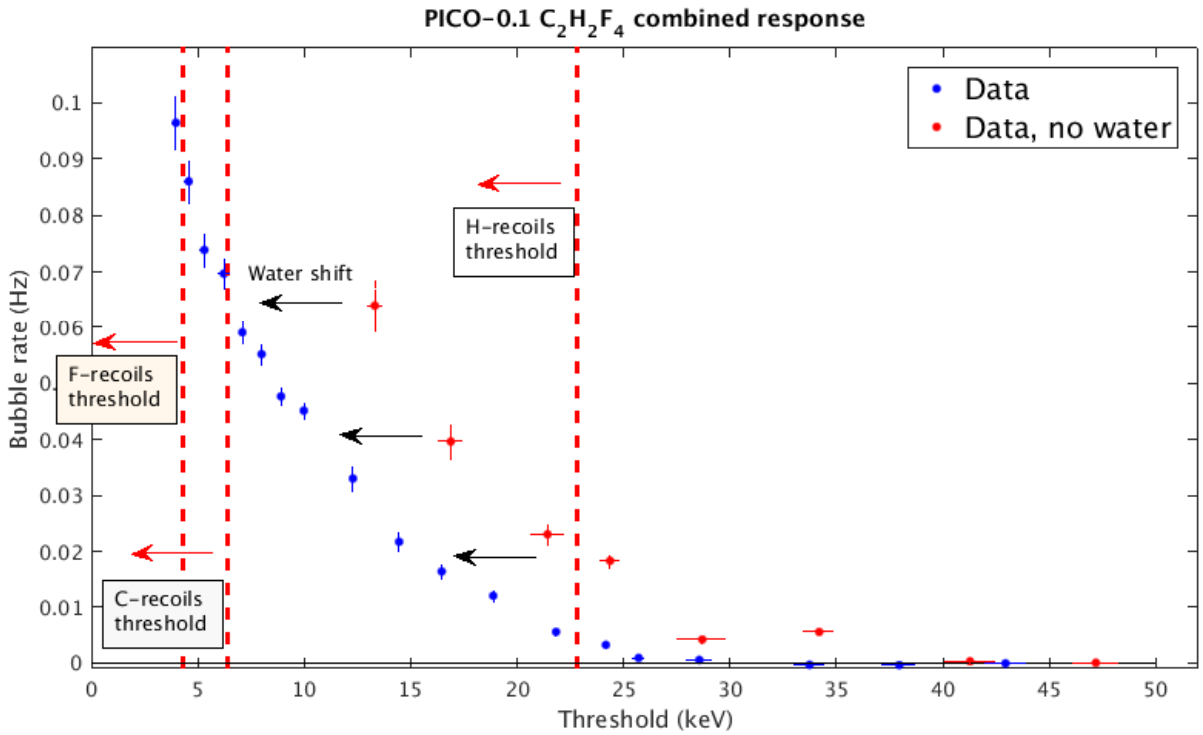

FIG. 6.15. Background-subtracted PICO-0.1 response to 22.8 keV neutrons in $C_2H_2F_4$, with (blue) and without (red) water in the water bath. Data are normalized to source activity.

simulations are therefore needed to explain the behaviour of this count rate curve in $C_2H_2F_4$.

6.2.2.4. *Simulations*

Simulations were carried out by prof. Alan E. Robinson for PICO-0.1 response to a ^{124}SbBe neutron source, including the 3% of 378 keV neutrons, and 1.256 cm of water between the outside of PICO-0.1 jar and the end of the beam tube (between the source and the detector). Figure 6.17 compares the experimental data to the simulations count rate, for all events having at least one bubble. The simulation curve is renormalized to fit the experimental data (simulations were not absolute but accurate on the shape of the curve). Although data do not fit perfectly the simulations, a good agreement is found; simulations including events from neutrons scattering on protons, it is concluded that proton recoils were indeed observed.

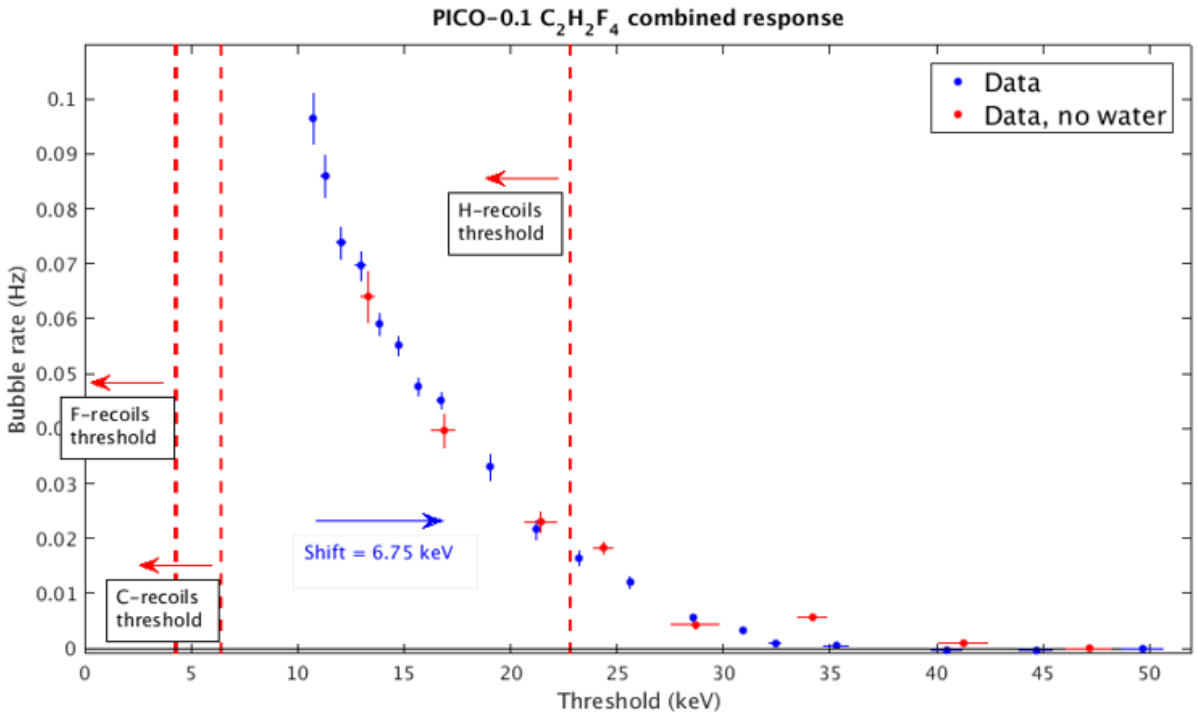

FIG. 6.16. Background-subtracted PICO-0.1 response to 22.8 keV neutrons in $C_2H_2F_4$, with (blue) and without (red) water in the water bath. Data with water are manually shifted by 6.75 kev to match data without water. Data are normalized to source activity.

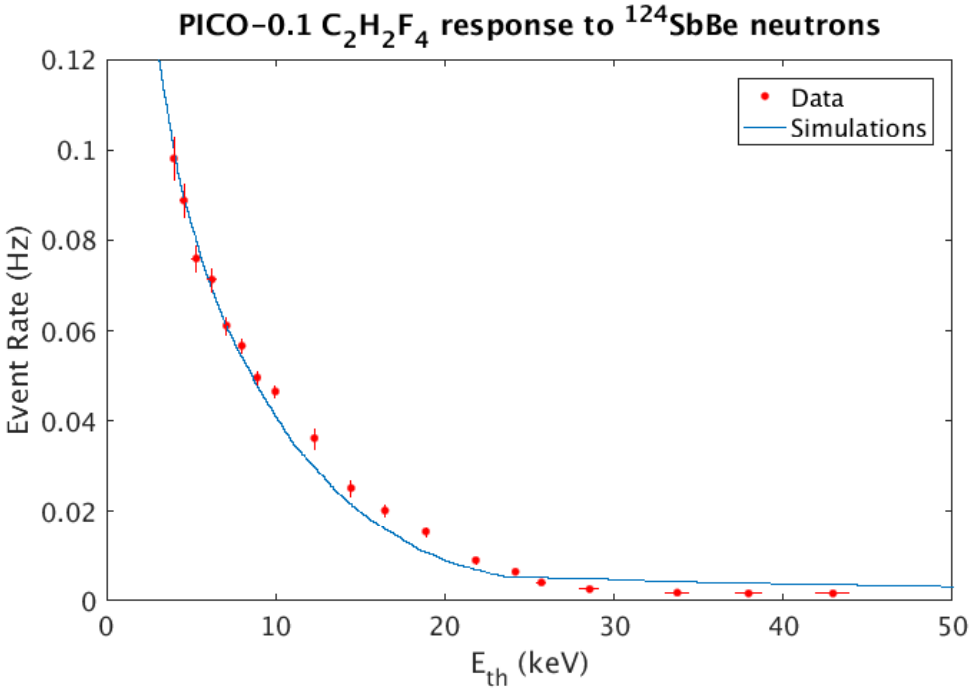

FIG. 6.17. PICO-0.1 response to ^{124}SbBe neutrons in $C_2H_2F_4$, compared to simulations.

6.2.3. Thomson scattering

Next, Thomson scattering on hydrogen nuclei was studied. Thomson scattering is the low-energy limit of Compton scattering, i.e. when electromagnetic radiation scatters on a charged particle of mass (energy) much greater than the energy of the photon. This condition can be written:

$$h\nu \ll mc^2 \ . \tag{6.2.3}$$

In the present case, gamma rays from a ^{24}Na radioactive source was used. ^{24}Na is an unstable isotope of sodium, that can also be produced at the SLOWPOKE facility of Polytechnique Montreal. ^{24}Na decays by a β^- process to ^{24}Mg with a half-life of 14.958 hours, emitting two gamma rays of 1.368 and 2.754 MeV, respectively [68]. Since the proton has a mass of 938 MeV(/c^2), condition 6.2.3 for Thomson scattering is therefore respected. The present source was activated with 474 μCi, at 2:03 PM on May 24$^{\text{th}}$, 2018.

From the Thomson scattering cross section on a particle of mass m and charge q [69]

$$\sigma_T = \frac{8\pi}{3}\left(\frac{q^2}{4\pi\epsilon_0 mc^2}\right)^2 \ , \tag{6.2.4}$$

one can derive the differential count rate for Thomson scattering on protons as a function of the recoil energy E_R in a PICO bubble chamber:

$$\frac{dR}{dE_R} = \frac{3m_pc^2}{8E_\gamma^2}\left(1+\left(1-E_R\frac{m_pc^2}{E_\gamma^2}\right)\right) \tag{6.2.5}$$

where m_p is the mass of the proton and E_γ the photon energy. As described in section 4.4, the detector count rate at a fixed threshold energy is given by the integral of the spectrum above this energy; namely:

$$R = \int_{E_{th}}^{E_{max}} dE_R \tag{6.2.6}$$

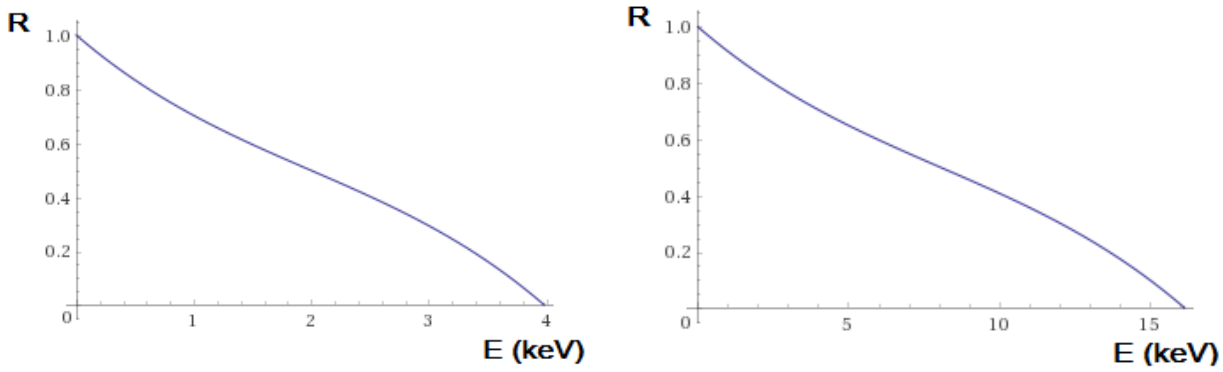

FIG. 6.18. Expected detector response from Thomson scattering, for 1.368 MeV γ (left) and 2.754 MeV γ (right).

where E_{max} is the maximum recoil energy; here $E_{max} = 2E_\gamma^2/m_pc^2$, from kinematics of a collision between a γ and a proton. Integrating equation 6.2.5, one can find the relative (normalized to 1) count rate as a function of the threshold energy:

$$R(E_{th}) = 1 - \frac{3}{4}\frac{m_pc^2}{E_\gamma^2}E_{th} + \frac{3}{8}\left(\frac{m_pc^2}{E_\gamma^2}\right)^2 E_{th}^2 - \frac{1}{8}\left(\frac{m_pc^2}{E_\gamma^2}\right)^3 E_{th}^3 \tag{6.2.7}$$

This expected detector response for γ's of 1.368 and 2.754 MeV is illustrated on figure 6.18; it is observed that the detector response begins (when decreasing in threshold energy) around 4 keV for 1.368 MeV γ's, and around 16 keV for 2.754 MeV γ's; solving eq. 6.2.7 exactly for $R = 0$ (maximum threshold energy), one finds that the detector response begins at 3.96 keV for 1.368 MeV γ's, and at 16.17 keV for 2.754 MeV γ's. One can therefore explore the energy range around 16 keV to study Thomson scattering of 2.754 MeV γ's in $C_2H_2F_4$; this is done in the next section.

6.2.3.1. *Data*

The PICO-0.1 data for the study of Thomson scattering on protons were taken between May 24$^{\text{th}}$ and May 28$^{\text{th}}$, 2018, and are presented on figure 6.19. A count rate significantly above background is observed from 18 keV and below, while at 26 keV the count rate is comparable to the background. However, this does not directly imply the observation of Thomson scattering on protons, particularly because no events are expected above 16

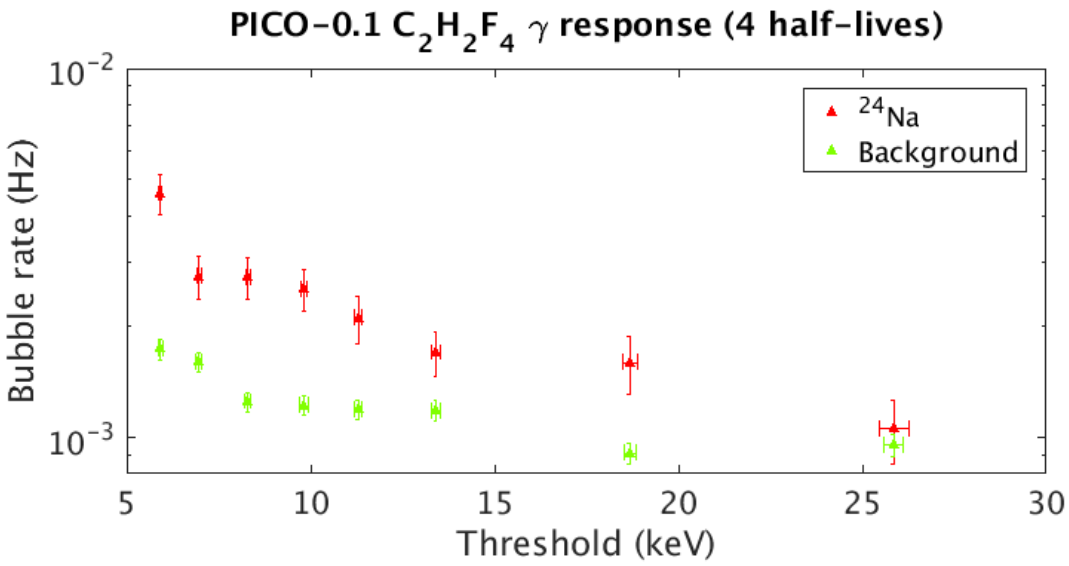

FIG. 6.19. PICO-0.1 response to ^{24}Na gamma rays in $C_2H_2F_4$. Data are not normalized to source activity; threshold points were selected randomly for each event, compensating for the relative effect of the source decaying. Data for four ^{24}Na half-lives are used.

keV; events can occur from neutrons indirectly produced by the gamma source. The most common process that could create neutron events in the detector is the dissociation of deuterium from the absorption of a gamma ray, ejecting a neutron. This can occur in surrounding materials, especially water from the PICO-0.1's water bath, and also from hydrogen in the active fluid itself ($C_2H_2F_4$). Some simulations therefore need to be carried out to estimate the fraction of events that are from Thomson scattering, and from other processes.

6.2.3.2. *Simulations*

Simulations were performed by prof. Alan E. Robinson to determine what fraction of events could come from Thomson scattering on protons. The total expected count rate curve is shown on figure 6.20, and a renormalization to fit the experimental data (to take into account the decaying of the source) are shown on figure 6.21. Although data do not fit

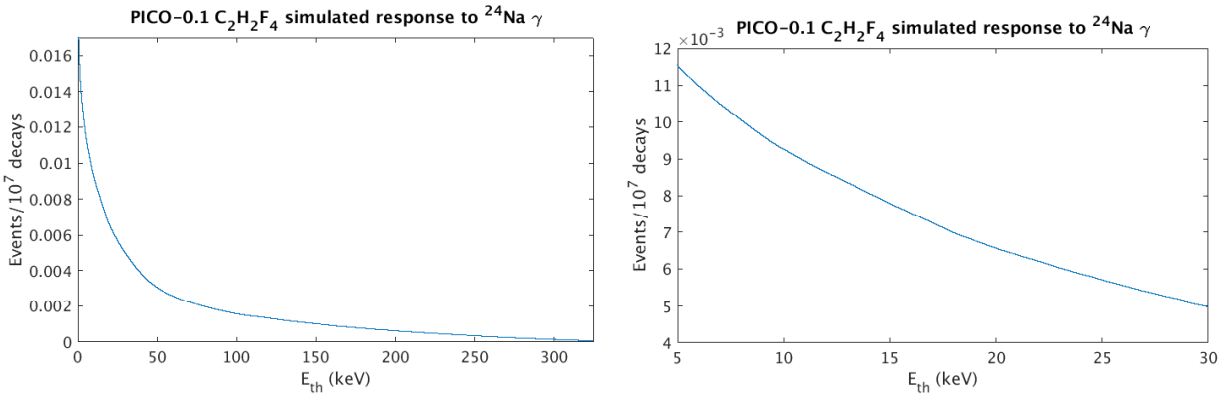

FIG. 6.20. Simulation of PICO-0.1 response to ^{24}Na gamma rays in $C_2H_2F_4$. Complete response (left) and zoom on the region of interest where data were taken (right).

perfectly the simulations, a good agreement is found. Fractions of different types of events were obtained:

- 1.79x10^{-10} events per ^{24}Na decay are expected from a neutron produced inside the freon.
- 9.45x10^{-9} events per ^{24}Na decay, for all threshold energies, are expected from Thomson scattering on protons.
- Rest of events comes from neutrons outside the freon.

Given eq. 6.2.7 for 2.754 MeV γ's (right of figure 6.18) and knowing that 9.45x10^{-9} events per ^{24}Na decay, for all energies (integral of the rate curve) come from Thomson scattering, one can renormalize the expected rate with this number:

$$R_N(E_{th}) = \frac{9.45\text{x}10^{-9}}{\int_0^{16.17} R(E_{th})\ dE_{th}} R(E_{th}) \approx \frac{9.45\text{x}10^{-9}}{8.0834} R(E_{th}) \approx 1.169\text{x}10^{-9} R(E_{th}) \qquad (6.2.8)$$

This renormalized expected rate from Thomson scattering on protons is compared to the total rate obtained from simulations, and is shown on figure 6.22. It is observed that a significant fraction of events is coming from Thomson scattering, suggesting that it was observed in PICO-0.1.

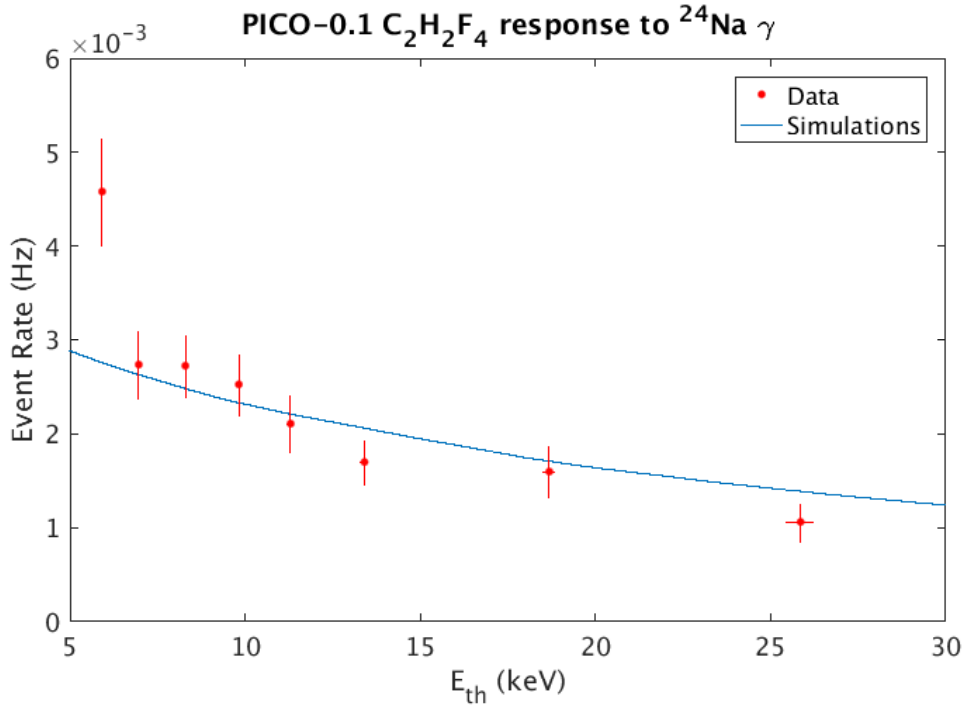

FIG. 6.21. PICO-0.1 response to ^{24}Na gamma rays in $C_2H_2F_4$, data compared to simulations.

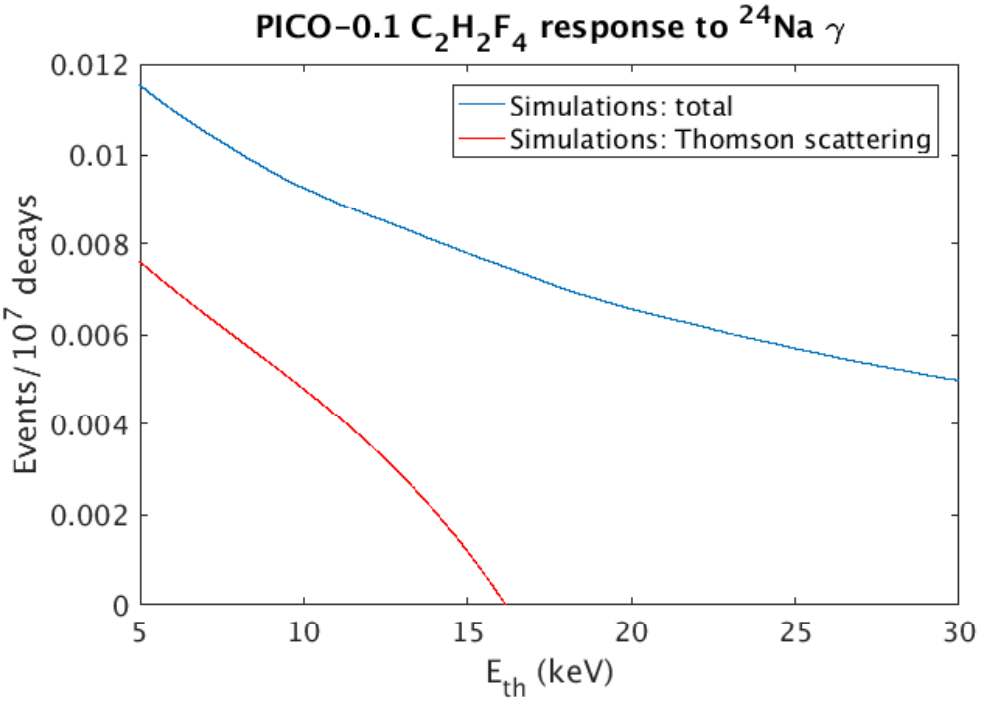

FIG. 6.22. Simulation of PICO-0.1 response to ^{24}Na gamma rays in $C_2H_2F_4$, including the fraction from Thomson scattering

It is therefore concluded that Thomson scattering on protons was likely observed in PICO-0.1.

6.3. Projected limits plot

It has been shown with PICO-0.1 that $C_2H_2F_4$ can be used as the active fluid inside a PICO bubble chamber, and in adequate conditions of operation. Therefore, $C_2H_2F_4$ could potentially be used for a dark matter search run in PICO main detectors, whether during future runs of PICO-40L or even PICO-500. As previously stated, the hydrogen in $C_2H_2F_4$ would largely improve the sensitivity of PICO at low WIMP mass; figure 6.23 presents potential limits that the PICO experiment could obtain with $C_2H_2F_4$ in PICO-40L. These limits were produced assuming 120 live-days (5400 kg-days) of exposure at 43°C and 20 PSIA, for a threshold energy about 1 keV; one can still adjust the temperature in the range 43-45°C, and the pressure between 20 and 40 PSIA (20 PSIA is too low for an operating PICO chamber) to obtain a threshold of 1 keV. These presented limits were calculated by Arthur Plante, a PICO colleague and PhD candidate at University of Montreal.

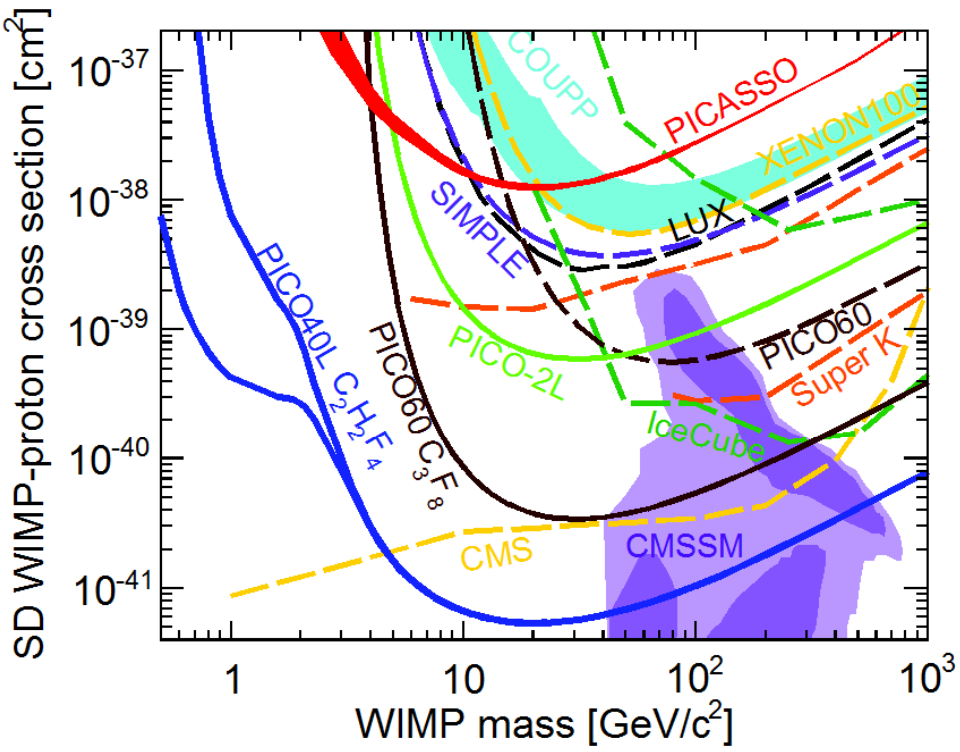

FIG. 6.23. Potential new exclusion limits of the PICO experiment for the search dark matter (blue), using $C_2H_2F_4$ in PICO-40L, with an exposure of 120 live-days (5400 kg-days) at a threshold about 1 keV. Current exclusion limits of PICO are shown in black. The two blue curves are calculated assuming two different hydrogen nucleation efficiencies at 1 keV, as shown on figure 6.24

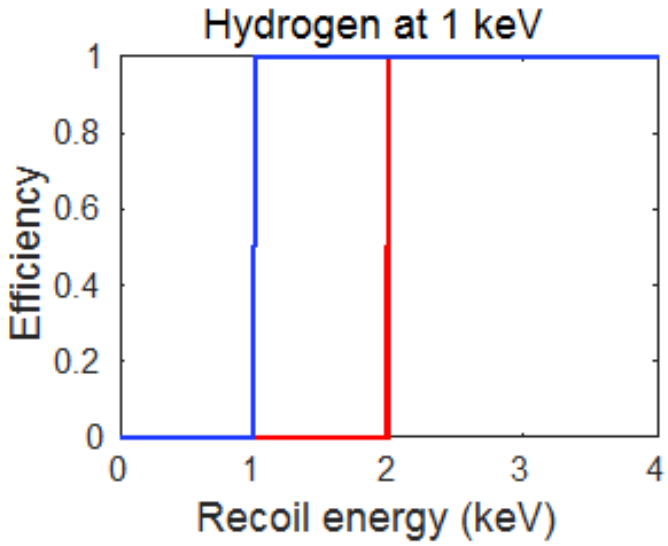

FIG. 6.24. Hydrogen nucleation efficiencies at a 1 keV threshold, as a function of the recoil energy. The blue efficiency generates the lowest limit of the two on figure 6.23, the red efficiency generates the highest limit of the two.

CONCLUSION

A lot of work still has to be done to have definitive evidence of the detection of dark matter. Great amounts of progress are made every year in all kinds of experiments trying to detect it, whether it is about the development of new technologies or a better understanding of the current ones. This general progress obviously includes the efforts of the PICO bubble chamber experiment: not only with its new detector design, but also with a deeper comprehension of its functioning, and of the theory of the physics behind it. The work done in this thesis provided insights on both parts: a better understanding of the theory, as well as experimental evidence of a yet unobserved phenomenon that could lead to new projects for the PICO experiment.

First, chapter 5 presented a study of the Seitz threshold, i.e. the theoretical model to calculate the energy necessary to form a bubble in a bubble chamber. Through the reaction ^{35}Cl (n_{th}, p) ^{35}S in C_2ClF_5, the ^{35}S monoenergetic recoil was studied to precisely understand and characterize the Seitz threshold. Many hypotheses were explored to explain the behaviour observed for this monoenergetic reaction; none of them, represented through simulations, could succeed. Hypotheses were such as: different values of the *Harper parameter* - providing the size of the critical length in which the energy has to be deposited to form a bubble; a lower surface tension than previously assumed for spherical bubbles; energy loss through heat dissipation during the growth of the bubbles; a normal distribution - instead of a fixed value - for the critical radius necessary for a bubble not to collapse on itself; and a combination of the two last hypotheses. Another approach was then explored: revisiting the Seitz threshold itself. By assuming an intrinsic resolution -

with a mean and a width - to the Seitz threshold, one could explain the behaviour of the ^{35}S monoenergetic recoil data, as well as a few more monoenergetic calibrations; a trend could be deduced for the function resolution: a resolution of about 10% was found for all cases. One could therefore describe the Seitz threshold with an intrinsic resolution and an energy shift. However, more calibrations need to be performed to confirm the observed trend, as well as to define a relation for the threshold shift and understand the mechanism behind it.

Second, proton recoils in PICO detectors were observed and described for the first time, in chapter 6. They were first observed by the acoustics analysis of the same reaction studied in chapter 5, i.e. ^{35}Cl (n_{th}, p) ^{35}S. This reaction produces a 600 keV monoenergetic proton recoil in the detector, that could be observed by comparing the acoustic power of such events with events containing only nuclear recoils; events with protons were acoustically more powerful, assuring that protons produce their own bubbles. They were then observed in a second manner by studying nuclear recoils in $C_2H_2F_4$. From elastic scattering with neutrons, only the threshold energy range $E_R \in [0.28,1]E_n$ allows for hydrogen nucleus recoils, i.e. proton recoils; they were indeed observed in this region. Furthermore, Thomson scattering on protons from 2.754 MeV gammas allows bubble events below 16 keV. Good evidence was found that this kind of recoil was observed as well.

In summary, the work done in this thesis provided new insights on the understanding of the Seitz threshold, and brought evidence of the detection of proton recoils in a PICO detector; both of these subjects can be useful for the future of the PICO experiment. The characterization of the Seitz threshold of chapter 5 has the potential to be extended by studying more monoenergetic calibrations, and eventually could help understand more precisely the Seitz threshold. On the other hand, the detection of proton recoils and the demonstration of usability of $C_2H_2F_4$ as the active fluid in a PICO detector is a tangible progress and has direct influence on the future of dark matter search with PICO: calibrating PICO detectors to proton recoils will improve significantly their sensitivity at low WIMP mass, especially by using $C_2H_2F_4$ as the active fluid for the search of dark matter.

BIBLIOGRAPHY

[1] HARTLE, James B. *Gravity: An introduction to Eistein's general relativity.* Addison Wesley, 2003.

[2] The Planck Collaboration. *Planck 2015 results. XIII. Cosmological parameters.* Astronomy & Astrophysics **594** (2016).
arxiv:1502.01589

[3] KAPTEYN, Jacobus C. *First attempt at a theory of the arrangement and motion of the sidereal system.* Astrophysical Journal **55** (1922).

[4] OORT, Jan H. *The force exerted by the stellar system in the direction perpendicular to the galactic plane and some related problems.* Bulletin of the Astronomical Institutes of the Netherlands, **6** (1932).

[5] ZWICKY, Fritz. *The redshift of extragalactic nebulae.* Helvetica Physica Acta **6** (1933).

[6] RUBIN, Vera and FORD, W. Kent, Jr. *Rotation of the Andromeda Nebula from a Spectroscopic Survey of Emission Regions.* The Astrophyscal Journal **159** (1970).

[7] Universe Today. *Astronomy without a telescope - Could dark matter not matter?.* `https://www.universetoday.com/91520/astronomy-without-a-telescope-could-dark-matter-not-matter/`

[8] CLOWE, D., GONZALEZ, A. and MARKEVITCH, M. *Weak-Lensing Mass Reconstruction of the Interacting Cluster 1E 0657–558: Direct Evidence for the Existence of Dark Matter.* The Astrophysical Journal **604** (2004).
arxiv:0312273

[9] CHANDRA X-Ray Observatory. `http://chandra.harvard.edu/photo/2006/1e0657/more.html`

[10] FIXSEN, D.J. *The Temperature of the Cosmic Microwave Background.* The Astrophysical Journal **707** (2009).
arxiv:0911.1955

[11] European Space Agency. *Planck reveals an almost perfect universe*, 2013. http://www.esa.int/Our_Activities/Space_Science/Planck/Planck_reveals_an_almost_perfect_Universe

[12] BAMBI, C. and DOLGOV, A.D. *Introduction to Particle Cosmology : The Standard Model of Cosmology and its Open Problems* (eBook). Springer eBooks, 2016.

[13] PECCEI, R.D. *The Strong CP Problem and Axions*, 2006.
arxiv:0607268

[14] SPERGEL, D.N. *et al. Wilkinson Microwave Anisotropy Probe (WMAP) Three Year Observations: Implications for Cosmology*. The Astrophysical Journal Supplement Series **170** (2007).
arxiv:0603449

[15] BERENJI, B., GASKINS, J. and MEYER, M. *Constraints on Axions and Axionlike Particles from Fermi Large Area Telescope Observations of Neutron Stars*. Physical Review D **93**, 045019 (2016).
arxiv:1602.00091

[16] THOMSON, M. *Modern Particle Physics*. Cambridge University Press, 2013.

[17] MERLE, A. *Sterile Neutrino Dark Matter* (eBook). Morgan & Claypool Publishers, 2017. http://iopscience.iop.org/book/978-1-6817-4481-0.pdf

[18] The MiniBooNE Collaboration. *Observation of a Significant Excess of Electron-Like Events in the MiniBooNE Short-Baseline Neutrino Experiment*, 2018.
arxiv:1805.12028

[19] Particle Data Group. *110. Supersymmetry, Part II (Experiment)*, 2017. http://pdg.lbl.gov/2018/reviews/rpp2018-rev-susy-2-experiment.pdf

[20] TOVEY, D.R. *et al. A new model-independent method for extracting spin-dependent cross section limits from dark matter searches*. Physics Letters B **488** (2000).

[21] The PICO Experiment. http://www.picoexperiment.com/

[22] The MOSCAB Collaboration. *MOSCAB: A geyser-concept bubble chamber to be used in a dark matter search*, 2017.
arxiv:1708.00101

[23] The SIMPLE Collaboration. *The SIMPLE Phase II Dark Matter Search*, 2014.
arxiv:1404.4309

[24] Super Cryogenic Dark Matter Search. http://cdms.berkeley.edu/

[25] SNOLAB. https://www.snolab.ca/

[26] ARAMAKI, Tsuguo. *SuperCDMS Detector Performance And Early Science From Cute*, Identification of Dark Matter, 2018.

[27] New Experiments With Spheres-Gas. https://news-g.org/

[28] The XENON Dark Matter Project. http://xenon.astro.columbia.edu/index.html

[29] The Large Underground Xenon Experiment. http://luxdarkmatter.org/

[30] The DarkSide Collaboration. *The DarkSide Experiment: Present Status and Future*. J. Phys.: Conf. Ser. **798**, 012109 (2017).

[31] Particle and Astrophysical Xenon Experiments. https://pandax.sjtu.edu.cn/

[32] The DAMA Project. http://people.roma2.infn.it/~dama/web/home.html

[33] Dark matter Experiment using Argon Pulse-shape discrimination. http://deap3600.ca/

[34] The MiniCLEAN Collaboration. *MiniCLEAN Dark Matter Experiment*, 2017.
arxiv:1711.02117

[35] GASKINS, Jennifer M., *A review of indirect searches for particle dark matter*. Contempory Physics **57:4**, 496-525 (2016).
arxiv:1604.00014

[36] The Fermi Large Area Telescope. http://www-glast.stanford.edu/

[37] The High Energy Steroscopic System. https://www.mpi-hd.mpg.de/hfm/HESS/

[38] Very Energetic Radiation Imaging Telescope Array System. https://veritas.sao.arizona.edu/

[39] IceCube Neutrino Observatory. https://icecube.wisc.edu

[40] ANTARES. http://antares.in2p3.fr/

[41] Super-Kamiokande. http://www-sk.icrr.u-tokyo.ac.jp/sk/index-e.html

[42] A Payload for Antimatter Matter Exploration and Light-nuclei Astrophysics. http://pamela.roma2.infn.it/index.php

[43] The Alpha Magnetic Spectrometer Experiment. http://www.ams02.org/

[44] CERN. *The Large Hadron Collider*. https://home.cern/topics/large-hadron-collider

[45] ATLAS Experiment at CERN. https://atlas.cern/

[46] Compact Muon Solenoid experiment at CERN's LHC. http://cms.web.cern.ch/news/what-cms

[47] A Large Ion Collider Experiment. http://aliceinfo.cern.ch/Public/Welcome.html

[48] LHCb Collaboration. http://lhcb.web.cern.ch/lhcb/

[49] The PICASSO Experiment. http://www.picassoexperiment.ca/

[50] The COUPP Experiment. http://www-coupp.fnal.gov/

[51] GLASER, Donald A. *Some Effects of Ionizing Radiation on the Formation of Bubbles in Liquids*. Phys. Rev. **87**, 665 (1952).

[52] WIKIPEDIA. *Bubble Chamber*. https://en.wikipedia.org/wiki/Bubble_chamber

[53] CERN. *The decay of a lambda particle in the 32 cm hydrogen bubble chamber*. https://cds.cern.ch/record/39474

[54] PICO Collaboration. *Dark Matter Search Results from the PICO-2L C_3F_8 Bubble Chamber*. Physical Review Letters **114**, 231302 (2015).
arxiv:1503.00008

[55] PICO Collaboration. *Improved dark matter search results from PICO-2L Run 2*. Physical Review D **93**, 061101(R) (2016).
arxiv:1601.03729

[56] PICO Collaboration. *Dark matter search results from the PICO-60 CF_3I bubble chamber*. Physical Review D **93**, 052014 (2016).
arxiv:1510.07754

[57] PICO Collaboration. *Dark Matter Search Results from the PICO-60 C3F8 Bubble Chamber*. Physical Review Letters **118**, 251301 (2017).
arxiv:1702.07666

[58] GIROUX, Guillaume. *PICO-60 Moriond 2017*, COUPP-doc-2171-v2. https://coupp-docdb.fnal.gov/cgi-bin/private/ShowDocument?docid=2171

[59] SEITZ, Frederick. *On the Theory of the Bubble Chamber*. Physics of Fluids **1**, 2 (1958).

[60] ARCHAMBAULT, S. *et al*. *New Insights into Particle Detection with Superheated Liquids*. New J. Phys. **13**, 043006 (2011).
arxiv:1011.4553

[61] National Institute of Standards and Technology. *NIST Chemistry Webbook*, SRD 69. https://webbook.nist.gov/

[62] HARPER, M. J. and RICH, J. C., Nucl Inst. and Meth. A336 (1993) 220.

[63] BARNABÉ-HEIDER, M. *et al* (PICASSO Collaboration), Nucl. Inst. and Meth. A555 (2005) 184.

[64] LOVAS, Rezső G. *Handbook of Nuclear Chemistry*. Springer Science & Business Media, 2003.

[65] Polytechnique Montreal. *SLOWPOKE*. http://www.polymtl.ca/phys/en/slowpoke

[66] Nuclear Power. *Sb-Be Source – Antimony-Beryllium Source.* https://www.nuclear-power.net/nuclear-power/reactor-physics/reactor-dynamics/subcritical-multiplication/source-neutrons-and-external-source-of-neutrons/sb-be-source-antimony-beryllium-source/?pdf=18180

[67] DENZEL, P., DIEMAND, J. and ANGÉLIL, R. *Molecular dynamics simulations of bubble nucleation in dark matter detectors*, 2016.
arxiv:1601.07390

[68] Laboratoire National Henri Becquerel. $^{24}_{11}Na_{13}$. http://www.nucleide.org/DDEP_WG/Nuclides/Na-24_tables.pdf

[69] The University of Texas at Austin. *Thomson scattering.* https://farside.ph.utexas.edu/teaching/jk1/lectures/node107.html

Appendix A

PICO-60 C_3F_8 PAPER

Dark Matter Search Results from the PICO-60 C_3F_8 Bubble Chamber

C. Amole,[1] M. Ardid,[2] I. J. Arnquist,[3] D. M. Asner,[3] D. Baxter,[4,5,*] E. Behnke,[6] P. Bhattacharjee,[7] H. Borsodi,[6] M. Bou-Cabo,[2] P. Campion,[8] G. Cao,[1] C. J. Chen,[4] U. Chowdhury,[1] K. Clark,[9,10] J. I. Collar,[11] P. S. Cooper,[5] M. Crisler,[5,3] G. Crowder,[1] C. E. Dahl,[4,5] M. Das,[7] S. Fallows,[12] J. Farine,[9] I. Felis,[2] R. Filgas,[13] F. Girard,[9,14] G. Giroux,[1,†] J. Hall,[3] O. Harris,[6,15] E. W. Hoppe,[3] M. Jin,[4] C. B. Krauss,[12] M. Laurin,[14] I. Lawson,[9,10] A. Leblanc,[9] I. Levine,[6] W. H. Lippincott,[5] F. Mamedov,[13] D. Maurya,[16] P. Mitra,[12] T. Nania,[6] R. Neilson,[8] A. J. Noble,[1] S. Olson,[1] A. Ortega,[11] A. Plante,[14] R. Podviyanuk,[9] S. Priya,[16] A. E. Robinson,[5] A. Roeder,[6] R. Rucinski,[5] O. Scallon,[9] S. Seth,[7] A. Sonnenschein,[5] N. Starinski,[14] I. Štekl,[13] F. Tardif,[14] E. Vázquez-Jáuregui,[17,9] J. Wells,[6] U. Wichoski,[9] Y. Yan,[16] V. Zacek,[14] and J. Zhang[4]

(PICO Collaboration)

[1]*Department of Physics, Queen's University, Kingston K7L 3N6, Canada*
[2]*Departament de Física Aplicada, IGIC—Universitat Politècnica de València, Gandia 46730 Spain*
[3]*Pacific Northwest National Laboratory, Richland, Washington 99354, USA*
[4]*Department of Physics and Astronomy, Northwestern University, Evanston, Illinois 60208, USA*
[5]*Fermi National Accelerator Laboratory, Batavia, Illinois 60510, USA*
[6]*Department of Physics, Indiana University South Bend, South Bend, Indiana 46634, USA*
[7]*Astroparticle Physics and Cosmology Division, Saha Institute of Nuclear Physics, Kolkata 700064, India*
[8]*Department of Physics, Drexel University, Philadelphia, Pennsylvania 19104, USA*
[9]*Department of Physics, Laurentian University, Sudbury P3E 2C6, Canada*
[10]*SNOLAB, Lively, Ontario P3Y 1N2, Canada*
[11]*Enrico Fermi Institute, KICP and Department of Physics, University of Chicago, Chicago, Illinois 60637, USA*
[12]*Department of Physics, University of Alberta, Edmonton T6G 2E1, Canada*
[13]*Institute of Experimental and Applied Physics, Czech Technical University in Prague, Prague, Cz-12800, Czech Republic*
[14]*Département de Physique, Université de Montréal, Montréal H3C 3J7, Canada*
[15]*Northeastern Illinois University, Chicago, Illinois 60625, USA*
[16]*Bio-Inspired Materials and Devices Laboratory (BMDL), Center for Energy Harvesting Material and Systems (CEHMS), Virginia Tech, Blacksburg, Virginia 24061, USA*
[17]*Instituto de Física, Universidad Nacional Autónoma de México, México D. F. 01000, Mexico*

(Received 9 March 2017; published 23 June 2017)

New results are reported from the operation of the PICO-60 dark matter detector, a bubble chamber filled with 52 kg of C_3F_8 located in the SNOLAB underground laboratory. As in previous PICO bubble chambers, PICO-60 C_3F_8 exhibits excellent electron recoil and alpha decay rejection, and the observed multiple-scattering neutron rate indicates a single-scatter neutron background of less than one event per month. A blind analysis of an efficiency-corrected 1167-kg day exposure at a 3.3-keV thermodynamic threshold reveals no single-scattering nuclear recoil candidates, consistent with the predicted background. These results set the most stringent direct-detection constraint to date on the weakly interacting massive particle (WIMP)-proton spin-dependent cross section at 3.4×10^{-41} cm^2 for a 30-GeV c^{-2} WIMP, more than 1 order of magnitude improvement from previous PICO results.

DOI: 10.1103/PhysRevLett.118.251301

The evidence for nonbaryonic dark matter in the Galactic halo is compelling [1,2]. Many classes of theory, including supersymmetric extensions to the standard model, provide promising dark matter candidates in the form of nonrelativistic, weakly interacting, massive particles (WIMPs) [3]. The search for WIMPs is challenging due to the predicted small WIMP-nucleon scattering cross section and nuclear recoil energies in the range of 1 to 100 keV. Low thresholds, large exposures, and background suppression are therefore critical to obtain sufficient sensitivity. As the nature of the WIMP-nucleon interaction is unknown, explorations in both the spin-dependent (SD) and spin-independent (SI) couplings are essential [4–6].

The PICO Collaboration searches for WIMPs using superheated bubble chambers operated in thermodynamic conditions at which they are virtually insensitive to gamma or beta radiation. Further background suppression is achieved through the measurement of the bubble's acoustic emission, allowing for discrimination between signals from alpha decays and those from nuclear recoils [7]. Superheated detectors filled with fluorine-rich liquids have consistently provided the strongest constraints to

 © 2017 American Physical Society

spin-dependent WIMP-proton interactions [8–15]. Our largest bubble chamber to date, PICO-60, was recently filled with a 52.2 ± 0.5 kg C_3F_8 target, and operated at SNOLAB in Sudbury, Ontario, Canada. Here, we report results from the first run of PICO-60 with C_3F_8, with an efficiency-corrected dark matter exposure of 1167 kg day, taken between November 2016 and January 2017.

The PICO Collaboration previously reported the observation of anomalous background events in dark matter search data with the 2-L PICO-2L C_3F_8 [8] and the 18-L PICO-60 CF_3I [10] bubble chambers. Improvements in fluid handling and bubble chamber operation eliminated this anomalous background in a second run of the PICO-2L detector [9]. A leading hypothesis for the cause of these background events is bubble nucleation due to surface tension effects introduced by the contamination of the active target with particulate matter and water droplets [16]. The PICO-60 detector was recommissioned following a rigorous cleaning procedure targeting particulate contamination. Every component was cleaned to MIL-STD-1246 Level 50 [17] prior to assembly, and samples of the water buffer were taken using an *in situ* filtration system during commissioning to monitor particulate injection. A final measurement after C_3F_8 distillation confirmed that the total assembly met MIL-STD-1246 Level 100, after which the inner volume was closed.

The PICO-60 apparatus was described in Ref. [10], and here we restrict ourselves to describing subsequent improvements and changes. A new seal design was deployed between the silica jar and the stainless steel bellows to minimize particulate generation, replacing the gold wire seal described in Ref. [10] with a nonexpanded virgin polytetrafluoroethylene gasket. The C_3F_8 target does not require the addition of chemicals to remove free ions, unlike CF_3I. While the same water tank is used, a new chiller system holds the temperature in the water tank uniform to approximately 0.1 °C. The target volume was more than doubled, requiring a corresponding increase from two to four cameras (in two vertical columns). Eight piezoelectric acoustic transducers identical to those used in Ref. [9] were attached, evenly spaced around the outside of the silica jar, using a spring loaded high-density polyethylene ring. Five sensors failed during commissioning, leaving three operable sensors for the duration of the experiment.

The chamber expansion cycle is similar to that employed in the previous run [10]. First, the chamber pressure is lowered to a predetermined point, superheating the C_3F_8 active liquid and putting our detector in a live, or expanded, state. Energy deposition within the superheated liquid will nucleate a phase change that can lead to a macroscopic gas bubble, or event. The primary trigger uses the change in entropy between two consecutive camera images [18] to detect the appearance of a gas bubble in the chamber. A trigger is also sent if a rise in pressure is detected or when the chamber has been expanded for 2000 s. Following a trigger, the hydraulic system initiates a fast compression, raising the pressure above 150 psia in roughly 100 ms. The chamber begins a new expansion after a compressed dead time of 100 s. A long compression of 600 s is imposed on every tenth compression or after a pressure-rise trigger. Of the 44.6 days of detector operation during the WIMP search data set, the chamber was expanded (live) for 34.3 days after the compressed dead time is removed.

The WIMP search data set was taken at 30.2 ± 0.3 psi and 13.9 ± 0.1 °C. The threshold is calculated from these thermodynamic conditions using Eq. (2) of Ref. [10] to be 3.29 ± 0.09 keV. There is an additional 0.2 keV uncertainty in the threshold due to the thermodynamic properties of C_3F_8 taken from Ref. [19]. As discussed in Refs. [8] and [10], the nuclear recoil threshold is not a step function at the calculated thermodynamic threshold due to energy losses that escape the region of bubble formation. *In situ* nuclear and electronic recoil calibrations were performed by exposing the chamber to AmBe and ^{252}Cf neutron sources and a ^{133}Ba gamma source both before and after the WIMP search run. Prephysics background data were taken during commissioning to measure the alpha backgrounds due to ^{222}Rn chain decays which, event by event, are indistinguishable from nuclear recoils except in acoustic response. For the WIMP search run, we performed a blind analysis by masking the acoustic information that allows the discrimination between alpha decays and nuclear recoils, effectively salting our WIMP search data with single bulk bubbles. This information was processed only after cuts and efficiencies for single bulk nuclear recoil candidates were set, using source calibrations and prephysics background data.

For the WIMP search data set, periods of unstable operation are removed, these being defined as times within one hour of radioactive source transport near the detector or in a 24-h window following any significant interruption to operation. The first 25 s of every expansion is discarded to remove transient effects. Of the 34.3 days the detector was expanded, 30.0 live days (87.4%) are considered in the WIMP search.

Bubble images are identified using the same entropy algorithm as used for the optical trigger. The pixel coordinates are then reconstructed into spatial coordinates using ray propagation in a simulated optical geometry. The fiducial volume is determined by setting cut values on isolated wall and surface event distributions in the source calibration and prephysics background data sets, and is shown in Fig. 1. These cuts remove events on or near the surface or within 6 mm of the nominal wall location. For regions of the detector where the optics are worse, such as the transition to the lower hemisphere, the outer 13 mm are removed. The fiducial cuts accept a mass of 45.7 ± 0.5 kg, or 87.7% of the total C_3F_8 mass.

The first step in the WIMP candidate selection removes events that are written improperly on disk, events that were

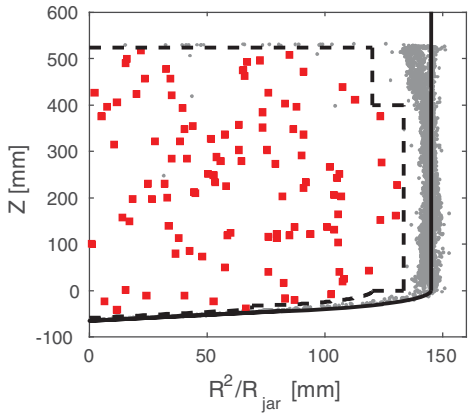

FIG. 1. Spatial distribution of single-bubble events in the WIMP search data. Z is the reconstructed vertical position of the bubble, and R^2/R_{jar} is the distance from the center axis squared, normalized by the nominal jar radius (145 mm). The fiducial cut is represented by the dashed line. The red squares are the 106 single bulk bubbles passing all cuts prior to acoustic unblinding and the gray dots are all rejected single-bubble events.

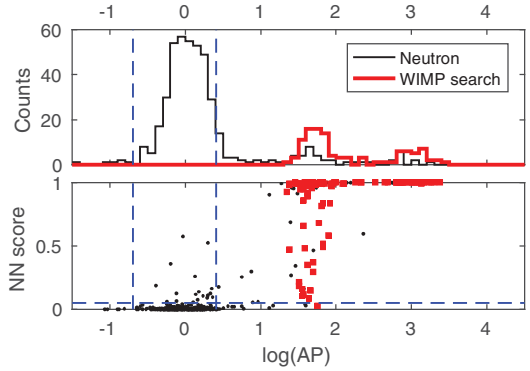

FIG. 2. Top: AP distributions for AmBe and ^{252}Cf neutron calibration data (black) and WIMP search data (red) at a 3.3 keV threshold. Bottom: AP and NN score for the same data set. The acceptance region for nuclear recoil candidates, defined before WIMP search acoustic data unmasking using neutron calibration data, is displayed with dashed lines and reveals no candidate events in the WIMP search data. Alphas from the ^{222}Rn decay chain can be identified by their time signature and populate the two peaks in the WIMP search data at a high AP. Higher energy alphas from ^{214}Po are producing larger acoustic signals.

not triggered by the cameras, and events for which the pressure was more than 1 psi from the target pressure. The signal acceptance for these cuts is greater than 99.9%. Only events that are optically reconstructed as a single bubble are selected as WIMP candidates. This cut removes neutron-induced multiple-bubble events and events for which the optical reconstruction failed. The acceptance of this cut is $98.0\% \pm 0.5\%$. In addition to the optical reconstruction fiducial cut, fiducial-bulk candidates are selected based on a rate-of-pressure-rise measurement, which is found to accept all optically reconstructed single bulk bubbles in the source calibration data.

The acoustic analysis is similar to the procedure described in Ref. [11] to calculate the acoustic parameter (AP), a measurement of the bubble's nucleation acoustic energy. As the AP is used to discriminate alpha particles from nuclear recoils, events with high pretrigger acoustic noise or an incorrectly reconstructed signal start time are removed from the WIMP candidates selection. The efficiency for these acoustic quality cuts is $99.6\% \pm 0.2\%$. For this analysis, based on the prephysics background and calibration data, the AP is found to optimally discriminate alpha particles from nuclear recoils using the signals of two out of the three working acoustic transducers in the 55 to 120 kHz frequency range. The AP distribution for nuclear recoil events is normalized to 1 based on AmBe and ^{252}Cf nuclear recoil calibration data.

An additional metric, the NN score, is constructed from the piezo traces using a neural network [20] trained to distinguish pure alpha events (NN score = 1) from pure nuclear or electron recoil events (NN score = 0). The two-layer feedforward network takes as an input the bubble's 3D position and the noise-subtracted acoustic energy of each of three working acoustic transducers in eight frequency bands ranging from 1 to 300 kHz. The network is trained and validated with source calibration data and the prephysics background data. A nuclear recoil candidate is defined as having an AP between 0.5 to 1.5 and a NN score less than 0.05. These combined acoustic cuts are determined to have an acceptance of $88.5\% \pm 1.6\%$ based on neutron calibration single bulk bubbles.

In the WIMP search data, before unmasking acoustic information, all single bulk bubbles are identified and manually scanned. Any events with mismatched pixel coordinates are discarded. The same procedure is found to keep $98.7\% \pm 0.7\%$ of the single bulk bubbles in the neutron calibration data. A total of 106 single bulk bubbles pass all cuts prior to acoustic unblinding and are shown in Fig. 1. The unmasking of the acoustic data, performed after completion of the WIMP search run, reveals that none of the identified 106 single bulk bubbles are consistent with the nuclear recoil hypothesis defined by the AP and NN score, as shown in Fig. 2. Instead, all 106 single bulk bubbles are alphalike in their acoustic response. The final efficiencies and exposures for the WIMP search are summarized in Table I.

TABLE I. Summary of the final number of events and exposure determination for singles and multiples in the 30.0 live-day WIMP search data set of PICO-60 C_3F_8 at a 3.3 keV thermodynamic threshold.

Data set	Efficiency (%)	Fiducial mass (kg)	Exposure (kg day)	No. of events
Singles	85.1 ± 1.8	45.7 ± 0.5	1167 ± 28	0
Multiples	99.4 ± 0.1	52.2 ± 0.5	1555 ± 15	3

Neutrons produced by (α, n) and spontaneous fission from ^{238}U and ^{232}Th characteristically scatter multiple times in the detector. The multiple-bubble events are an unambiguous signature and provide a measurement of the neutron background. To isolate multiple-bubble events in the WIMP search data, we do not apply acoustic or fiducial cuts, resulting in the larger exposure shown in Table I. Instead, given the $99.5\% \pm 0.1\%$ efficiency to reconstruct at least one bubble in the bulk for a multiple-bubble event, every passing event is scanned for multiplicity. This scan reveals three multiple-bubble events in the WIMP search data set. Based on a detailed Monte Carlo simulation, the background from neutrons is predicted to be 0.25 ± 0.09 (0.96 ± 0.34) single- (multiple-)bubble events. PICO-60 was exposed to a 1 mCi ^{133}Ba source both before and after the WIMP search data, which, compared against a Geant4 [21] Monte Carlo simulation, gives a measured nucleation efficiency for electron recoil events above 3.3 keV of $(1.80 \pm 0.38) \times 10^{-10}$. Combining this with a Monte Carlo simulation of the external gamma flux from Refs. [16,22], we predict 0.026 ± 0.007 events due to electron recoils in the WIMP search exposure. The background from coherent scattering of ^{8}B solar neutrinos is calculated to be 0.055 ± 0.007 events.

We use the same shapes of the nucleation efficiency curves for fluorine and carbon nuclear recoils as found in Ref. [8], rescaled upwards in recoil energy to account for the 2% difference in thermodynamic threshold. We adopt the standard halo parametrization [23], with the following parameters: $\rho_D = 0.3$ GeV c^{-2} cm^{-3}, $v_{\rm esc} = 544$ km/s, $v_{\rm Earth} = 232$ km/s, and $v_o = 220$ km/s. We use the effective field theory treatment and nuclear form factors described in Refs. [24–27] to determine the sensitivity to both spin-dependent and spin-independent dark matter interactions. For the SI case, we use the M response of Table 1 in Ref. [24], and for SD interactions, we use the sum of the Σ' and Σ'' terms from the same table. To implement these interactions and form factors, we use the publicly available DMDD code package [27,28]. The calculated Poisson upper limits at the 90% C.L. for the spin-dependent WIMP-proton and spin-independent WIMP-nucleon elastic scattering cross sections, as a function of WIMP mass, are shown in Figs. 3 and 4. These limits, corresponding to an upper limit on the spin-dependent WIMP-proton cross section of 3.4×10^{-41} cm^2 for a 30 GeV c^{-2} WIMP, are currently the world-leading constraints in the WIMP-proton spin-dependent sector and indicate an improved sensitivity to the dark matter signal of a factor of 17, compared to previously reported PICO results.

A comparison of our proton-only SD limits with neutron-only SD limits set by other dark matter search experiments is achieved by setting constraints on the effective spin-dependent WIMP-neutron and WIMP-proton couplings a_n and a_p that are calculated according to the method proposed in Ref. [46]. The expectation values for the proton and neutron spins for the ^{19}F nucleus are taken from Ref. [24]. The allowed region in the a_n-a_p plane is shown for a 50 GeV c^{-2} WIMP in Fig. 5. We find that PICO-60 C_3F_8 improves the constraints on a_n and a_p, in complementarity with other dark matter search experiments that are more sensitive to the WIMP-neutron coupling.

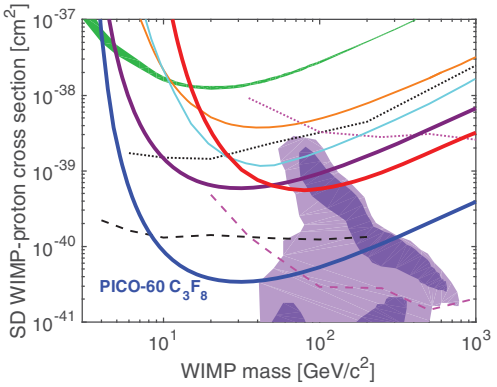

FIG. 3. The 90% C.L. on the SD WIMP-proton cross section from PICO-60 C_3F_8 plotted in thick blue, along with limits from PICO-60 CF_3I (thick red) [10], PICO-2L (thick purple) [9], PICASSO (green band) [14], SIMPLE (orange) [15], PandaX-II (cyan) [29], IceCube (dashed and dotted pink) [30], and SuperK (dashed and dotted black) [31,32]. The indirect limits from IceCube and SuperK assume annihilation to τ leptons (dashed) and b quarks (dotted). The purple region represents parameter space of the constrained minimal supersymmetric model of Ref. [33]. Additional limits, not shown for clarity, are set by LUX [34] and XENON100 [35] (comparable to PandaX-II) and by ANTARES [36,37] (comparable to IceCube).

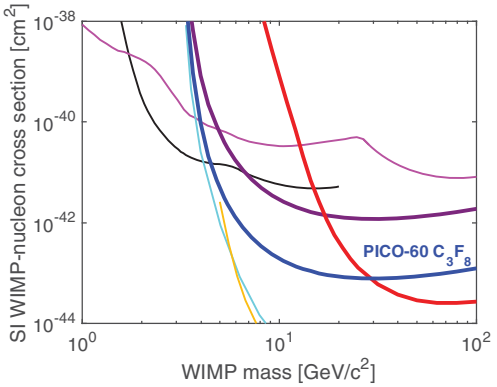

FIG. 4. The 90% C.L. on the SI WIMP-nucleon cross section from PICO-60 C_3F_8 plotted in thick blue, along with limits from PICO-60 CF_3I (thick red) [10], PICO-2L (thick purple) [9], LUX (yellow) [38], PandaX-II (cyan) [39], CRESST-II (magenta) [40], and CDMS-lite (black) [41]. While we choose to highlight this result, LUX sets the strongest limits on WIMP masses greater than 6 GeV/c^2. Additional limits, not shown for clarity, are set by PICASSO [14], XENON100 [35], DarkSide-50 [42], SuperCDMS [43], CDMS-II [44], and Edelweiss-III [45].

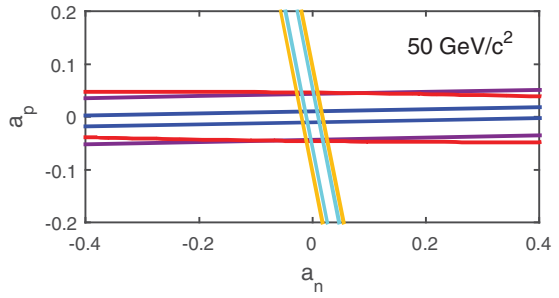

FIG. 5. PICO-60 constraints (blue) on the effective spin-dependent WIMP-proton and WIMP-neutron couplings, a_p and a_n, for a 50 GeV$/c^2$ WIMP mass. Parameter space outside of the band is excluded. Also shown are results from PANDAX-II (cyan) [29], LUX (yellow) [34], PICO-2L (purple) [9], and PICO-60 C_3FI (red) [10].

The LHC has significant sensitivity to dark matter, but to interpret LHC searches, one must assume a specific model to generate the signal that is then looked for in the data. Despite this subtlety, the convention has been to show LHC limits alongside more general direct detection constraints in the parameter space of Fig. 3. We choose instead to compare our limits with those of the LHC on the chosen model, as shown in Fig. 6. The LHC Dark Matter Working Group has made recommendations on a set of simplified models to be used in LHC searches and the best way to present such results [47–49]. For a given simplified model involving a mediator exchanged via the s channel, there are four free parameters: the dark matter mass m_{DM}, the mediator mass m_{med}, the universal mediator coupling to quarks g_q, and the mediator coupling to dark matter g_{DM}. We make a direct comparison of the sensitivity of PICO to that of CMS [50,51] by applying our results to the specific case of a simplified dark matter model involving an axial-vector s-channel mediator. Following Eqs. (4.7)–(4.10) of Ref. [49], we find an expression for the spin-dependent cross section as a function of those free parameters, and we invert this expression to find m_{med} as a function of the cross section. For this comparison, we assume $g_q = 0.25$ and $g_{\mathrm{DM}} = 1$. With this simple translation onto the specified model, we can plot our limits on the same m_{DM}-m_{med} plane, and the results are shown in Fig. 6.

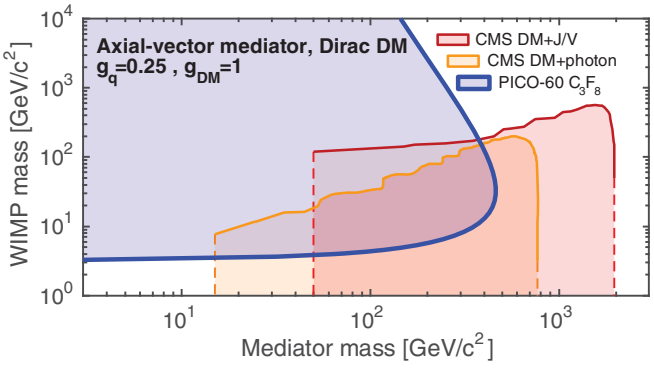

FIG. 6. Exclusion limits at the 95% C.L. in the m_{DM}-m_{med} plane. PICO-60 constraints (thick blue) are compared against collider constraints from CMS for an axial-vector mediator using the monojet and mono-V (red) [50] and monophoton (orange) [51] channels. The shaded regions signify excluded parameter space for the chosen model. A similar analysis by ATLAS can be found in Ref. [52].

The PICO Collaboration wishes to thank SNOLAB and its staff for support through underground space, logistical, and technical services. SNOLAB operations are supported by the Canada Foundation for Innovation and the Province of Ontario Ministry of Research and Innovation, with underground access provided by Vale at the Creighton mine site. We are grateful to Kristian Hahn and Stanislava Sevova of Northwestern University and Björn Penning of the University of Bristol for their assistance and useful discussion. We wish to acknowledge the support of the Natural Sciences and Engineering Research Council of Canada (NSERC) and the Canada Foundation for Innovation (CFI) for funding. We acknowledge the support from National Science Foundation (NSF) (Grants No. 0919526, No. 1506337, No. 1242637, and No. 1205987). We acknowledge that this work is supported by the U.S. Department of Energy (DOE) Office of Science, Office of High Energy Physics (under Award No. DE-SC-0012161), by a DOE Office of Science Graduate Student Research (SCGSR) award, by Dirección General Asuntos del Personal Académico, Universidad Nacional Autónoma de México (DGAPA-UNAM) through the grant Programa de Apoyo a Proyectos de Investigación e Innovación Tecnológica (PAPIIT) No. IA100316 and by Consejo Nacional de Ciencia y Tecnología (CONACyT) (Mexico) through Grant No. 252167, by the Department of Atomic Energy (DAE), the Government of India, under the Center of AstroParticle Physics II project (CAPP-II) at Saha Institute of Nuclear Physics (SINP), by the Czech Ministry of Education, Youth and Sports (Grant No. LM2015072), and by the Spanish Ministerio de Economía y Competitividad, Consolider MultiDark (Grant No. CSD2009-00064). This work is partially supported by the Kavli Institute for Cosmological Physics at the University of Chicago through NSF Grant No. 1125897, and an endowment from the Kavli Foundation and its founder Fred Kavli. We also wish to acknowledge the support from Fermi National Accelerator Laboratory under Contract No. De-AC02-07CH11359, and Pacific Northwest National Laboratory, which is operated by Battelle for the U.S. Department of Energy under Contract No. DE-AC05-76RL01830. We also thank Compute Canada and the Center for Advanced Computing, ACENET, Calcul Québec, Compute Ontario, and WestGrid for the computational support.

*danielbaxter2013@u.northwestern.edu
†ggiroux@owl.phy.queensu.ca

[1] K. A. Olive *et al.* (Particle Data Group), Chin. Phys. C **38**, 090001 (2014).

[2] See E. Komatsu *et al.*, Astrophys. J. Suppl. Ser. **180**, 330 (2009) and references therein.
[3] G. Jungman, M. Kamionkowski, and K. Griest, Phys. Rep. **267**, 195 (1996).
[4] M. W. Goodman and E. Witten, Phys. Rev. D **31**, 3059 (1985).
[5] P. Cushman *et al.*, arXiv:1310.8327.
[6] G. Bertone, D. Hooper, and J. Silk, Phys. Rep. **405**, 279 (2005); J. L. Feng, Annu. Rev. Astron. Astrophys. **48**, 495 (2010).
[7] F. Aubin *et al.*, New J. Phys. **10**, 103017 (2008).
[8] C. Amole *et al.*, Phys. Rev. Lett. **114**, 231302 (2015).
[9] C. Amole *et al.*, Phys. Rev. D **93**, 061101 (2016).
[10] C. Amole *et al.*, Phys. Rev. D **93**, 052014 (2016).
[11] E. Behnke *et al.*, Phys. Rev. D **86**, 052001 (2012).
[12] E. Behnke, J. Behnke, S. J. Brice, D. Broemmelsiek, J. I. Collar, P. S. Cooper, M. Crisler, C. E. Dahl, D, Fustin, J. Hall, J. H. Hinnefeld, M. Hu, I. Levine, E. Ramberg, T. Shepherd, A. Sonnenschein, and M. Szydagis, Phys. Rev. Lett. **106**, 021303 (2011).
[13] S. Archambault *et al.*, Phys. Lett. B **711**, 153 (2012).
[14] E. Behnke *et al.*, Astropart. Phys. **90**, 85-92 (2017).
[15] M. Felizardo, T. A. Girard, T. Morlat, A. C. Fernandes, A. R. Ramos, J. G. Marques, A. Kling, J. Puibasset, M. Auguste, D. Boyer, A. Cavaillou, J. Poupeney, C. Sudre, F. P. Carvalho, M. I. Prudencio, and R. Marques, Phys. Rev. D **89**, 072013 (2014).
[16] A. E. Robinson, Ph.D. thesis, University of Chicago, 2015.
[17] U.S. Department of Defense, Military Standard: Products Cleanliness Levels and Contamination Control Program (1994).
[18] K. Klaasen, Galileo Technical Reports No. JPL D-5880 and No. 1625-210, 1993.
[19] E. W. Lemmon, M. L. Huber, and M. O. McLinden, *NIST Standard Reference Database 23: Reference Fluid Thermodynamic and Transport Properties-REFPROP, Version 9.0, National Institute of Standards and Technology, Standard Reference Data Program* (National Institute of Standards and Technology, Gaithersburg, MD, 2010).
[20] MATLAB: Neural Network Toolbox, The MathWorks, Inc., Natick, Massachusetts.
[21] S. Agostinelli *et al.*, Nucl. Instrum. Methods Phys. Res., Sect. A **506**, 250 (2003); J. Allison *et al.*, IEEE Trans. Nucl. Sci. **53**, 270 (2006).
[22] D. Fustin, Ph.D thesis, University of Chicago, 2012.
[23] J. D. Lewin and P. F. Smith, Astropart. Phys. **6**, 87 (1996).
[24] A. L. Fitzpatrick, W. Haxton, E. Katz, N. Lubbers, and Y. Xu, J. Cosmol. Astropart. Phys. 02 (2013) 004.
[25] N. Anand, A. L. Fitzpatrick, and W. C. Haxton, Phys. Rev. C **89**, 065501 (2014).
[26] M. I. Gresham and K. M. Zurek, Phys. Rev. D **89**, 123521 (2014).
[27] V. Gluscevic, M. I. Gresham, S. D. McDermott, A. H. G. Peter, and K. M. Zurek, J. Cosmol. Astropart. Phys. 12 (2015) 057.
[28] V. Gluscevic and S. D. McDermott, DMDD, Astrophysics Source Code Library, Record ascl:1506.002, 2015.
[29] C. Fu *et al.*, Phys. Rev. Lett. **118**, 071301 (2017).
[30] M. G. Aartsen *et al.*, Eur. Phys. J. C **77**: 146 (2017).
[31] T. Tanaka *et al.*, Astrophys. J. **742**, 78 (2011).
[32] K. Choi *et al.*, Phys. Rev. Lett. **114**, 141301 (2015).
[33] L. Roszkowski, R. R. de Austri, and R. Trotta, J. High Energy Phys. 07 (2007) 075.
[34] D. S. Akerib *et al.*, Phys. Rev. Lett. **116**, 161302 (2016).
[35] E. Aprile *et al.*, Phys. Rev. D **94**, 122001 (2016).
[36] S. Adrián-Martínez *et al.*, Phys. Lett. B **759**, 69 (2016).
[37] S. Adrián-Martínez *et al.*, J. Cosmol. Astropart. Phys. 05 (2016) 016.
[38] D. S. Akerib *et al.*, Phys. Rev. Lett. **118**, 021303 (2017).
[39] A. Tan *et al.*, Phys. Rev. Lett. **117**, 121303 (2016).
[40] G. Angloher *et al.*, Eur. Phys. J. C **76**: 25 (2016).
[41] R. Agnese *et al.*, Phys. Rev. Lett. **116**, 071301 (2016).
[42] P. Agnes *et al.*, Phys. Rev. D **93**, 081101 (2016).
[43] R. Agnese *et al.*, Phys. Rev. Lett. **112**, 241302 (2014).
[44] R. Agnese *et al.*, Phys. Rev. D **92**, 072003 (2015).
[45] L. Hehn *et al.*, Eur. Phys. J. C **76**: 548 (2016).
[46] D. R. Tovey, R. J. Gaitskell, P. Gondolo, Y. Ramachers, and L. Roszkowski, Phys. Lett. B **488**, 17 (2000).
[47] O. Buchmueller, M. J. Dolan, S. A. Malik, and C. McCabe, J. High Energy Phys. 01 (2015) 037.
[48] D. Abercrombie *et al.*, arXiv:1507.00966.
[49] A. Boveia *et al.* Report No. CERN-LPCC-2016-001, 2016; arXiv:1603.04156,
[50] CMS Collaboration, Report No. CMS-PAS-EXO-16-037, 2016.
[51] CMS Collaboration, Report No. CMS-PAS-EXO-16-039, 2016.
[52] M. Aaboud *et al.*, Phys. Rev. D **94**, 032005 (2016).

Appendix B

PICO-60 C_3F_8 COMPLETE EXPOSURE PAPER

[To be published]

Dark Matter Search Results from the Complete Exposure of the PICO-60 C_3F_8 Bubble Chamber

C. Amole,[1] M. Ardid,[2] I. J. Arnquist,[3] D. M. Asner,[4] D. Baxter,[5,6] E. Behnke,[7] M. Bressler,[8] B. Broerman,[1] G. Cao,[1] C. J. Chen,[5] U. Chowdhury,[1] K. Clark,[1] J. I. Collar,[9] P. S. Cooper,[6] M. Crisler,[6,3] G. Crowder,[1] N.A. Cruz-Venegas,[10] C. E. Dahl,[5,6] M. Das,[11] S. Fallows,[12,*] J. Farine,[13] I. Felis,[2] R. Filgas,[14] F. Girard,[13,15] G. Giroux,[1] J. Hall,[3] O. Harris,[16] E. W. Hoppe,[3] M. Jin,[5] L. Klopfenstein,[7] C. B. Krauss,[12] M. Laurin,[15] I. Lawson,[13,17] A. Leblanc,[13] I. Levine,[7] W. H. Lippincott,[6] F. Mamedov,[14] D. Maurya,[18] P. Mitra,[12] T. Nania,[7] R. Neilson,[8,†] A. J. Noble,[1] P. Oedekerk,[7] S. Olson,[1] A. Ortega,[9] M.-C. Piro,[12] A. Plante,[15] R. Podviyanuk,[13] S. Priya,[18] A. E. Robinson,[15] R. Rucinski,[6] S. Sahoo,[11] O. Scallon,[13] S. Seth,[11] A. Sonnenschein,[6] N. Starinski,[15] I. Štekl,[14] T. Sullivan,[1] F. Tardif,[15] E. Vázquez-Jáuregui,[10,13] N. Walkowski,[7] U. Wichoski,[13] Y. Yan,[18] V. Zacek,[15] and J. Zhang[5,‡]

(PICO Collaboration)

[1]*Department of Physics, Queen's University, Kingston, K7L 3N6, Canada*
[2]*Departament de Física Aplicada, IGIC - Universitat Politècnica de València, Gandia 46730 Spain*
[3]*Pacific Northwest National Laboratory, Richland, Washington 99354, USA*
[4]*Brookhaven National Laboratory, Upton, New York 11973, USA*
[5]*Department of Physics and Astronomy, Northwestern University, Evanston, Illinois 60208, USA*
[6]*Fermi National Accelerator Laboratory, Batavia, Illinois 60510, USA*
[7]*Department of Physics, Indiana University South Bend, South Bend, Indiana 46634, USA*
[8]*Department of Physics, Drexel University, Philadelphia, Pennsylvania 19104, USA*
[9]*Enrico Fermi Institute, KICP and Department of Physics, University of Chicago, Chicago, Illinois 60637, USA*
[10]*Instituto de Física, Universidad Nacional Autónoma de México, México D. F. 01000, México*
[11]*Astroparticle Physics and Cosmology Division, Saha Institute of Nuclear Physics, Kolkata, India*
[12]*Department of Physics, University of Alberta, Edmonton, T6G 2E1, Canada*
[13]*Department of Physics, Laurentian University, Sudbury, P3E 2C6, Canada*
[14]*Institute of Experimental and Applied Physics, Czech Technical University in Prague, Prague, Cz-12800, Czech Republic*
[15]*Département de Physique, Université de Montréal, Montréal, H3C 3J7, Canada*
[16]*Northeastern Illinois University, Chicago, Illinois 60625, USA*
[17]*SNOLAB, Lively, Ontario, P3Y 1N2, Canada*
[18]*Bio-Inspired Materials and Devices Laboratory (BMDL), Center for Energy Harvesting Material and Systems (CEHMS), Virginia Tech, Blacksburg, Virginia 24061, USA*

(Dated: July 18, 2018)

New results are reported from continued operation of the PICO-60 dark matter detector, a bubble chamber filled with 52 kg of C_3F_8 located in the SNOLAB underground laboratory. The chamber was successfully operated at thermodynamic thresholds as low as 1.2 keV while remaining stable. A second, blind 1404-kg-day exposure at 2.45 keV threshold was acquired with approximately the same expected total background rate as the previous 1167-kg-day exposure at 3.3 keV. A new, more stringent limit is set in the region of WIMP mass below 5 GeV.

PACS numbers: 29.40.-n, 95.35.+d, 95.30.Cq, FERMILAB-PUB-XX-XXX-XX-XXX

I. INTRODUCTION

Identifying the nature of the cold dark matter is one of the primary challenges in modern physics [1–5]. Direct detection dark matter experiments with sensitivity to the very small recoil energies (1–100 keV) expected from elastic scatters of WIMPs on target nuclei are designed to acquire large background-free exposures. This has required scaling up detector masses while continuing to eliminate all sources of interactions that would act as backgrounds to a WIMP interaction signal. The operators characterizing this interaction are typically parametrized into spin-independent (SI) and spin-dependent (SD) couplings, and as the underlying mechanism remains unknown, it is essential for a WIMP-search program to probe both SI and SD couplings.

The superheated liquid detector technology used by the PICO collaboration affords excellent intrinsic rejection of electron recoils from gamma and beta particles. Alpha decays of U/Th daughter nuclei can be acoustically discriminated against using piezoelectric sensors

* fallows@ualberta.ca
† neilson@drexel.edu
‡ now at Argonne National Laboratory

mounted on the detector surface. Materials screening and optimized detector design minimize the remaining sources of neutron background, with the goal of acquiring a background-free WIMP-search exposure. The first blind exposure of the PICO-60 C_3F_8 detector [13] achieved this goal, acquiring a 1167-kg-day exposure at a thermodynamic threshold of 3.3 keV with zero single-scatter nuclear recoil candidates in the signal region after unblinding.

Three multi-bubble events were observed during that exposure, while 0.25 ± 0.09 (0.96 ± 0.34) single(multiple)-scatter neutron events were predicted by simulation (Sec. V A), indicating that the detector was effectively neutron-limited, unable to attain significant additional WIMP sensitivity simply by acquiring longer exposures.

Following post-run calibrations, an attempt was made to explore the limits of detector stability while testing for the appearance of the predicted environmental gamma background (Sec. V B), by significantly reducing the detector's bubble nucleation threshold. The C_3F_8 temperature was increased from $(13.9 \pm 0.1)\,^{\circ}$C to $(15.9 \pm 0.1)\,^{\circ}$C and the superheated pressure was progressively reduced from (30.2 ± 0.3) psia to (21.7 ± 0.3) psia, effecting a reduction in the nucleation threshold (Sec. III) from (3.29 ± 0.09) keV to (1.81 ± 0.09) keV. The detector continued to operate stably, maintaining a live-time fraction over 75% during these periods, despite the higher rate of bulk single-bubble events, attributed primarily to increased sensitivity to the electron-recoil background.

In response, a second blind exposure was acquired between April and June 2017 at a threshold of 2.45 keV, for which the overall background rate was expected to be indistinguishable from the rate at 3.29 keV. Here we report the results of that efficiency-corrected dark matter exposure of 1404-kg-days.

Just prior to decommissioning, the temperature was raised to $(19.9 \pm 0.1)\,^{\circ}$C, enabling a threshold as low as (1.20 ± 0.09) keV to be reached. As expected, the event rate was then dominated by events consistent with electron recoils, but operations remained stable. The higher event rate led to a reduced live-time fraction near 40% at this lowest threshold. These operating conditions are summarized in Table I.

II. EXPERIMENTAL METHOD

The PICO-60 apparatus (Fig. 1) was configured as described in detail in [10], with the following changes implemented in 2016. Rather than CF_3I, the bubble chamber was filled with (52.2 ± 0.5) kg of C_3F_8, as first reported in [13]. As the superheated operating temperatures for C_3F_8 are lower than those in CF_3I, a new chiller system was used to hold the temperature of the surrounding water tank [10, 13] uniform to approximately 0.1 °C. The acoustic transducers, formerly coupled to the inner vessel with epoxy, were changed to a spring-loaded coupling. The chamber's expansion cycle was identical to the previous run [13], with only occasional minor alterations as required to respond to temporarily elevated trigger-rates observed after the position of the water-target interface shifted due to thermal expansion.

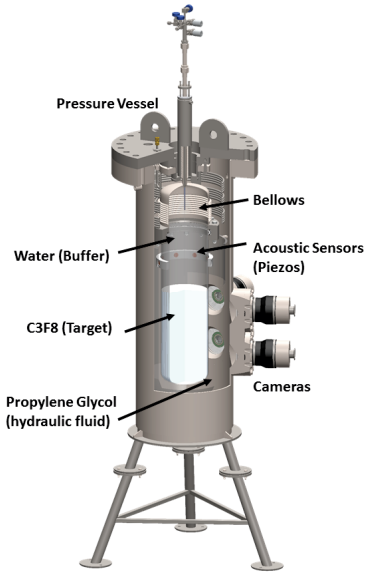

FIG. 1. The PICO-60 detector as configured for its operation with C_3F_8. The full volume of target fluid is stereoscopically imaged by two columns of two cameras each.

As in [13], in order to image the entire C_3F_8 volume, double that of the CF_3I used in the first run of PICO-60 [10], it was necessary to install an upper row of cameras, resulting in a stereoscopic view by each of two vertical pairs. As part of this expansion in scale, the data acquisition hardware and software running the cameras and issuing the primary event trigger was restructured and modularized. Each column of cameras was controlled by a separate server continuously acquiring images at 340 Hz, improved time resolution compared to the 200 Hz used for the previous exposure [13]. Each camera filled a ring buffer with incoming images while their control software monitored for the appearance of bubbles by continuously calculating the image entropy $S_I = -\sum_i P_i \log_2 P_i$, where P_i is the fraction of pixels populating intensity bin i of the difference map histograms generated from consecutive frames. These camera servers communicated operational state changes and trigger conditions to the primary data acquisition server managing event-level operation of the chamber. The cameras were sent a single digital pulse train to synchronize their exposure timing. This signal was also used to drive the pulse timing of the LEDs illuminating the chamber's inner volume.

The chamber was primarily operated at four additional sets of thermodynamic conditions, summarized in Table I. For the (2.45 ± 0.09) keV threshold, a second blind analysis [13] was undertaken by defining and beginning to acquire a new category of background data that imple-

T (°C)	P (psia)	Seitz threshold, E_T (keV)	Livetime (d)	Exposure (kg-d)
19.9	25.5	$1.20 \pm 0.1(\text{exp}) \pm 0.1(\text{th})$	0.21	8.2
19.9	34.3	$1.58 \pm 0.1(\text{exp}) \pm 0.1(\text{th})$	1.29	50.3
15.9	21.7	$1.81 \pm 0.1(\text{exp}) \pm 0.2(\text{th})$	7.04	310.81
15.9	30.5	$2.45 \pm 0.1(\text{exp}) \pm 0.2(\text{th})$	29.95	1404.22
13.9	30.2	$3.29 \pm 0.1(\text{exp}) \pm 0.2(\text{th})$	29.96	1167

TABLE I. Details of the four new operating conditions and their associated exposures, as well as the original set of conditions used in [13]. The two blind exposures are grouped in the lower rows. The experimental uncertainty on the threshold comes from uncertainties on the temperature (0.1 °C) and pressure (0.3 psi), while the theoretical uncertainty comes from the thermodynamic properties of C_3F_8, including the surface tension and dominated by uncertainty in the Tolman length [33].

mented randomization in the processing of the acoustic signals that allow discrimination between alpha decays and nuclear or electron recoil events. Source calibrations and pre-physics background data were used to finalize cuts and efficiencies for bulk single recoil event candidates in an unbiased manner. After this analysis was frozen, acoustic information for the physics data set was processed and the acceptance region was examined.

For the three lowest thresholds, acoustic information was never blinded, and a full analysis not performed, as these data sets were always expected to contain many gamma-induced recoils indistinguishable from nuclear recoils by their acoustic signals. Furthermore, these lowest thresholds are not supported by comprehensive nuclear recoil calibrations in C_3F_8 as introduced for the thresholds of the blind exposures in Sec. III. These data sets thus act primarily as a confirmation of the ability to operate a bubble chamber stably at very low thresholds.

III. BUBBLE NUCLEATION THRESHOLD

The efficiency with which nuclear recoils nucleate bubbles is measured with a suite of neutron calibration experiments, to which fluorine and carbon efficiency curves at each threshold are fit to monotonically increasing, piecewise linear functions. Well-defined resonances in the ^{51}V(p,n)^{51}Cr reaction are used to produce monoenergetic 50, 61, and 97 keV neutrons directed at a ∼30-ml C_3F_8 bubble chamber at the Tandem Van de Graaff facility at the Université de Montréal. An SbBe neutron source is also deployed adjacent to the ∼30-ml bubble chamber, and an AmBe neutron source adjacent to the PICO-2L chamber [8]. The initial C_3F_8 calibration presented in Ref. [8] and used for the first PICO-60 C_3F_8 result [13] is refined in this analysis with additional calibration data. Datasets have been added for 61 and 97 keV neutron beams and the 50 keV neutron beam dataset is entirely new, as is the SbBe source, a gamma-induced neutron source that primarily produces monoenergetic 24 keV neutrons. Calibrations were preformed at a variety of thermodynamic thresholds, with selected results shown in Figure 2, along with the prediction for the best-fit efficiency model.

Each of the neutron calibration experiments is simulated in MCNP [22] or Geant4 [23], using updated differential cross sections for elastic scattering on fluorine [24]. The calibration data is fit using the `emcee` Markov Chain Monte Carlo (MCMC) python code package [25]. The output of the fitting is a distribution of sets of four efficiency curves (fluorine and carbon curves at each of the 2.45 and 3.29 keV thresholds) with associated likelihoods (Fig. 3). The addition of the new lower-neutron-energy datasets supports tighter constraints on the low-energy part of the efficiency curves than previously reported, resulting in increased sensitivity to low-mass WIMPs.

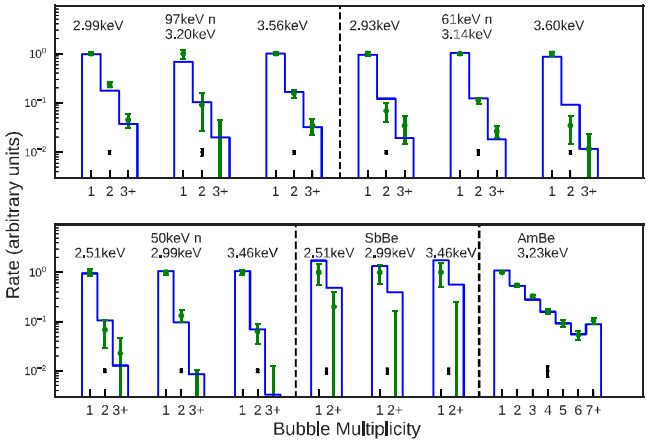

FIG. 2. The green points show the observed rates of single, double, and triple-or-more bubbles for the calibration sources at listed thermodynamic thresholds. Green error bars indicate statistical uncertainties, and the black error bars at the bottom show the systematic uncertainty on the neutron flux. The blue histograms show the predicted rates from the simulation given the best-fit efficiency model derived from all calibration data. Each dataset is normalized to the observed rate of single bubbles, or double bubbles for SbBe due to gamma background. The normalization of the simulation is constrained by the systematic neutron flux uncertainties shown.

IV. DATA ANALYSIS

The new data sets were processed in much the same way as in [13], with several improvements and additions.

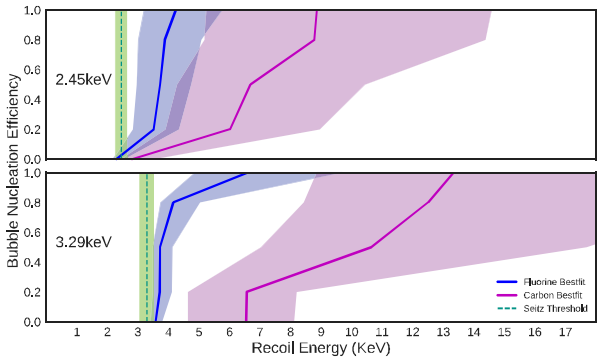

FIG. 3. The best-fit fluorine (blue) and carbon (magenta) efficiency curves for 2.45 keV and 3.29 keV data are shown as the solid lines. The shaded regions show the band enveloping all efficiency curves fitted within 1σ. The light green dashed lines show the calculated Seitz threshold, with theoretical uncertainties from Table I.

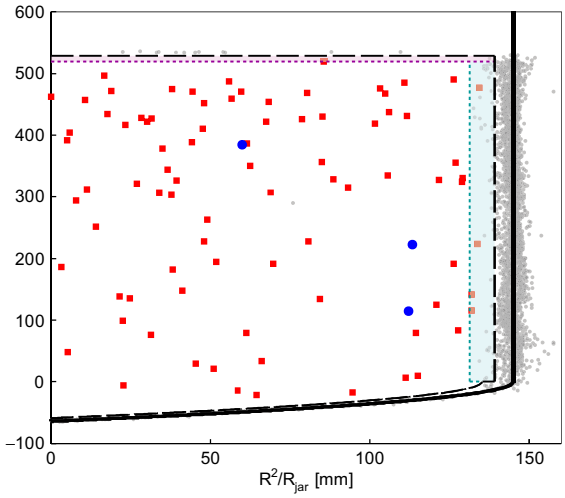

FIG. 4. Spatial distribution of single-bubble events in the 2.45 keV WIMP-search data. Z is the reconstructed vertical position of the bubble, and R^2/R_{jar} is the distance from the center axis squared, normalized by the nominal jar radius (145 mm). The outer edge of the fiducial cut is represented by the dashed black line, outside of which all events are excluded. Events reconstructed within the cyan annular region 3–7 mm from the wall were additionally required to satisfy a condition limiting their track's zenith angle, and events in the near-surface magenta region were additionally required to have appeared in two cameras with a limited offset in frame index. Red squares are the 87 single bulk bubbles passing all cuts prior to acoustic unblinding and grey dots are all rejected single-bubble events. Blue circles are the 3 candidate events passing the AP cut.

Cuts were redefined independently for each set of operating conditions, and to take advantage of an improved optical reconstruction of bubble positions.

The algorithm to reconstruct the spatial position of each bubble was modified to have finer sub-pixel resolution and to monitor and correct for any slight shifts in the overall image position on the sensor grid over time. This algorithm individually weighted each camera's contribution to the reconstruction by the relative quality of the bubble image obtained. Image quality was evaluated as a function of the distance between the bubble's image the center of the camera's sensor, and included corrections for lighting quality that changed as several LEDs failed during operations.

One result of these improvements is that the fiducial mass is increased from (45.7 ± 0.5) kg to (48.9 ± 0.2) kg. These new fiducial cuts use improved time-resolution to reconstruct vectors tracking bubble motion for ten frames after first visibility, which are then used to reject single bubble events in the near-wall region having highly angled tracks characteristic of nucleations originating on the detector walls, with a uniform 95.6% acceptance of non-wall events in this annular region. Similarly, events near the surface, where visibility is less favorable, were required to be detected by both cameras within 30 ms of each other, to limit uncertainties in position reconstruction. This cut had 100% acceptance of non-surface events in the cylindrical near-surface region. Together, these optimizations allow fiducial cut boundaries to be placed more closely to the edge of the detector while still classifying zero surface- or wall-originating events as fiducial. A manual scan for misalignment of pixel coordinates found zero single bubble candidates reconstructed in an incorrect position.

Time-dependent effects over the blind exposure were minimal. The signal from a Dytran fast pressure transducer, a polynomial fit to which during early bubble growth can very accurately identify bubble multiplicity, drifted over time, but was straightforwardly renormalized. The magnitude of acoustic signals from bubble nucleation is strongly dependent on the temperature and pressure of the superheated liquid. Single bubble events from ^{252}Cf neutron and ^{133}Ba gamma calibration data were used to independently renormalize the acoustic scaling at each set of thermodynamic conditions.

V. BACKGROUND ESTIMATES

Backgrounds are estimated from a combination of Monte Carlo simulations and measured calibration event rates during threshold scans. The total expected background rate is the sum of the following contributions, and is summarized in Table II.

A. Neutron background

Geant4 simulations of the detector geometry and composition lead to estimates of the expected neutron flux in the detector. The background from neutrons during the blind exposure is expected to be 0.38±0.15 singles and 1.43±0.49 multiples. Two multi-bubble events were observed during the second blind exposure, along with one during an intervening ^{60}Co gamma calibration, in addition to the three observed during the first blind exposure [13]. Two neutron single-bubble events over the total 60-day blind exposure is the most probable value, as inferred from the observed multiples and the simulated ratio of single-bubble to multi-bubble events.

B. Gamma background

Gamma calibration was performed at 2.45 keV with a 0.1 mCi ^{60}Co source before and after the blinded run. Compared with a Geant4 simulation of the same detector geometry, this produces a measured nucleation efficiency of $(2.89 \pm 0.15)\times10^{-9}$ for electron recoil events above 2.45 keV. Combined with the rate of external gammas as simulated in MNCP, based on measurements from a NaI detector in the SNOLAB J drift [ref], we estimate a background of 0.129 ± 0.028 gamma events in 29.95 days for this blind exposure. More advanced models of the gamma response in superheated fluids are currently under development, at present producing even lower estimates for the gamma background in this exposure than the above method.

C. Coherent neutrino scattering background

With energy thresholds below approximately 5 keV, sensitivity to coherent elastic nuclear scattering of ^{8}B solar neutrinos can become a significant contributor to the overall background estimate for sufficiently large exposures. For the blind exposure acquired at 2.45 keV, this background is projected to contribute (0.10 ± 0.02) events.

D. Alpha background

The measured fiducial single-bubble event rate during the second blind run of PICO-60, (2.9 ± 0.3) events/live-day, can be extrapolated to a ^{222}Rn rate under the assumption that each such event represents one of three alpha decays along the ^{222}Rn to ^{210}Po chain. Given the exposure of this data set, this corresponds to an approximate ^{222}Rn rate of 2 µBq in the detector, competitive with [cite DEAP-3600 paper – it was accepted to PRL as of 17 July 2018, but no citation details exist yet]. Excellent separation of the alpha peak from the low-AP recoil peak was maintained across thermodynamic conditions.

Neutron	Gamma	CNS	Total
(0.38 ± 0.15)	(0.13 ± 0.03)	(0.10 ± 0.02)	(0.61 ± 0.15)

TABLE II. Summary of estimated background contributions for the full 30.0 day livetime of the 2.45 keV blind run of PICO-60.

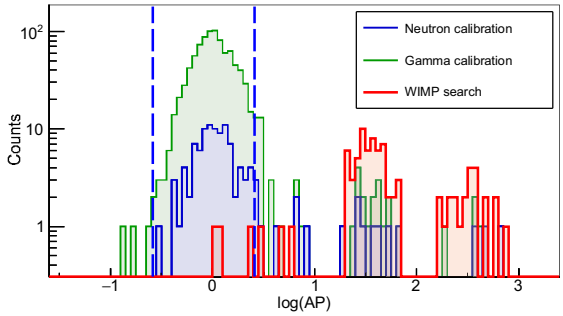

FIG. 5. AP distributions for ^{252}Cf and ^{133}Ba calibration data (black) and WIMP search data (red) at 2.45 keV threshold. The acceptance region for nuclear recoil candidates, defined before WIMP search acoustic data unmasking using neutron calibration data, is displayed with dashed lines and reveals 3 candidate events in the WIMP search data. Alphas from the ^{222}Rn decay chain can be identified by their time signature and populate the two peaks in the WIMP search data at high AP. Higher energy alphas from ^{214}Po produce larger acoustic signals.

VI. WIMP SEARCH RESULTS

After the decision to unblind the 2.45 keV WIMP-search data set, the acoustic signals were processed and are presented in Figure 5 along with the AP distributions for neutron and gamma calibrations. Three nuclear recoil candidates are observed in the WIMP-search signal region, a rate higher than the background prediction from Table II. However, the total observation of three single-bubble and six multiple-bubble events over the combined exposures is not inconsistent with the expected singles-to-multiples ratio of 1:4 for a neutron dominated background, albeit at somewhat higher rate than predicted by our simulations.

A Profile Likelihood Ratio (PLR) test [35] is used to set WIMP exclusion limits on the combination of 2.45 and 3.29 keV datasets. A test statistic is formed from the ratio of the likelihood for a specific WIMP cross-section to the maximum likelihood over all WIMP cross-sections. The background rate and WIMP detection efficiency in each dataset are treated as nuisance parameters, marginalized over by finding the conditional maximum likelihood for each specific WIMP cross-section.

Given the apparent discrepancy between our predicted and observed neutron background, the background rates

Dataset	Efficiency (%)	Fiducial Mass (kg)	Exposure (kg-days)	No. of events
Singles	$95.9\ ^{+1.9}_{-3.4}$	48.8 ± 0.8	$1404\ ^{+48}_{-75}$	3
Multiples	$99.9\ ^{+0.0}_{-0.1}$	52.0 ± 0.1	$1556\ ^{+3}_{-5}$	2

TABLE III. Summary of the final number of events and exposure determination for singles and multiples in the 30.0 live-day WIMP search dataset of PICO-60 C_3F_8 at 2.45 keV thermodynamic threshold.

are unconstrained in the PLR, with flat likelihood functions for all non-negative values.

For the efficiencies, a likelihood surface is created as a function of WIMP detection efficiency at 2.45 and 3.29 keV. WIMP detection efficiencies, Φ, in units of detected WIMPs per kg-day of exposure per picobarn of WIMP-nucleon scattering cross-section, are derived from the calibration MCMC output by integrating the efficiency curves over the nuclear recoil spectrum from an astrophysical WIMP flux for an array of potential WIMP masses. The two-dimensional WIMP detection efficiency space is divided into bins and within each bin the maximum likelihood set of efficiency curves that fall within that bin is found. The likelihood surface thus created retains any covariance between the efficiency at the two thresholds from the neutron calibration.

The standard halo parametrization [27] is used, with the following parameters: ρ_D=0.3 GeVc^{-2}cm^{-3}, $v_{\rm esc}$ = 544 km/s, $v_{\rm Earth}$ = 232 km/s, and v_o = 220 km/s. The effective field theory treatment and nuclear form factors described in Refs.[28–31] are used to determine sensitivity to both spin-dependent and spin-independent dark matter interactions. The M response of Table 1 in Ref. [28] is used for SI interactions, and the sum of the Σ' and Σ'' terms from the same table is used for SD interactions. To implement these interactions and form factors, the publicly available `dmdd` code package [31, 32] is used. Figure 6 shows exanmples of the WIMP detection efficiency likelihood surfaces used for 5 GeV WIMPs with SI coupling and 19 GeV WIMPs with SD-proton coupling. The likelihood surfaces are marginalized over as nuisance parameters within the PLR, after being convolved with a two-dimensional Gaussian function reflecting experimental uncertainty in the PICO-60 thermodynamic thresholds.

To develop a frequentist WIMP exclusion curve, toy datasets are generated at each point in a grid of WIMP masses and cross-sections. A grid point is then excluded if the observed PLR test statistic for that point is larger than >90% of toy dataset test statistics at that point. A conservative choice is made to generate the toy datasets with no background contribution, but the 90% exclusion curve is subsequently confirmed to be valid over the range of background rates consistent with the data. The calculated exclusion curves at 90% C.L. for spin-dependent WIMP-proton and spin-independent WIMP-nucleon eleastic scattering cross-sections, as a function of WIMP mass, are shown in Figures 7 and 8. The already world-leading limits in the spin-dependent WIMP-proton sector are improved, particularly for WIMP-masses in the 3–5 GeV range.

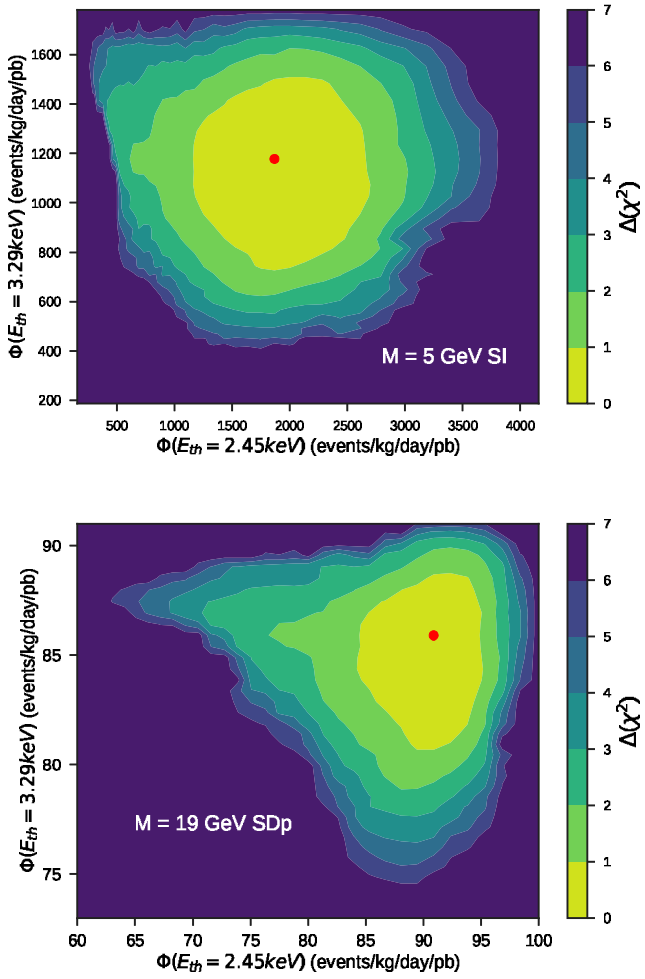

FIG. 6. Contour plot of integrated efficiency Φ at 2.45 keV and 3.29 keV with red dot representing best-fit result. Contour layers have been color-coded to represent the difference in χ^2 with respect to the minimum. Details in the outer boundary of the plot are subject to statistical fluctuations.

VII. ACKNOWLEDGEMENTS

The PICO collaboration wishes to thank SNOLAB and its staff for support through underground space,

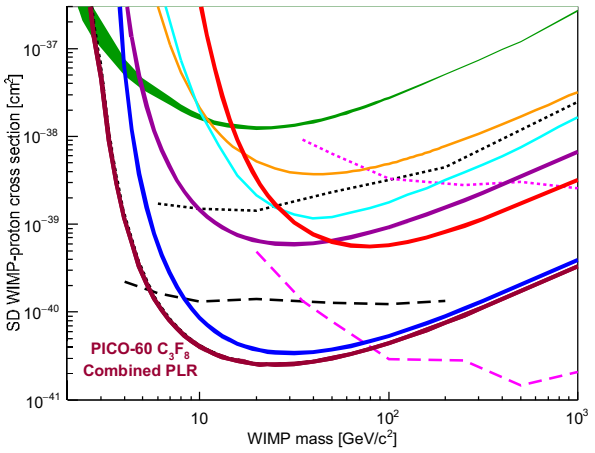

FIG. 7. The 90% C.L. limit on the SD WIMP-proton cross section from the profile likelihood analysis of the PICO-60 C_3F_8 combined blind exposure plotted in thick maroon, along with limits from the first blind exposure of PICO-60 C_3F_8 (thick blue) [13], as well as limits from PICO-60 CF_3I (thick red) [10], PICO-2L (thick purple) [9], PICASSO (green band) [15], SIMPLE (orange) [16], PandaX-II (cyan) [41], IceCube (dashed and dotted pink) [42], and SuperK (dashed and dotted black) [43, 44]. The indirect limits from IceCube and SuperK assume annihilation to τ leptons (dashed) and b quarks (dotted). The purple region represents parameter space of the constrained minimal supersymmetric model of [45]. Additional limits, not shown for clarity, are set by LUX [46] and XENON1T [48] (comparable to PandaX-II) and by ANTARES [49, 50] (comparable to IceCube).

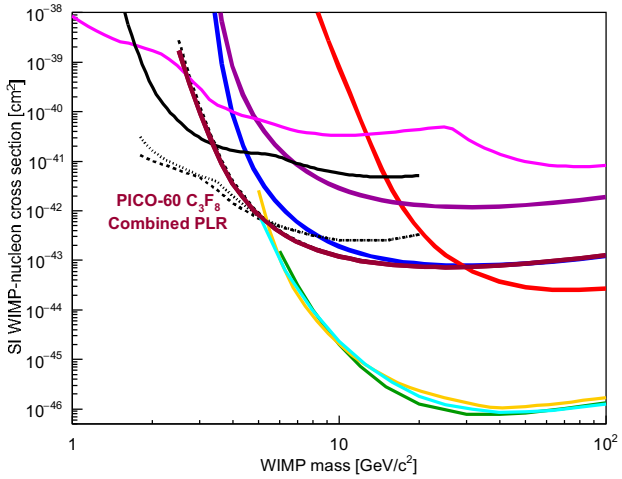

FIG. 8. The 90% C.L. limit on the SI WIMP-nucleon cross-section from the profile likelihood ratio analysis of the PICO-60 C_3F_8 combined blind exposure plotted in thick maroon, along with limits from the first blind exposure of PICO-60 C_3F_8 (thick blue) [13], PICO-60 CF_3I (thick red) [10], PICO-2L (thick purple) [9], LUX (yellow) [51], PandaX-II (cyan) [52], XENON1T (green) [48], CRESST-II (magenta) [53], and CDMS-lite (black) [54]. Additional limits, not shown for clarity, are set by PICASSO [15], XENON100 [47], DarkSide-50 [55], SuperCDMS [56], CDMS-II [57], and Edelweiss-III [58]. [Note: this version includes DarkSide-50 low mass limits in dotted/dashed lines in the same parameter space that this new limit excludes – we're still undecided about whether/how to handle/include this, as it remains unpublished five months after arXiv submission and is not necessarily sufficiently supported by low-energy nuclear recoil calibration data.]

logistical and technical services. SNOLAB operations are supported by the Canada Foundation for Innovation and the Province of Ontario Ministry of Research and Innovation, with underground access provided by Vale at the Creighton mine site. We are grateful to Kristian Hahn and Stanislava Sevova of Northwestern University and Björn Penning of the University of Bristol for their assistance and useful discussion. We wish to acknowledge the support of the Natural Sciences and Engineering Research Council of Canada (NSERC) and the Canada Foundation for Innovation (CFI) for funding. We acknowledge the support from National Science Foundation (NSF) (Grant 0919526, 1506337, 1242637 and 1205987). We acknowledge that this work is supported by the U.S. Department of Energy (DOE) Office of Science, Office of High Energy Physics (under award DE-SC-0012161), by the DOE Office of Science Graduate Student Research (SCGSR) award, by DGAPA-UNAM (PAPIIT No. IA100316 and IA100118) and Consejo Nacional de Ciencia y Tecnología (CONACyT, México, Grant No. 252167), by the Department of Atomic Energy (DAE), the Government of India, under the Center of AstroParticle Physics II project (CAPP-II) at SAHA Institute of nuclear Physics (SINP), the Czech Ministry of Education, Youth and Sports (Grant LM2015072) and the the Spanish Ministerio de Economía y Competitividad, Consolider MultiDark (Grant CSD2009-00064). This work is partially supported by the Kavli Institute for Cosmological Physics at the University of Chicago through NSF grant 1125897, and an endowment from the Kavli Foundation and its founder Fred Kavli. We also wish to acknowledge the support from Fermi National Accelerator Laboratory under Contract No. DE-AC02-07CH11359, and Pacific Northwest National Laboratory, which is operated by Battelle for the U.S. Department of Energy under Contract No. DE-AC05-76RL01830. We also thank Compute Canada (www.computecanada.ca) and the Center for Advanced Computing, ACENET, Calcul Québec, Compute Ontario and WestGrid for the computational support.

[1] K. A. Olive *et al.* (Particle Data Group), Chinese Phys. C **38**, 090001 (2014).

[2] E. Komatsu *et al.*, Astroph. J. Suppl. **180**, 330 (2009) and refs. therein.

[3] G. Jungman, M. Kamionkowski, and K. Griest, Phys. Rep. **267**, 195 (1996).

[4] M. W. Goodman and E. Witten, Phys. Rev. D **31**, 3059 (1985).

[5] P. Cushman *et al.*, Snowmass CF1 Summary: WIMP Dark Matter Direct Detection, arXiv:1310.8327 [hep-ex] (2013).

[6] G. Bertone, D. Hooper, and J. Silk, Phys. Rep. **405**, 279, (2005); J.L. Feng, Ann. Rev. Astr. Astroph., **48**, 496 (2010).

[7] F. Aubin *et al.*, New J. Phys. **10**, 103017 (2008).

[8] C. Amole *et al.*, Phys. Rev. **114**, 231302 (2015).

[9] C. Amole *et al.*, Phys. Rev. D **93**, 061101 (2016).

[10] C. Amole *et al.*, Phys. Rev. D **93**, 052014, (2016).

[11] E. Behnke *et al.*, Phys. Rev. D **86**, 052001 (2012).

[12] E. Behnke *et al.*, Phys. Rev. Lett. **106**, 021303 (2011).

[13] C. Amole *et al.*, Phys. Rev. Lett. **118**, 251301 (2017).

[14] S. Archambault *et al.*, Phys. Lett. B **711**, 153 (2012).

[15] E. Behnke *et al.*, Astropart. Phys. **90**, 85-92 (2017).

[16] M. Felizardo *et al.*, Phys. Rev. D **89**, 072013 (2014).

[17] A. E. Robinson, Ph.D. thesis, University of Chicago (2015).

[18] MIL-STD-1246C, Product Cleanliness Levels and Contamination Control Program, US Department of Defense (1994).

[19] K. Klaasen, Galileo Technical Report JPL D-5880, 1625-210 (1993).

[20] E. W. Lemmon, M. L. Huber, and M. O. McLinden, NIST Standard Reference Database 23: Reference Fluid Thermodynamic and Transport Properties-REFPROP, Version 9.0, National Institute of Standards and Technology, Standard Reference Data Program, Gaithersburg (2010).

[21] MATLAB: Neural Network Toolbox, The MathWorks, Inc., Natick, Massachusetts, United States.

[22] S. A. Pozzi, E. Padovani and M. Marseguerra, Nucl. Instr. Meth. A **513** 550 (2003).

[23] S. Agostinelli *et al*, Nucl. Instr. Meth. A **506** 250-303 (2003); J. Allison *et al*, IEEE Trans. Nucl. Sci. **53** No. 1, 270-278 (2006).

[24] A. E. Robinson, Phys. Rev. C89, 032801 (2014).

[25] D. Foreman-Mackey, D. W. Hogg, D. Lang and J. Goodman, Publications of the Astronomical Society of the Pacific, Volume 125, Issue 925, pp. 306 (2013).

[26] D. Fustin, Ph.D thesis, University of Chicago (2012).

[27] J. D. Lewin and P. F. Smith, Astrop. Phys. **6**, 87 (1996).

[28] A. L. Fitzpatrick *et al.*, J. Cosmol. Astropart. Phys. 02 (2013) 004.

[29] N. Anand, A. L. Fitzpatrick, W. C. Haxton, Phys. Rev. C **89**, 065501 (2014).

[30] M. I. Gresham and K. M. Zurek, Phys. Rev. D **89**, 123521 (2014).

[31] V. Gluscevic, M. I. Gresham, S. D. McDermott, A. H. G. Peter, and K. M. Zurek, J. Cosmol. Astropart. Phys. 12 (2015) 057.

[32] V. Gluscevic and S. D. McDermott, 2015, dmdd, Astrophysics Source Code Library, record ascl:1506.002.

[33] McLure *et al.*, J. Chem. Soc., Faraday Trans. 1 **78**, 7 (1982).

[34] D. R. Tovey *et al.*, Phys. Lett. B **488**, 17 (2000).

[35] G. Cowen *et al.*, Eur. Phys. J. C **71**, 1554 (2011).

[36] O. Buchmueller, M. J. Dolan, S. A. Malik *et al.*, J. High Energy Phys. 01 (2015) 037.

[37] D. Abercrombie *et al.* arXiv:1507.00966 [hep-ex] (2015).

[38] A. Boveia *et al.* Report Number CERN-LPCC-2016-001. arXiv:1603.04156 [hep-ex] (2016).

[39] CMS Collaboration, Report Number CMS-PAS-EXO-16-037 (2016).

[40] CMS Collaboration, Report Number CMS-PAS-EXO-16-039 (2016).

[41] C. Fu *et al.*, Phys. Rev. Lett. **118**, 071301 (2017).

[42] M. G. Aartsen *et al.*, Eur. Phys. J. C **77**: 146 (2017).

[43] T. Tanaka *et al.*, Astroph. J. **742**, 78 (2011).

[44] K. Choi *et al.*, Phys. Rev. Lett. **114**, 141301 (2015).

[45] L. Roszkowski, R. R. de Austri, and R. Trotta, J. High Energy Phys. 07 (2007) 075.

[46] D. S. Akerib *et al.*, Phys. Rev. Lett. **116**, 161302 (2016).

[47] E. Aprile *et al.*, Phys. Rev. D **94**, 122001 (2016).

[48] E. Aprile *et al.*, Phys. Rev. Lett. **119**, 181301 (2017).

[49] S. Adrián-Martínez *et al.*, Phys. Lett. B **759**, 69 (2016).

[50] S. Adrián-Martínez *et al.*, J. Cosmol. Astropart. Phys. 05 (2016) 016.

[51] D. S. Akerib *et al.*, Phys. Rev. Lett. **118**, 021303 (2017).

[52] A. Tan *et al.*, Phys. Rev. Lett. **117**, 121303 (2016).

[53] G. Angloher *et al.*, Eur. Phys. J. C **76**: 25 (2016).

[54] R. Agnese *et al.*, Phys. Rev. Lett. **116**, 071301 (2016).

[55] P. Agnes *et al.*, Phys. Rev. D **93**, 081101 (2016).

[56] R. Agnese *et al.*, Phys. Rev. Lett. **112**, 241302 (2014).

[57] R. Agnese *et al.*, Phys. Rev. D **92**, 072003 (2015).

[58] L. Hehn *et al.*, Eur. Phys. J. C **76**: 548 (2016).

[59] M. Aaboud *et al.*, Phys. Rev. D **94**, 032005 (2016).